Structural and Functional Investigations on Pyrin/TRIM20, a Modulator of the Innate Immune Response

Dissertation

zur

Erlangung der naturwissenschaftlichen Doktorwürde
(Dr. sc. nat.)

vorgelegt der

Mathematisch-naturwissenschaftlichen Fakultät

der

Universität Zürich

von

Christopher Weinert

aus Deutschland

Promotionskomitee

Prof. Dr. Markus Grütter (Leitung und Vorsitz)
Prof. Dr. Ben Schuler
Prof. Dr. Sabine Werner

Zürich 2013

Acknowledgement

The presented work would not have been possible without the help of many people. I am very thankful for their help, contribution and support during the last years.

I am very thankful to Prof. M. G. Grütter for giving me the possibility to work on a very interesting and challenging project, for his support and ideas at all stages, and for providing an excellent working environment.

I want to thank Prof. Sabine Werner and Prof. Ben Schuler for being in my thesis committee.

I am very grateful to Aleksandra Djekic and Dominik Possner for their direct contribution and input to this project and the chance to guide them through their master thesis. Without their commitment, this project would have not progressed as much as it did.

I wish to thank PD Peer Mittl for his help in X-ray crystallography and his many ideas for my thesis. I especially thank Damien Morger for the many discussions about TRIM proteins and the work we have done together. I thank Dr. Peter Gutte for the collaboration on another project. For their help and support I thank Dr. Stefan Schauer, who introduced me to SPR, and Dr. Manfred Rössle for his assistance in SAXS experiments.

I would like to thank the staff of the Institute of Biochemistry, namely our secretary Salome Rittmeyer, Adrian Schmid and Sascha Weidner of the workshop, and Steve Rast and Stefan Klauser of the IT service. I also want to thank Beat Blattmann and Céline Stutz-Ducommun of the NCCR crystallization facility.

Many thanks to all former and present members of the Grütter group as well as the Dutzler group for many interesting discussions, a great lab atmosphere and their support. I especially thank Andreas Flütsch, Heidi Roschitzki and Brian Brissoni for their input and contributions.

I would also like to thank all my friends for the great time outside the lab and their support.

Last but no least I want to thank my parents and my brother, who have always supported and encouraged me, and Cäcilia for her support, patience, encouragement and love during these years.

Content

Abstract

The innate immune system has evolved a complex and highly regulated system to sense foreign pathogens and injury through the recognition of associated molecules by special receptors, the so called pattern recognition receptors (PRR). One group of intracellular PRRs is the family of Nod-like receptors (NLRs) that can sense various pathogens as well as danger associated molecules and trigger the release of pro-inflammatory cytokines and/or the transcription thereof. Genetic variations in key proteins can alter signaling events and may lead to innate immune disorders. A prototype of such a disorder is the Familial Mediterranean Fever (FMF), where patients develop spontaneous attacks of inflammation without pathogenic infections. FMF is caused by genetic alterations of the gene encoding the protein pyrin/TRIM20.

Pyrin belongs to the tripartite motif-containing family of proteins that is characterized by a shared domain architecture comprising a RING finger, a B-Box and a predicted coiled coil domain. Pyrin has no functional RING domain, but possesses an N-terminal pyrin domain and, as most other TRIMs too, a C-terminal B30.2 domain. The function of pyrin seems to be two-fold. It can act in a pro-inflammatory manner similar to the NLRs, but it can also inhibit the NLR mediated release of pro-inflammatory cytokines. Structurally, only single domains of homologous proteins were solved, but none of pyrin. There is also a lack of information on how these domains are structurally arranged in the full length protein. In this thesis i) structural information on pyrin or fragments of it, ii) the effect of FMF associated mutations, and iii) biochemical analysis of interactions of pyrin with ligands was quested.

Structure determination by X-ray crystallography of the pyrin B30.2 domain and several FMF associated mutants thereof identified that the domain folds identical to other B30.2 domains and that mutations alter the binding epitope commonly found in these domains. Mutations in the central cavity of the epitope, including M694V that confers a severe FMF phenotype, lead to changes in the shape of the cavity. Mutations in loop regions alter their conformational flexibility and led to the identification of an important stabilizing hydrogen bond network between two loops. Our results provide detailed insights into the characteristics of both the shape and loop flexibility of the binding epitope that are altered in FMF mutants.

The B30.2 domain in isolation is a monomer. The crystal structure of the B30.2 domain connected through a linker to the predicted coiled coil domain shows for the first time how TRIM proteins dimerize. The coiled coil and the proposed linker region form a central helical scaffold (CHS) domain. The monomeric CHS is composed of a 155 Å long helix, a turn of two short helices followed by an elongated stretch and a forth helix antiparallel to the long helix. The CHS domain dimerizes in an antiparallel fashion along the first helix positioning the flexibly attached B30.2 domains close to the dimeric 2-fold axis and the N-termini of the two monomers 167 Å apart. Based on the structure, a stereotype full length TRIM was modeled illustrating the arrangement of the domains. In addition, a

crystal contact between two neighboring dimers suggests a new mechanism on how TRIM proteins may form tetrameric structures. The ability to form higher oligomers beyond dimerization has been shown for several TRIM proteins, but the contribution of each domain was not fully understood. Our structure provides a model for the initial step of the higher oligomer formation through the presented dimer dimer contact. The contact also involves FMF associated residues as well as loops of which the flexibility is altered by FMF mutations.

The dimeric construct also allowed us to investigate the suggested binding of pyrin to proInterleukin-1β (pro-IL-1β). Co-immunoprecipitation and Surface Plasmon Resonance experiments showed a clear interaction and revealed that pyrin is present in two states that bind to pro-IL-1β with different affinities. Size exclusion experiments reveal the formation of a high molecular weight complex. These results suggest that pyrin binds pro-IL-1β tightly when present as a higher oligomer most likely as a tetramer. As this interaction is linked to the inhibition of Il-1β maturation, the oligomerisation state of pyrin may play a regulatory role in the modulation of Il-1β.

Zusammenfassung

Pathogene und Verletzungen werden durch ihnen assoziierte Moleküle (sog. PAMPS und DAMPS) von speziellen Rezeptoren des angeborenen Immunsystems erkannt. Eine Familie dieser Rezeptoren bilden die NOD-ähnlichen Rezeptoren (NLR). Die Erkennung von PAMPS und DAMPS aktiviert die Expression entzündungsaktivierender Proteine und die Maturation von Zykokinen. Eine genetische Veränderung involvierter Proteine kann zu Veränderungen in der Signalweitergabe führen, welches in einigen Fällen Autoentzündungskrankheiten auslöst. Ein Beispiel dieser Krankheiten ist das gemeine Mittelmeerfieber (FMF), welches durch genetisch bedingte Veränderungen des Proteins Pyrin/TRIM20 hervorgerufen wird und sich durch spontane Fieberattacken kennzeichnet.

Pyrin gehört zur Gruppe der ‚tripartite motif containing' (TRIM) Proteine. TRIMs besitzen eine konservierte Domänenarchitektur, die aus einer RING Domäne, einer B-Box Domäne und einem ‚coiled coil' (CC) Motiv bestehen. Pyrin besitzt keine funktionelle RING Domäne, jedoch eine N-terminal Pyrin Domäne (PYD), und wie die meisten TRIMs eine zusätzlich C-terminale B30.2 Domäne. Die Funktion von Pyrin ist einerseits die Inhibierung einer NLR ausgelösten Immunantwort, es kann jedoch auch eine solche Antwort selbst induzieren. Strukturell ist Pyrin gänzlich unerforscht, lediglich Strukturen einzelner Domänen homologer Proteine sind bekannt

Das Ziel dieser Arbeit war es i) Pyrin oder Fragmente von Pyrin strukturell aufzuklären, ii) den Effekt von FMF assoziierten Mutationen zu analysieren und iii) Bindungen von Pyrin zu Liganden *in-vitro* biochemisch zu untersuchen.

Die Strukturbestimmung der C-terminalen B30.2 Domäne und mehrerer ihrer FMF-assoziierten Mutanten zeigt einerseits die domänentypische Faltung. Andererseits zeigen die Mutanten Veränderungen im allgemein angenommenen Bindungsepitop. Mutationen in der zentralen Bindungstasche des Epitops verändern hauptsächlich dessen Form, wohingegen Mutation in flexiblen ‚Loops', deren konformative Flexibilität beeinträchtigen. Die gelösten Strukturen ergeben ein detailliertes Bild der B30.2 Domäne und der Eigenschaften ihres Bindungsepitops.

Die isolierte B30.2 Domäne ist monomer in Lösung. Die Struktur des C-terminalen Fragmentes von Pyrin bestehend aus dem CC Motiv, einem Linker und der B30.2 Domäne zeigt zum ersten Mal die antiparallele Dimerisierung der TRIM Proteine. Das CC Motiv und der Linker bilden dabei eine zentrale helikale Gerüstdomäne (CHS), an welcher die B30.2 Domäne flexibel nahe der zentralen 2-fach Achse angebracht ist. Die N-termini beider Peptidketten liegen jedoch 167 Å voneinander entfernt. Damit kann zum ersten Mal gezeigt werden, wie die genaue Domänenarchitektur in TRIM Proteinen aussieht. Des Weiteren kann aus der Kristallstruktur ein Tetramer postuliert werden, welches als Baustein einer multimeren Selbstassemblierung dienen kann. Eine solche Selbstassemblierung wurde für mehrere TRIM Protein gezeigt.

Das dimere Konstrukt erlaubte uns ebenfalls, die postulierte Bindung von Pyrin zum Zytokine proInterleukin-1β (pro-IL-1β) zu messen. Co-Immunoprezipitations- und

Oberflächenplasmonenresonanzexperimente beweisen die Interaktion beider Proteine *in-vitro*, wobei Pyrin in zwei verschiedenen Zuständen vorkommt, welche pro-IL-1β mit unterschiedlicher Affinität binden. Ein Komplex beider Proteine konnte mittels Gel-Permeations-Chromatographie detektiert werden, und zeigt ein hohes scheinbares Molekulargewicht des Komplexes. Die Resultate suggerieren, dass Pyrin pro-IL-1β mit höherer Affinität bindet, sofern es als höheres Oligomer (Tetramer) vorliegt. Da die Bindung von Pyrin zu pro-IL-1β dessen Maturation inhibieren soll, könnte der oligomere Zustand von Pyrin eine regulatorische Funktion besitzen.

1 Introduction

1.1 Innate Immune System

The innate immnue system is the first line of defense against foreign pathogens and tissue damage. The ability to sense pathogens as well as injury and the capability of clearance by phagocytosis, the innate immune system provides a fast and general defense mechanisms against harmful factors. The recognition of tissue damage and foreign invaders, such as bacteria, viruses, and fungi is performed by the soluble factors of the complement system and specialized white blood cells, namely monocytes, neutrophils, macrophages or dendritic cells. Upon recognition a local and systemic response is induced by releasing signaling molecules (e.g. chemokines and cytokines). The systemic response leads to the production and differentiation of white blood cells in the bone marrow, the secretion of acute phase response reactants by the liver, the onset of fever and the activation of the adaptive immune system. The local response includes an increased blood flow and vasodilatation at the site of action that allows the recruitment of a larger set of phagocytic cells, activation of phagocytosis, and the secretion of antimicrobial substances[1,2]. The sensing of pathogens and cell damage by white blood cells is mediated through a germ-line encoded set of proteins, which recognize special molecular patterns associated to pathogens and broken cells, called pathogen and danger associated molecular patterns (PAMPS, DAMPS). This set of proteins includes cell surface receptors and cytoplasmic receptors that comprise four families of proteins: the membrane bound toll-like receptors (TLR) and C-type lectin receptors (CLR) and the intracellular nucleotide-binding and oligomerization domain (NOD)-like receptors (NLR), and the retinoic acid-inducible gene I (RIG-I)-like receptors (RLR). They all have sensing domains for specific PAMPS or DAMPS. Upon binding of PAMPS or DAMPS, the receptors oligomerize and induce either a signaling cascade that leads to the transcription of several inflammatory proteins or/and induce the secretion of cytokines to the extracellular space.

1.2 Pattern Recognition Receptors

An overview of the known PRR is shown in figure 1.

1.2.1 TLRs

TLRs are the best characterized set of PRRs. They are type-1 membrane proteins and comprise an extracellular leucine-rich-repeat (LRR), a transmembrane domain and an intracellular toll/Interleukin-1 receptor homology (TIR) domain that triggers signal transduction. There are eleven human members known of this family. TLRs can sense a variety of PAMPS, such as viral RNA and DNA, bacterial cell wall

components like lipopolysaccharide (LPS) and bacterial flagellin. The extracellular LRRs have a varying number of repeats, ranging from 18 to 25, where each repeat is between 22-29 amino acids in length and has a distinct interval of leucines[3]. They form a horseshoe like structure and act as the PAMP sensing domain through their ability to directly bind to PAMPS in a versatile way[4-6]. The sensing of PAMPS leads to the activation of TLRs that induces a signaling cascade in the cytoplasm. This cascade is characterized by protein-protein interactions and protein modifications such as ubiquitination and phosphorylation that alter the functions of the participating proteins. As most proteins involved are present in an inactive state the modifications are needed for further signal transduction[7]. For several TLRs the following cascade has been described following TLR activation that is initiated at the intracellular TIR domain. Via the TIR domain the Myeloid differentiation primary response protein 88 (MyD88) is recruited. Myd88, sometimes in association with the TIR domain containing adaptor protein (TIRAP) then recruits the interleukin-1 receptor-associated kinase 1, 2 and 4 (IRAK1,2, and 4) and the tumor-necrosis-factor (TNF)-receptor associated factor6 (TRAF6). TRAF6 promotes the formation of K63-linked polyubiquitin chains linked to IRAK1 and TRAF6. These ubiqutin chains allow the binding and induction of two kinase complexes, namely the IκB-kinase complex (IKK) and the transforming growth factor β-activated kinase 1 (TAK1) in complex with the TAK1-binding protein 2 and 3 (TAB2, 3)[8]. Both these complexes activate the mitogen-activated protein kinase (MAPK) cascade that eventually leads to the activation of transcription factors, such as the nuclear factor κB (Nf-κB) and the activating protein 1 (AP-1)[9]. These transcription factors induce the expression a large set of inflammatory cytokine, chemokines and inflammatory associated proteins and in this way induce an innate immune response upon the recognition of PAMPS.

1.2.2 CLRs

The other group of membrane bound PRRs are the CLRs. They are mostly involved in sensing components of the fungal outer membrane, in particular carbohydrates like β-glucan and mannan[10]. The signaling occurs differently than seen for TLR. Through their cytoplasmic immunoreceptor tyrosine-based activation motif (ITAM) they recruit and activate the protein kinase C (PKC)δ which leads to the formation of a caspase-recruitment domain protein 9 (CARD9) dependent complex followed by the activation of Nf-κB and AP-1 transcription factors.

NLR and RLR are the intracellular receptors. RLRs are involved in the recognition of cytoplasmic viral RNA. The NLRs are activated upon a large set of PAMPS and DAMPS.

1.2.3 RLRs

RIG-I as a member of the RLR senses 5'-phophorylated and double stranded (ds) RNA of viral origin in the cytoplasm. RIG-I consist of the N-terminal tandem CARD motif, followed by a DExD-box RNA helicase domain and a C-terminal domain

(CDT) that binds to the RNA. Once the RNA is sensed, the CARD tandem motif is released from its autoinhibitory conformation and is able to recruit the tripartite-motif containg protein 25 (TRIM25). TRIM25 induces the formation of unanchored K63-linked polyubiquitin chains that allows the binding of RIG-I to the mitochondrial antiviral signaling protein (MAVS) that induces further downstream signaling and transcriptional activation[11,12].

1.2.4 NLRs

The NLRs have a central NOD domain and a C-terminal LRR. The N-terminal domain is variable and may contain a CARD, Pyrin domain (PYD), a Baculovirus inhibitor of apoptosis protein repeat (BIR) domain or other domain. Depending on their N-terminal domain they are called NLRP (NOD, LRR and PYD domain contain proteins) , NLRC (NOD, LRR and CARD domain containing proteins) or NAIP (BIR-containing protein). In humans NLRP1-12, NLRC1-5 and NAIP are found. Not all members of these groups are functioning as a PRR, as this functions has only clearly been assigned to NLRP1, 3, 6 and 12, NLRC1, 2 (also called NOD1 and 2) and NLCR 4 and NAIP. Whereas NOD 1 and 2 are involved in Nf-κB activation upon recognition of peptidoglycans via the recruitment of the receptor-interacting protein kinase 2 (RIP2), NLRP1,3,6,and 12, NLRC4 and NAIP are involved in the activation and release of the proinflammatory cytokines proInterleukin-1β (pro-IL-1β) and prointerleukin-18 (proIl-18) via platforms that are termed inflammasome[13].

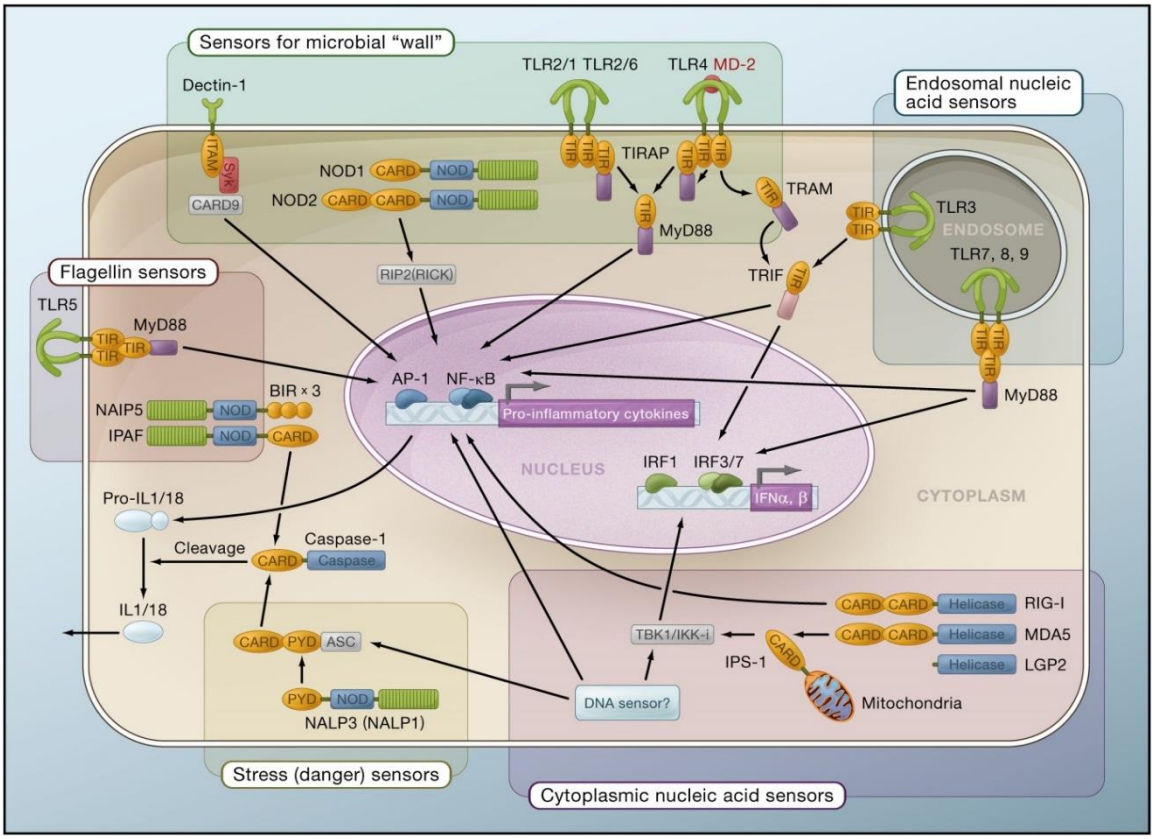

Figure 1: Overview of Pattern Recognition Receptors and their downstream signalling events. Taken from Ishii et al., 2008[14]. The proteins are named as indicated in the text.

1.3 The inflammasome

Inflammasomes are mulitprotein complexes that lead to the maturation of proInterleukin-1β (pro-IL-1β) and proInterleukin-18 (proIl-18). Both cytokines are expressed as inactive proforms and need to be proteolytically processed to the mature form. The enzyme responsible for the proteolytic activation is the Cystein-dependent aspartate-directed protease 1 (caspase-1). Caspase-1 is one of 12 caspases found in humans that are expressed as zymogens. Caspases are cysteine proteases that cleave C-terminal of an aspartic acid and are involved in cytokine processing but also in of apoptosis, also called programmed cell death. They are therefore grouped into inflammatory and apoptotic caspases. The inflammatory caspases include caspase-1, -4, -5 and -12. Caspases share the same domain architecture in their catalytic domain, having a small and large subunit. Inflammatory, as well as some apoptotic members have an additional recruitment domain that in case of Caspase-1 is a CARD domain. The CARD as well as the earlier mentioned PYD domain belongs to the group of death domains (DD) that are shown to interact in a homotypic manner with other DD-containing proteins[15]. The formation of the inflammasome greatly relies on such homotypic interactions.

A first step in inflammasome activation is the sensing of a stimulus. The direct stimuli is in most cases not known and has only been clearly proven in case of NLRP1, murine NAIP5 and NRLX1 (containing an N-terminal X-1 domain), which have been shown to directly interact with muramyl dipeptide, bacterial flagellin and RNA, respectively. The best characterized inflammasome, formed by NLRP3, is activated by a large variety of signals that change the cytoplasmic environment upon cellular stress and damage. Activation can occur by such different stimuli such as extracellular ATP, nigericin, changes in the osmotic pressure by pore forming toxins, or reactive oxygen species[13]. It is also associated with viral infections. In all cases the stimulation induces the oligomerization of the NLRs into large disc-like structures and the recruitment of other proteins to the inflammasome[16,17]. Recently, the crystal structure of the NLRC4 has been solved in its auto-inhibited state. The structure reveals that the LRR region binds to the NOD domain and through this intramolecular binding inhibits the oligomerisation of NLCR4, illustrating the need for stimulus binding to multimerize[18]. Through their N-terminal domain, NLRC4 for example can directly recruit procaspase1 via homotypic CARD-CARD interaction[19]. In case of NLRP3, this requires the adaptor protein Apoptosis-associated Speck-like protein containing a CARD (ASC), which possesses both a CARD and a PYD and therefore acts as a bridging or adaptor molecule to recruit procaspase-1[20]. The recruited zymogen procaspase-1 then autoactivates itself through an induced proximity mechanism that leads to the proteolytic cleavage of the polypeptide chain of procaspase-1 at three distinct sites. Procaspase-1 is cleaved C-terminal of the recruitment domain at residue 119 and

between the small and big subunits at residues 297 and 316[21]. The resulting p10 and p20 subunit form a heterotetrameric active caspase-1, and in this respect the inflammasome is regarded a caspase-1 activation platform. Caspase-1 modifies its substrates proteolytically as it is the case in the cleavage of proI-1β that occurs at two sites. The first cleavage occurs within the prodomain at aspartate 28. The second cleavage occurs at aspartate 116, yielding the active C-terminal fragment[22,23].

1.4 Interleukin-1β

The result of inflammasome formation is the maturation of Il-1β, which is a potent pro-inflammatory cytokine that upon its maturation is released into the extracellular space by non classical secretion pathways[24]. Il-1β acts in a paracrine and autocrine manner to amplify the inflammatory response of the innate immune system. It binds to Il-1 receptors (Il-1R) that in a similar manner as described for the TLRs lead to the activation of Nf-κB through a cascade initiated by the cytoplasmic TIR domain. Via this signaling cascade Il-1β induces the transcription of a large set of genes in various cell types that mediate a systemic pro-inflammatory response[25]. Due to the systemic and potent effect if this cytokine, Il-1β is regulated at various stages ranging from the gene transcription, mRNA lifetime, expression as precursor, maturation, secretion, and receptor binding[26]. It is therefore not surprising, that alterations in the regulation of Il-1β activity are associated to diseases. One example are alterations of the gene coding for NLRP3, which cause cryopyrin (an older name for NLRP3) associated periodic syndromes (CAPS), which belong to the group of auto-inflammatory diseases. Mutations in the gene are thought to either cause increased expression of NLRP3 or alter the auto-inhibited state of NLRP3[27]. Due to their association to increased pro-IL-1β maturation, treatment usually occurs with Il-1R antagonist or anti-Il-1β monoclonal antibodies. Another prototype of an auto-inflammatory disease is the Familial Mediterranean Fever.

1.5 Familial Mediterranean Fever

Familial Mediterranean Fever (FMF; OMIM #249100) is an autosomal recessive disorder and represents a prototype of hereditary recurrent fevers or autoinflammatory diseases that are characterized by recurrent episodes of fever without any signs of pathogenic infection[25,26]. In contrast to auto-immune diseases there is no increased titer of auto-reactive T-cells[28]. FMF is mostly found within ethnics of the eastern Mediterranean basin, such as Arabs, Armenians, Turks, and non-Ashkenazi Jews. Within these populations the carrier frequency for heterozygotes varies. In Turks and non-Ashkenazi Jews frequency was reported to be 1:13 and 1:11,4, respectively[29]. The highest carrier frequency is observed in Armenians being as high as 1:3. The disease onset is usually found within the first 20 years of live[30].

In FMF patients, the recurrent episodes of fever are accompanied by peritonitis, acute synovitis of joints and pleuritis mediated by an increased migration of neutrophils into these tissues. The self-limiting inflammatory attacks usually last for a few days up to one week with intervals of weeks up to month, where patients are symptom free[31]. An inflammation mediated chronic secretion of the acute phase reactant serum amyloid A (SAA), can lead to amyloidosis, which represents the most severe pathological consequence. The deposition of amyloid A fibrils in the kidney can lead to a nephrotic syndrome and renal failure[32]. The sudden onset of inflammatory attacks is triggered by environmental factors such as exposure to cold, psychological stress, tiredness and menstruation[33].
FMF is diagnosed by the evaluation of apparent symptons according to the Tel-Hashomer criteria[34]. The disease is treated with colchicine at a dosis of 1-2 mg daily or in case of colchicine resistance with anakinra, an Il-1R antagonist[35,36]. Colchicine is an inhibitor of microtubule association, able to reduce neutrophil migration. It is effective in abolishing the symptons as well as preventing amyloidosis. In 1997, two consortia independently identified the gene responsible for FMF, the *Mediterranean Fever gene*[37,38]. This gene codes for protein that was called pyrin, to recall its association to fever. Pyrin belongs to the family of tripartite-motif containing proteins.

1.6 TRIM proteins

Tripartite motif-containing proteins comprise a large family of proteins that share a common domain architecture. This motif consists of a Really-Interesting-New-Gene (RING) finger domain, one or two B-Box domains and a predicted coiled coil domain. The motif is also referred to as RBCC[39,40]. Members of this family are found in all metazoan[41,42]. The size of the protein family varies greatly across different species. According to Ozato et al, there are 65 human members, 64 in mice, 20 in worms and less than 10 in flies[42]. The fact that the tri-partite motif can be flanked by different domains and the low sequence similarity found in some parts makes an exact determination of the family size difficult.

The TRIM family can be divided into twelve subfamilies that are grouped according to the domains found in addition to the RBCC motif (see Fig. 2)[43]. Subfamilies I to XI all possess a RING domain, whereas the twelfth group contains members where no RING domain is present. Despite some members having no RING domain, there are other members that have no apparent B-Box or predicted coiled coil. However, if single domains are missing, the remaining domains are conserved in order and spacing[42].

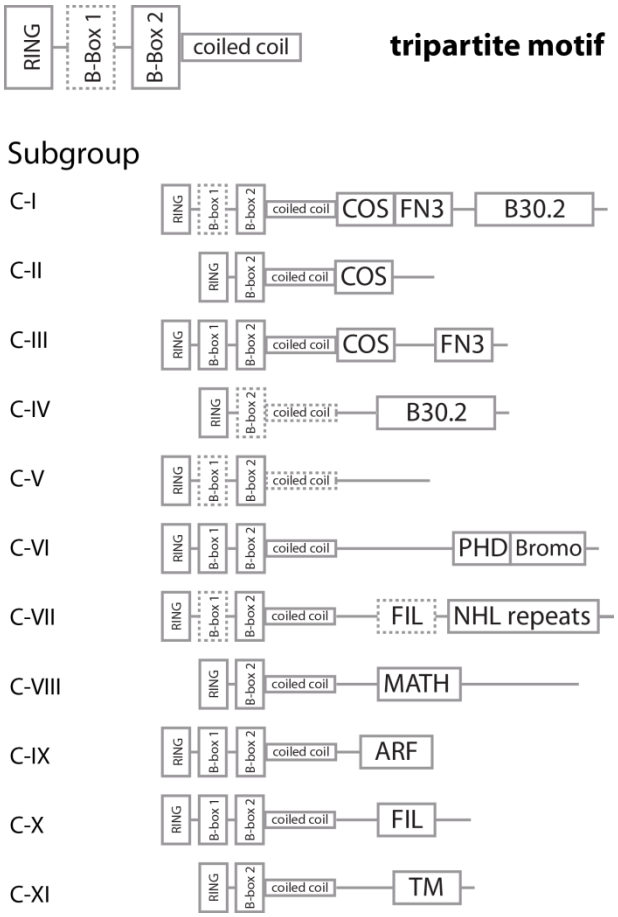

Figure 2. The tripartite motif and domain composition of the different TRIM subfamilies. The subgroup C-XII is not depicted. The abbreviations for the domains are as described in the text. Adapted from Short et al., 2006[44].

1.6.1 The TRIM motif

Although TRIM proteins are involved in various different cellular processes, distinct functions can be assigned for each of the domains found in the common tripartite motif.

1.6.2 RING finger

RING domains are between 40 and 60 residues in length and share a common motif of eight conserved residues able to coordinate divalent cations such as zinc[45,46]. First structures of RING domains revealed the mode of coordination of two zinc atoms[47,48]. The ββα fold of the RING domain coordinates the first zinc atom via the first and second conserved cysteine together with cysteine five and six in a tetrahedral manner (CCCC finger). The second zinc-finger is made by a cysteine and a histidine at position three and four and the last two cysteines (CHCC finger; see Figure 3A and 4). This cross brace manner of zinc coordination is a characteristic feature of RING domains, and was later also shown in related domains, such as the B-Box domain (see below). First insights into the function were revealed by several groups showing that the Ring Box protein 1 (Rbx1) is

involved in the ubiquitination of Sic1, an inhibitor of cell cycle progression. The ability to act as an E3 ligase was then found for several unrelated RING containing proteins, suggesting the E3-ligase activity as a common function of RING domain containing proteins[49]. Through genome wide screening more than 300 proteins containing a RING domain are now identified in the human genome[50]. The largest protein family found within these RING containing proteins is the TRIM family with approximately 78 members. Soon after the discovery of the E3-ligase activity of RING domains, first evidence was presented that also TRIM proteins are involved in ubiquinitation process of target proteins in a RING dependent manner. TRIM18/MID1 for example, was shown ubiquitinylate PP2A, the microtubule associated phosphatase 2A[51,52]. TRIM25 was shown to target 14-3-3σ, a negative cell cycle regulator that causes G2 arrest, to proteosomal degradation by ubiqitination[53]. Besides targeting proteins for degradation through so called K48-linked ubiquitination, several TRIM proteins were also shown to activated an innate immune response by creating unanchored K63-linked poly-ubiquitin (poly-ub) chains[54,55]. The type of ubiquitination is dependent on the E2-conjugating enzyme. TRIM proteins have been shown to able to recruit both types of E2-enzymes that either tag target proteins with K48-linked poly-ub chains or are capable of producing unanchored K63-linked poly-ub chains. The type of ubiquitination has clearly been demonstrated for a few TRIM proteins. TRIM5α and TRIM21 have been shown to induce K63 unanchored poly-ub formation, whereas TRIM27 links K48-linked poly-ub chains to target proteins[56-58].

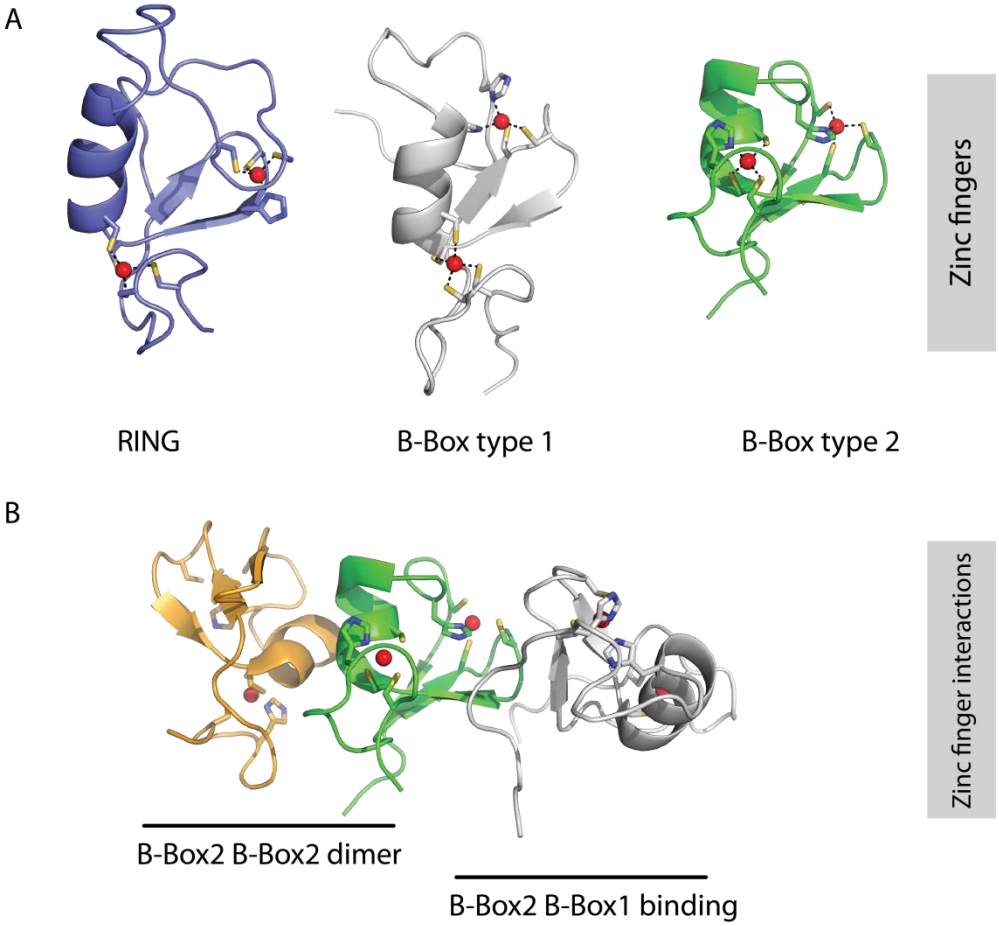

Figure 3: The tripartite motif: A) Structures of the Zinc-fingers are shown in a cartoon representation. The residues involved in the cross brace coordination of the Zn^{2+} (red spheres) are shown as sticks. B) Two interactions are proposed for the B-Box2. The formation of dimers was seen for TRIM63, and a B-Box1 B-Box2 interaction was seen in the solution structure of TRIM18. The central B-Box2 is in the same orientation and color as in A. The second B-Box2 found in the dimer is shown on the left and colored in orange. B-Box1 is colored as in A.

1.6.3 The B-Box

In TRIM proteins, two type of B-Boxes are found that differ in their zinc binding consensus motif and overall length, B-Box type 1 (B-Box1) and B-Box type 2 (B-Box2). With some few exceptions B-Box domains are exclusively found in TRIM proteins. The B-Box1 is only found in a few members of the family, the B-Box2 though is present in all TRIM proteins and is regarded the determinant of the TRIM family of proteins[59]. Solution structures of B-Box1 and B-Box2 revealed their similarity to the RING domain as they also fold into ββα structures[60,61]. In case of the B-Box2 this motif is followed by an additional third β-strand (see Fig. 3A). The coordination of the two zinc atoms occurs as seen in RING domains in a cross brace manner. The difference to the RING domain is that B-Box domains are shorter in length and have a changed consensus motif. The B-Box domains function as a protein a binding domain. In the crystal structure of TRIM63/MuRF1 and TRIM54/MuRF3, the B-Box2 is present as a dimer[59]. The dimerization interface is formed by the α-helix of one protomer that binds into the concave side

of the β-sheet of the second protomer (see Figure 3B). In some TRIM proteins, the B-Box2 was found to be responsible for the formation of higher oligomers, probably due to the described ability to form homodimers. A prominent example is TRIM5α, where mutations of residues that correspond to residues within the dimerization interface found in TRIM63, led to the loss of function through the inability to form multimeric self-assemblies[62]. TRIM5α is a retroviral restriction factor that is dependent on the formation large self-assemblies, in order to potently restrict retroviruses.

An interesting feature has been observed in the solution structure of the TRIM18/MID1 B-Box1 B-Box2 tandem motif[63]. The structure revealed that the two types of B-Box domains form a stable interaction. This interface is formed by residues of the structured loop between β1 and β2 of both B-Box domains, and is located on the opposite site of the B-Box2 homodimer interface (see Fig. 3B).

Besides the contribution of the B-Box domain to form homotypic interactions, they have also been found to mediate other protein protein interactions. In case of TRIM18/MID1 the B-Box1 binds to the α4-subunit of the PP2A, targeting the later for degradation, as described above[51].

Just very recently, another function has been assigned for B-Box domains. In case of TRIM16, which harbors a B-Box1 B-Box2 tandem motif, but no RING domain, an E3-ligase activity has been assigned. However, it could not be clarified which of the B-Boxes confers this activity[64].

1.6.4 The Coiled Coil

The coiled coil is an α-helical assembly of 2 or more parallel or antiparallel amphipathic helices. Their characteristic sequence motif is a heptad repeat pattern (*abcdefg*), where residues at position *a* and *d* are hydrophobic. As the α-helix has 3.6 residues per turn, residues at these positions face the same side of the helix and make hydrophobic interactions with the corresponding residues of the partner helix/helices. The hydrophobic side chains pack into a knob-into-hole manner, which means that the side chain of the amino acid at position *a* (knob) binds into a hole formed by residues *d*, *g*, *a+1*, and *d+1* of the opposing helix[65]. The hydrophobic interactions are complemented by ionic interactions between charged residues at position *e* and *g*[66] (see Figure 4). The remaining residues at position *b*,*c* and *f* are usually hydrophilic. The average distance for the hydrophobic residues in the CC sequence is 3.5, which is a little less then the 3.6 residues per turn observed in α-helices. This difference is the reason why the α-helices coil around each other forming a left handed superhelical assembly with 3.5 residues per turn with respect to the superhelical axis[67]. The type of hydrophobic residue found at position a and/or d can determine the degree of oligomerization[68]. Likewise observations have been made for the charged residues at position *e* and *g*[69]. The regular heptad repeat pattern can be disrupted by non-heptad

sequence motifs. These stutters (four residue insert) and stammers (three residue insert) decrease or increase the superhelical coil character of the CC, respectively.

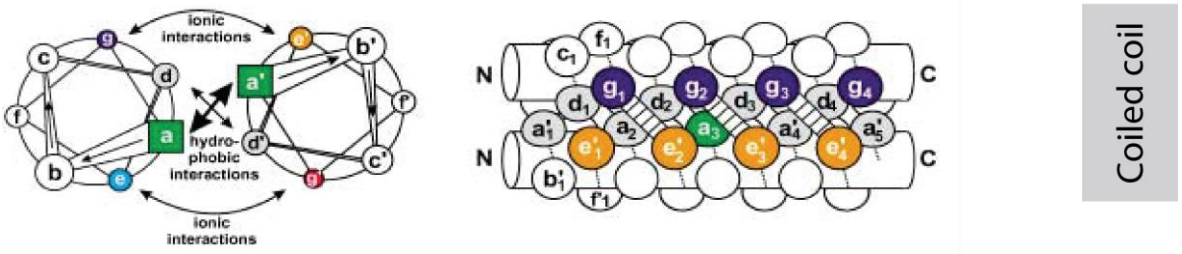

Figure 4: Indicated on the left are the residues of the heptad repeat pattern with their contributions to the coiled coil α-helical assembly. The knob into hole interaction as well as the ionic interactions are indicated on the right. Taken from Mason et al, 2004[69].

The B-Box2 is in almost all TRIMs followed by a predicted coiled coil motif (CC)[70]. The length and probability of the predicted CC region differ for the different TRIM proteins. With three exceptions, the CC lies within the first 120 amino acids C-terminal of the B-Box2 and is bipartite, meaning there are stretches of two sequence regions that can be interpreted to form a CC.

In a broad yeast-2-hybrid screening, most TRIMs studied were shown to form homo-oligomers in a coiled coil dependent fashion. In a few cases the formation of hetero-oligomers was found[71]. In case of TRIM5α and TRIM21, cross-linking experiments followed by SDS-PAGE analysis suggested the proteins to form trimers in a CC dependent manner[72,73]. However, it was later found that these putative trimeric species corresponded to dimers in solution when the oligomeric state was analyzed using purified proteins[57,74,75]. In case of TRIM5α, it was shown that the dimer formation does not only depend on the CC part, but also relies on residues C-terminal of the CC segment[76]. The ability of forming dimers has been shown to be essential for function as a deletion of either of the two CC regions leads to an inactive form of TRIM5α. Besides oligomerisation the CC region is also attributed to other functions. In both TRIM21 and TRIM27 cellular localization sequences were identified[77,78].

1.6.5 C-terminal domains

As depicted in figure 2, a variety of additional domains can be fused at the C-terminus of the tri-partite motif. These will be shortly discussed with a focus on the B30.2 domain which is found in more than half of TRIM proteins. In class C-I to C-III a C-terminal subgroup one signature (COS) domain is found right C-terminal of the predicted CC. This approximately 60 residue long domain is predicted to form a 2 α-helical coiled coil and is associated with microtubule binding[44]. The Fibronectin type III domain (FN3) present in subgroup C-I and C-III is approximately 100 amino acids long and folds into an immunoglobuline-like fold

comprising of 7 β-strands forming two antiparallel β-sheets[79]. In non-TRIM proteins the FN3 domain are found in cell surface receptors, cytokine receptors or receptor protein tyrosine kinases. Their role in TRIM proteins is unknown. In subgroup C-II the COS domain is found together with an acidic rich (AR) sequence, which is thought to be intrinsically disordered and has not been assigned to a specific function, yet.

In the subgroup C-VI a plant homeodomain (PHD) and a Bromo domain is found. The PHD finger belongs to the RING finger[80]. The Bromo domain forms a 4-helical bundle and recognizes acetylate lysines as found at the N-termini of histones[81]. The tandem motif of PHD domain and Bromo domain were shown to be important for TRIM28 to act as a transcriptional repressor[82].

The NHL (first identified in *ncl-1* , HT2A , and *lin-41*) domain is found in subgroup C-VII[83]. The structure of the NHL domain of the TRIM protein Brat from *Drosophila melanogaster* shows the domains six bladed β-propeller fold[84]. Brat acts as a translational repressor important in early development.

The Meprin And TRAF-Homology (MATH) domain found in subfamily C-VIII is involved in protein-protein interactions[85]. The ADP ribosylation factor-like domain (ARF) is involved in protein trafficking, the filamine like Ig (FIL) domain is important in the process of actin crosslinking and transmembrane domain (TM) anchors the protein to the cellular membrane[43].

1.6.6 The B30.2 domain

As mentioned the B30.2 domain is present of almost half of the TRIM proteins and is named after the exon it was first identified in[86]. In TRIM proteins it is either found in combination with COS-FN3 in subfamily C-I or as a single C-terminal domain in C-IV. Besides TRIM proteins, the B30.2 domain is also found in the Butyrophilin-related protein family, which comprises membrane bound receptor glycoproteins and in the Stonustoxin, a cytolytic protein of the stonefish *Synanceia horrida*[87] The B30.2 is closely related to a domain first identified in *Dictyostelium discoideum* dual-specificity kinase termed splA and in ryanodine receptors (RyR) domain that was named SPRY[88]. SPRY domains are found in a variety of proteins, e.g. the SPRY domain containing SOCX box (SSB) proteins that form multiprotein E3 ubiquitin complexes and are involved in suppression of cytokine signaling[89,90]. Primary sequence analysis revealed the relationship between the B30.2 domain and the SPRY domain. Where the B30.2 domain is between 180-200 amino acids in length[91], the SPRY domain is shorter in length. By identifying domain specific consensus motifs, it was shown that the SPRY domain motif is also found in the N-terminal part of the B30.2 domain. However the B30.2 domain has an additional C-terminal consensus motif not present in SPRY domains[92]. This extension is sometimes called PRY (for SPRY associated domain)[91]. Therefore the B30.2 domain can also be called PRYSPRY as it contains a SPRY domain with a C-terminal PRY extension. Structurally, the B30.2 folds into a six- and

seven-stranded β-sheet that form a β-sandwich. The sheets are connected by several loops in a jellyroll-like topology[91]. With respect to the subdomains PRY and SPRY, the PRY part consists of 3 β-strands and the SPRY domain of 10 β-strands. Both subunits are part of the globular structure of the B30.2 domain forming a single β-sandwich. Some of connecting loops between the strands are of variable length and show a high sequence variability between the different B30.2 domains (see Fig. 5). Structures of the SPRY domain show a very similar fold compared to the B30.2 domain. The SPRY part is also accompanied with a C-terminal extension that is an integrated component of the fold and structurally related to the PRY segment of the B30.2 domain[89,93].

The B30.2 and SPRY domains are thought to mediate protein-protein interactions. Several binding partners were identified for these domains. First structural insights into the mode of ligand binding were given by the dimeric PRYSPRY assembly of the similar to Ret-finger protein like 1 (sRFPL1), a protein of unknown function, the complex structure of TRIM21 binding to the Fc-region of an IgG, and the SPRY domain of GUSTAVUS binding to its interacting peptide[89,94,95]. The complex crystal structures revealed that in all cases a similar epitope is used to bind the ligand, which is created by the variable loops and the surface of the β-sheet (see Fig. 5). Besides the suggested common binding epitope, the mode of interaction between B30.2/SPRY domains is variable. In case of GUSTAVUS, the only SSB protein found in *Drosophila melanogaster*, its SPRY domain binds a linear peptide. TRIM21 binds to the Fc-region of the IgG via a complex interface binding to both the constant region 2 and 3 of the antibody's heavy chain creating two non continuous binding areas on the B30.2 domain of TRIM21.

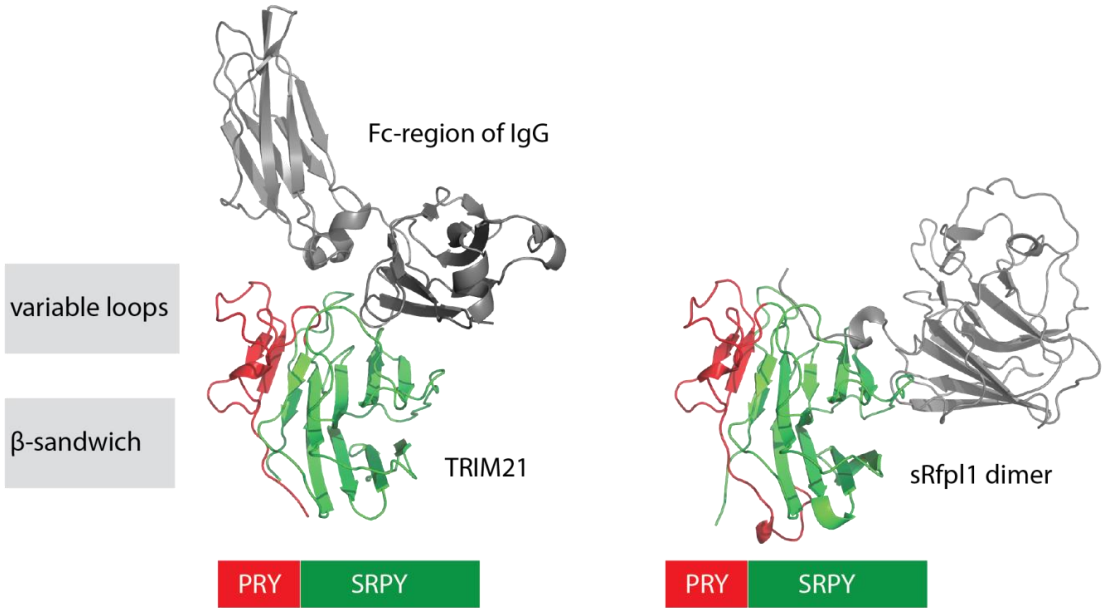

Figure 5: The B30.2 domains of TRIM21 and sRfpl1 with their bound ligands. The B30.2 domains are colored in red and green for their PRY and SPRY segment, respectively, and the bound ligand is colored in grey. The orientation of both B30.2 domains is identical.

1.6.7 TRIM function

TRIM proteins are involved in various processes and their different functions can mainly be attributed to the different C-terminal domains that lead to binding to different target proteins[96]. The tripartite motif then provides the platform for the effector function of the TRIM proteins. To illustrate the function of TRIM proteins, the binding to the target protein and the induced effect is illustrated for two well characterized TRIM proteins that belong to subfamily C-IV, namely TRIM5α and TRIM21. TRIM5α has been shown to potently restrict a variety of retroviruses and TRIM21 is an intracellular Fc-receptor.

In humans, TRIM5α potently restricts the N-murine leukemia virus, whereas the rhesus macaque orthologue restricts the human immune deficiency virus 1 (HIV-1). Upon entry of the retroviruses into the host cell, TRIM5α recognizes the assembled capsid lattice. The recognition of the capsid is mediated by the C-terminal B30.2 domain that directly interacts with the capsid proteins. Via interactions of the B-Box TRIM5α self-assembles into a multimeric lattice that engulfs the viral capsid cone[97]. Once self assembled, TRIM5α is able to induce the formation of K63-linked free ubiquitin chains through its RING domain. These K-63 linked ubiquitin chains induce the activation of the TAK-1 kinase complex which activates subsequently NF-κB and AP-1 induced transcription and expression of several inflammatory chemokines and cytokines[57]. In this manner TRIM5α acts as a PRR, as it senses directly the pathogen and induces downstream signaling.

TRIM21 acts as an intracellular Fc-receptor that also potently induces a pro-inflammatory response. Pathogenic particles such as viruses and bacteria that circulate in the body are exposed to antibodies and may eventually be coated with antibodies capable of binding. Once in the cytoplasm, the antibodies can be recognized by TRIM21 through the described binding to the Fc-region by the B30.2 domain. The binding of the TRIM21 to antibody coated pathogens induces again the formation of K63-linked free poly ubiquitin chains. This induces similar to TRIM5α the induction of the inflammatory cytokines. In addition TRIM21 autoubiquitinates itself, therefore targeting the pathogen-antibody-TRIM21 complex for proteosomal degradation, and therefore conferring clearance of the pathogen.

1.7 Pyrin

Pyrin is encoded by the Mediterranean fever gene (MEFV) located on the short arm of chromosome 16[37,38]. MEFV encodes the 781 amino acid long protein/TRIM20 that is a member of the TRIM protein family (see Figure 6 and 7). The N-terminal RING domain is degenerated as three out of eight conserved Zn^{2+} coordinating residues are mutated. It is therefore grouped to the subfamily C-XII which habors the RING-less members. However, with respect to the B-Box, CC and the C-terminal domain it belongs to the subfamily C-IV as it also harbors a B30.2 domain[70]. Additionally it has a long N-terminal insertion consisting of 303 amino acids. At the N-terminus it harbors a 95 amino acid PYRIN domain (PYD). In the adjacent linker region it also contains a B-zip domain, that is thought to be responsible for translocation to the nucleus[98,99]. Pyrin is mostly localized in the cytoplasm, although a splice variant of pyrin, which is missing the linker region between the PYD and the degenerated RING domain, was found to localize in the nucleus[100]. Pyrin is mostly expressed in monocytes, macrophages, neutrophils and eosinophils and its expression is under control of a variety of cytokines including type I and type II interferons, Tumornecrosis factor α (TNF), but also of PAMPS such as LPS[101,102]. Pyrin was shown to form a trimer through the CC domain by crosslinking studies, however the limitations of this method were shown for TRIM5α and TRIM21 (see above) suggesting that pyrin is also present as a dimer..

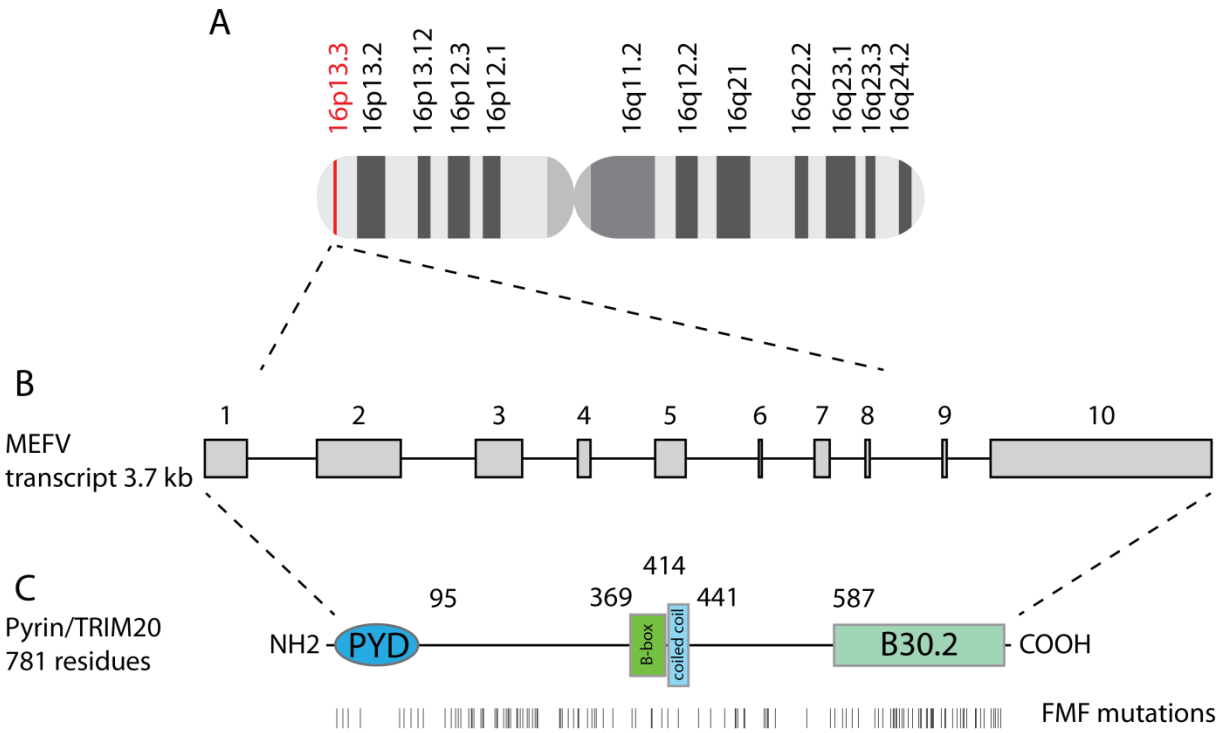

Figure 6: From gene to protein. A) The MEFV gene is located on the short arm of chromosome 16. B) The transcript consists of 10 exons, which are shown as grey boxes. Their length of the depicted box is in scale to their relative mRNA length. The introns are depicted as a black line and are not in scale. C) In the longest isoform, the MEFV gene encodes a 781 amino acid protein consisting of 4 domain (PYD: Pyrin domain). Adapted from Grandmange et al., 2008[103]. Mutations with a reported FMF phenotype are indicated as lines beneath the domain architecture of pyrin.

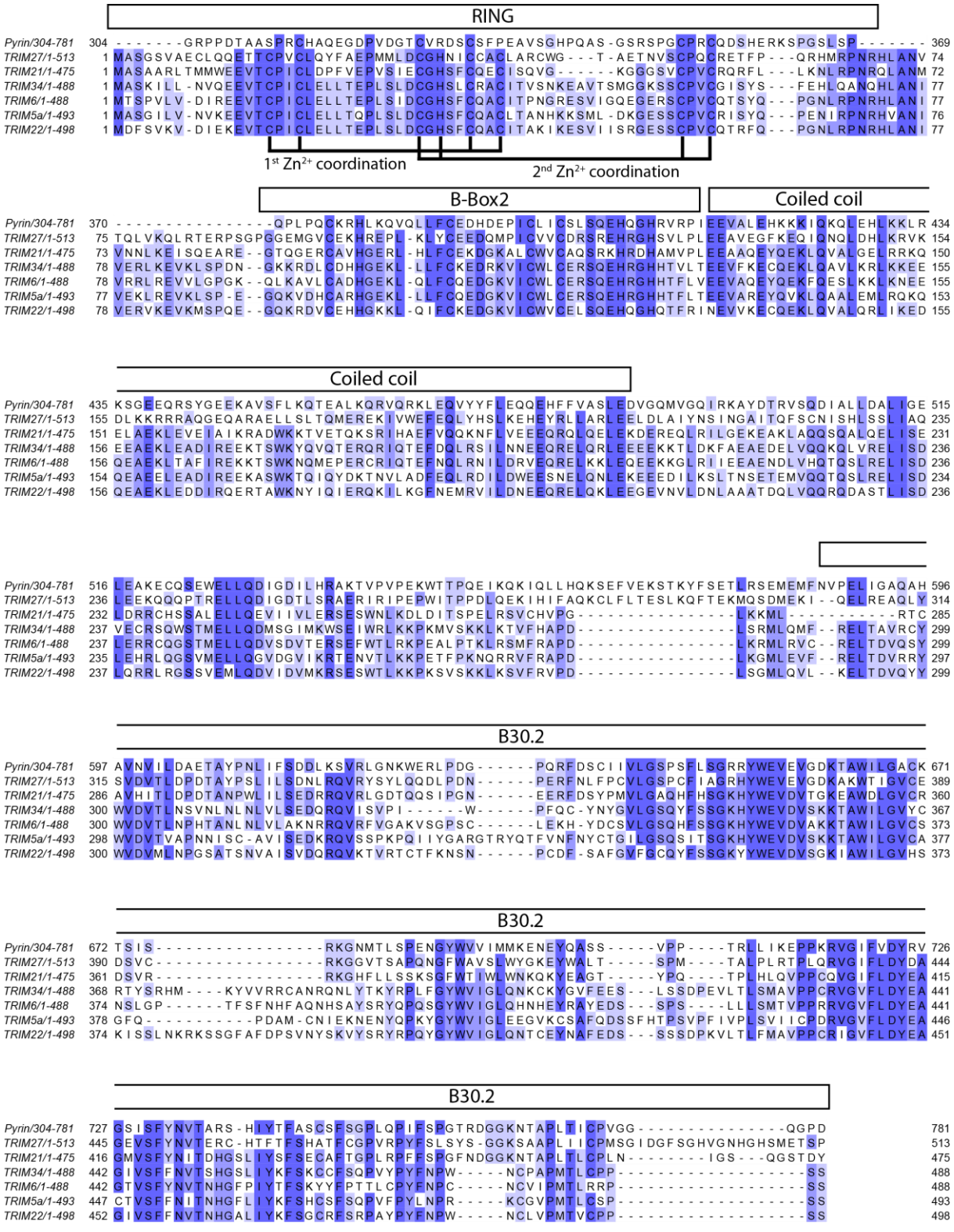

Figure 7: Sequence alignment of TRIM proteins of subclass C-IV: Conservation of residues is colored according to the BLOSUM62 score, where blue having the highest score. The domain boundaries are shown above the alignment in boxes. For the RING domain the cross-brace manner type of zinc coordination is indicated. Note that pyrin has lost 3 of the 8 conserved residues involved in zinc coordination.

PYRIN domain

The PYRIN domain (PYD) belongs to the superfamily of death domains (DD). This superfamily is characterized by its globular fold comprising of 6 anti-parallel α-helices that are arranged in greek key topology. Through their ability of forming homotypic interactions, they are widely found in inflammatory, apoptotic and necrotic signaling pathways[15].

1.7.1 Function of pyrin

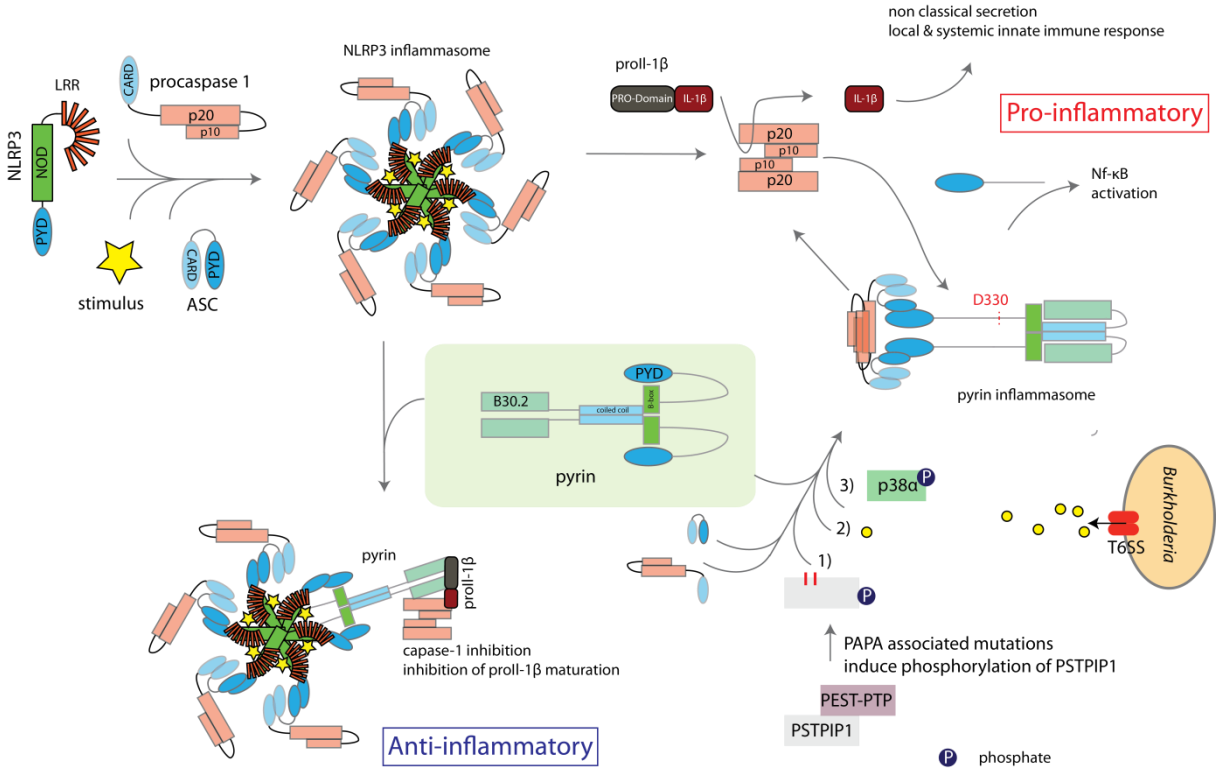

Figure 8: Function of pyrin. On the upper left: The NLRP3 inflammasome is formed upon stimulus recognition by its LRR, therefore releasing the NOD domain, which now oligomerizes to form a multimeric assembly with ASC to activate procaspase-1. In the middle: Dimeric pyrin is shown in its auto-inhibited state through the intramolecular interaction between PYD and B-Box. Lower right: Pyrin can inhibit the maturation of pro-IL-1β by binding to NLRP3 inflammasome components as described in the text. Activation of pyrin can occur via 1) PAPA associated mutations in PSTPIP1. Wild type PSTPIP1 is binding to the PEST-type phosphaste keeping PSTPIP1 dephosphorylated. PAPA associated mutations interfere with the binding to the phosphatase, and as a result PSTPIP1 is phosphorylated and activates pyrin by binding to the B-Box. 2) *Burkholderia cenocepacia* infection also results in the formation of a pyrin inflammasome through a type-6 secretion system dependent mechanism. 3) The third activation mechanism is described via activated kinase p38α.

A summary of the associated functions of pyrin is shown in figure 8.

Through its association to FMF, pyrin was suggested to function in the innate immune signaling and therefore most studies elaborated pyrin's contribution to this process. In yeast two-hybrid experiments, pyrin was shown to bind to the PYD domain of ASC through homotypic interactions[104]. The interaction seems to occur through the same interface as the NLRP3 PYD binds to ASC, as this interaction

can be competed with the pyrin PYD[105]. It was later found that pyrin can activate caspase-1 in a similar manner as described for NLRP3, by recruiting ASC and procaspase-1. The activation of caspase-1 by pyrin also resulted in the maturation of Il-1β and it was therefore postulated that pyrin can form an inflammasome as described for several NLRs[106]. Several mechanisms by which the pyrin inflammasome can be triggered were elucidated: 1) The Proline-Serine-Threonine Phosphatase Interacting Protein 1 (PSTPIP1) was shown to bind to pyrin in a phosphorylation dependent manner. PSTPIP1 is involved in cytoskeleton organization by forming filamentous networks[107]. Under normal conditions PSTPIP1 binds to rich in proline (P), glutamate (E), serine (S), threonine (T) protein threonine phosphatases (PEST-PTP) that keep PSTPIP1 dephosphorylated. The binding to the phosphatase is however altered in case of mutations in the PSTPIP1 gene that are associated to another auto-inflammatory disease called pyogenic arthritis, pyoderma gangrenosum and acne (PAPA) syndrome[108]. In case of PAPA associated mutations, the binding ability of PSTPIP1 to PEST-PTP is reduced leading to an increased phosphorylation of the PSTPIP1. The phosphorylated form has an increased affinity to bind to the B-Box of pyrin. It is thought that this binding event leads to the release of the PYD domain from the B-Box and as a result activates pyrin[109]. Although it is not clear, whether PSTPIP1 induces pyrin activation in case of wild type PSTPIP1, it clearly shows the pro-inflammatory potential of pyrin. 2) Just recently, it was shown that an infection with *Burkholderia cenocepacia* (*B.c.*), a gram negative bacterium that resides within vacuoles of macrophages, leads to procaspase-1 activation and Il-1β maturation in a pyrin dependent manner. The exact stimulus (PAMP) of the bacterium was not found, but pyrin activation was dependent on the type 6 secretion system of *B.c.,* suggesting that pyrin binds to a secreted bacterial protein. With confocal microscopy, it was shown that pyrin and ASC assembly around the vacuoles enclosing the *B.c.*[110]. 3) Another mechanism by which pyrin can be activated is through stress-induced activation of the mitogen-activated protein kinase (MAPK) p38[111,112]. By inducing ribotoxic stress that effectively activates (phosphorylates) the MAPK-p38, a pyrin dependent activation of procaspase-1 was observed. Interestingly, the MAPK-p38 is also activated by the signaling cascades induced by PRR, as described before.

In contrast to the pro-inflammatory function that could be assigned to pyrin, it was also shown that pyrin can negatively influence the maturation of the pro-inflammatory cytokine pro-IL-1β through inhibiting the NLRP3 inflammasome. Pyrin is recruited to NLRP3 through an interaction of its B30.2 domain and the NOD domain of NLRP3. In addition pyrin, was co-immunoprecipitated with active caspase-1, and the immature pro-IL-1β. Both interactions are also mediated by the B30.2 domain. Through the recruitment of pyrin to the inflammasome, and the binding capability to caspase-1 and pro-IL-1β, pyrin was shown to inhibit the maturation of the latter. However, the precise mechanism by which this inhibition

is mediated could not be assigned, but it was suggested that pyrin can inhibit the proteolytic activity of caspase-1. Additionally, due to the ability of pyrin's PYD domain to compete with NLRP3 binding to the PYD domain of ASC, it was also assumed that the recruitment of pyrin to NLRP3 inhibits the recruitment of ASC to the inflammasome.

Although pyrins interaction with caspase-1 was suggested to inhibit the protease, pyrin itself is a substrate of caspase-1. Pyrin is cleaved at aspartate 330. As a consequence of cleavage, the N-terminal product is capable of inducing NF-κB activation through inducing a proteosomal degradation of IκB, an inhibitor of NF-κB. The N-terminal product was also shown to bind to the p65 subunit of NF-κB inducing its relocalization from the cytoplasm into the nucleus and induce gene transcription[113].

With respect to the FMF associated mutations, different results were obtained. It was suggested that the interaction to NLRP3-inflammasome components might be weakened, which would lead to increased pro-IL-1β maturation. The obtained results were contradictory. In one case, a FMF mutation did lead to a decreased binding to caspase-1 and therefore the amount of Il-1β was increased[114]. In another study, the mutation did not have a visible effect on either of the two events[95]. Despite the contradictory findings with respect to the binding of pyrin to caspase-1 and pro-IL-1β, there seems to be an effect in case of the proteolytic cleavage of pyrin by caspase-1. Analysis of the state of pyrin from peripheral blood mononuclear cells revealed an increased amount of cleaved pyrin in FMF patients, suggesting that the N-terminal potential of NF-κB activation contributes to the disease symptoms[113].

1.7.2 FMF and pyrin

More than 120 mutations have been identified in FMF patients (see Fig. 6; Infevers[115]). However the frequency is very heterogeneous. Mutations with highest frequency in FMF are M694V or M694I (together 52 %), M680I (13 %), V726A (13 %), E148Q (11 %), A744S (1.7 %), R761H (1.2 %)[116-123]. All other mutations are less abundant, although not in all studies has the whole *MEFV* gene been sequenced, leading to the possibility of having missed certain mutations. Note that besides E148Q, all mutations affect the B30.2 domain of pyrin. A genotype-phenotype correlation can not be clearly assigned, as the phenotype not only depends on the mutation but is also influenced by other genes[31]. Some of the mutations also confer an atypical FMF phenotype.

However, a homozygous M694V genotype was clearly associated to the development of amyloidosis, higher risk of arthritis and to an earlier onset of disease[124,125]. For the other mutations, a tendency for the associated severity of the phenotype can be postulated[126].

1.7.3 Structure of pyrin

At the beginning of this thesis, there was no structural information on pyrin. Several structures of homologous domains were solved, namely the PYD domain, B-Box and the C-terminal B30.2 domain. With respect to the TRIM motif, the only domain/motif, of which no structural information of any homologue is available, is the predicted coiled coil. However, as this central domain mediates oligomerization and is essential for function, this motif is of special interest as it is not known how TRIMs oligomerize and how the adjacent domains are connected to each other.

1.8 Aim of the work

The association of pyrin to the disorder FMF reveals its importance in the modulation of an innate immune response. The many studies performed *in-vivo* elucidated the ability of pyrin to modulate the maturation of the proinflammatory cytokine pro-IL-1β. However, the mechanism by which pyrin can either act in a pro-inflammatory inflammasome like manner, or inhibit the activity of NLR-inflammasomes is not known. This is partly due to the complexity of the innate immune system, but also due to the lack of structural information and understanding of the interactions in which pyrin is involved in on a molecular level. At the start of thesis, all interaction studies regarding pyrin were done *in vivo.* Besides the many advantages of *in-vivo* studies, it was shown to be very challenging to study the effect of FMF related mutations on the binding behavior of pyrin. Additionally, the lack of structural information makes it difficult to predict domain boundaries that can be used to rationally design deletion mutants for *in-vivo* studies. This is not only true for pyrin, but also for the whole class of TRIM proteins, where only single domains of a few members have been solved.

The first aim of this thesis was therefore to structurally characterize pyrin or fragments of pyrin to obtain a structural understanding of pyrin and TRIM proteins on a molecular level. As most FMF related mutations are clustered in the B30.2 domain, and the fact that for this domain several binding partners were identified, we had a clear focus on this domain. By rational design of N-terminal deletion mutations, we aimed to identify stable pyrin fragments suitable for X-ray crystallography and *in-vitro* binding studies. In this thesis, we could solve two crystal structures of C-terminal fragments of pyrin. As described in the first publication we solved the structure of the B30.2 domain. We subsequently aimed to analyze the structural features of several FMF related mutants found in this domain which is summarized in the 2nd manuscript. However binding studies using the single B30.2 domain were not successful.

As all TRIM proteins oligomerize, we designed larger constructs that included the predicted coiled coil motif. As the minimal dimeric construct of pyrin (pyrinΔ413) was best expressed, we used this CC-B30.2 construct to establish binding assays and gather further structural information. The final aim was to characterize the effect of FMF related mutations on the effect of ligand binding.

The structure determination of the dimeric pyrin construct showed for the first time, how TRIM proteins mediate dimerization and how all domains are arranged in the full length protein. We also established quantitative and qualitative binding assays to test the interaction of pyrin to pro-IL-1β. These results are summarized in the 3rd manuscript.

2 Publication: Crystal Structure of the Pyrin B30.2 Domain: Implications for Mutations Associated with Familial Mediterranean Fever

doi:10.1016/j.jmb.2009.08.059 J. Mol. Biol. (2009) 394, 226–236

JMB

Available online at www.sciencedirect.com

ScienceDirect

ELSEVIER

The Crystal Structure of Human Pyrin B30.2 Domain: Implications for Mutations Associated with Familial Mediterranean Fever

Christopher Weinert, Christian Grütter, Heidi Roschitzki-Voser, Peer R. E. Mittl and Markus G. Grütter*

Department for Biochemistry, University of Zürich, Winterthurer Str. 190, CH-8057 Zürich, Switzerland

Received 19 June 2009; received in revised form 18 August 2009; accepted 19 August 2009
Available online 31 August 2009

The inherited autoinflammatory syndrome familial Mediterranean fever (FMF) is characterized by recurrent episodes of fever, which are independent of any bacterial or viral infections. This disease is associated with point mutations in the mefv gene product pyrin. Although the precise molecular functions of pyrin are unknown, it seems to be involved in the maturation and secretion of interleukin-1β. Approximately two thirds of all FMF-associated mutations cluster in the C-terminal B30.2 domain of pyrin. To investigate the molecular consequences of FMF-associated mutations, we determined the crystal structure of the pyrin B30.2 domain at 1.35-Å resolution. The comparison with other B30.2/ligand complex structures revealed a shallow cavity, which seems to be involved in binding the pyrin ligand. The bottom of this cavity is covered mainly with hydrophobic amino acids, suggesting that pyrin recognizes its ligand by hydrophobic contacts and surface complementarities. FMF-associated mutations cluster around two sites on the B30.2 surface. Approximately two thirds, including those mutations with the most severe disease outcomes, are observed in the vicinity of the predicted peptide binding site, suggesting that they will have a direct impact on ligand binding. A second mutational hot spot was observed on the opposite side of the B30.2 domain in the neighbourhood of its artificial N-terminus. Although most FMF-associated mutations are solvent exposed, several will modify the main-chain conformation of loops. The experimental crystal structure of the pyrin B30.2 domain serves as a basis for an accurate modelling of these mutations.

Keywords: innate immunity; inflammasome; inherited disease; crystal structure; NLRP

Edited by R. Huber

Introduction

The release of active interleukin-1β (IL-1β) from macrophages, monocytes, and dendritic cells is an early event in inflammation because it enables the entry of leukocytes to the site of infection or tissue injury, promotes maturation of lymphocytes, enhances the activity of natural killer cells, and triggers the onset of fever.[1] The proinflammatory cytokine IL-1β is expressed as an inactive 31-kDa precursor, and proteolytic cleavage of this precursor by caspase-1 liberates active IL-1β (reviewed in Ref. 2). Since IL-1β is crucial for the inflammatory process, the caspase-1 activity is tightly regulated. Caspase-1 is expressed as a precursor containing a CARD and a protease domain. The recruitment of inactive procaspase-1 into a macromolecular complex, called the inflammasome, through its CARD domain[3] causes activation of procaspase-1 by proteolytic cleavage on the C-terminal side of Asp297.[4]

Besides the proteolytic processing of zymogens, caspases are regulated by a number of inhibitory proteins, such as FLIPs, which act as caspase decoys, X-linked inhibitor of apoptosis proteins, which inhibit caspases through their BIR domains (reviewed in Ref. 5), or pyrin, which interacts with caspase-1.[6–8] Pyrin

*Corresponding author. E-mail address: gruetter@bioc.uzh.ch.

Abbreviations used: IL-1β, interleukin-1β; FMF, familial Mediterranean fever; TRIM, tripartite motif; ASC, apoptosis-associated speck-like protein with a CARD; GST, glutathione *S*-transferase; LRR, leucine-rich repeat.

(also known as marenostrin or TRIM20) belongs to the large family of tripartite motif (TRIM) proteins. This protein family is characterized by an N-terminal RING domain, one or two B-box type zinc fingers followed by a coiled-coil motif, and one or more additional C-terminal domains (reviewed in Ref. 9). TRIM proteins participate in diverse cellular processes such as proliferation, differentiation, apoptosis, and viral replication (reviewed in Ref. 10). In pyrin, the N-terminal RING domain is exchanged by a Pyd domain and harbours a C-terminal B30.2 domain (reviewed in Ref. 11). The largest spliced isoform of pyrin consists of 781 amino acids, and depending on the isoform, it is expressed in the cytoplasm or the nucleus of neutrophiles, eosinophiles, and monocytes.[12,13] The N-terminal PYD domain of pyrin is responsible for the recognition of the apoptosis-associated speck-like protein with a CARD (ASC), which acts as an adaptor protein in the inflammasome.[3,14]

Mutations in pyrin are associated with familial Mediterranean fever (FMF), a recessively inherited disease that is characterized by episodes of inflammation and fever.[15,16] FMF is considered to be an autoinflammatory syndrome due to the lack of any obvious stimuli and the involvement of autoreactive T cells (reviewed in Ref. 17). Autoinflammatory syndromes are caused by a dysfunction of the innate immune system. Mutations that are associated with FMF cluster in the C-terminal B30.2 domain of pyrin. Therefore, it is assumed that pyrin plays a role in the innate immune system, probably by effecting caspase-1-dependent IL-1β maturation. The role of pyrin in innate immunity is discussed controversially. Immunoprecipitation and glutathione *S*-transferase (GST) pull-down experiments established an interaction between the caspase-1 protease domain and the B30.2 domain of pyrin *in vitro*.[7,8] It was suggested that this interaction inhibits caspase-1-dependent IL-1β secretion because macrophages from pyrin-mutated mice showed elevated secretion of IL-1β upon stimulation with lipopolysaccharide,[6] and the knockdown of pyrin by RNA interference techniques in Thp1 monocytes enhanced IL-1β secretion as well.[8] On the other hand, pyrin was shown to activate caspase-1 by ASC oligomerization in a HEK293 cell-based reconstitution system.[18] Besides caspase-1 and ASC, pyrin was also found to interact with the cytoskeleton-organizing protein PSTPIP1,[19] some isoforms of 14-3-3,[20] and the pro-apoptotic protein Siva.[21] PSTPIP1 unlocks the N-terminal Pyd domain of pyrin and enables the formation of the pyrin/ASC complex.[19] The 14-3-3 protein recognizes amino acids in the linker region between the Pyd and the B-box domains of pyrin,[20] whereas Siva targets the C-terminal B30.2 domain.[21]

To investigate the molecular effects of mutations that are observed in FMF, we determined the crystal structure of the pyrin B30.2 domain at 1.35-Å resolution and compared it to the previously determined crystal structures of B30.2 domains from human sRFPL1,[22] GUSTAVUS in complex with different peptides,[23,24] and TRIM21 in complex with an Ig Fc fragment.[25] This analysis revealed that most mutations that are associated with FMF cluster around a putative peptide binding site. Since this binding site is blocked neither by ligands nor by crystal contacts, the described crystal structure will be of great value for probing the pyrin B30.2 peptide binding activity by fragment-based screening.

Results

Overall crystal structure of the pyrin B30.2 domain

Residues 577 to 780 of human pyrin (Uniprot entry O15553) were expressed in *Escherichia coli*. The crystal structure of the pyrin B30.2 domain was refined at 1.35-Å resolution and reveals clear electron density for all residues except for amino acids 577–585, 625–634,

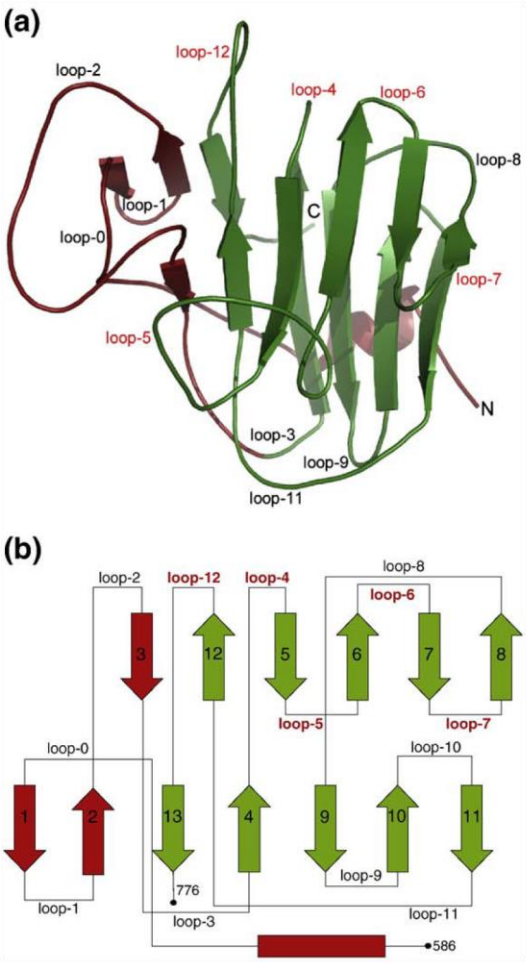

Fig. 1. (a) Ribbon diagram of the pyrin B30.2 domain showing the Pry and Spry subdomains in red and green, respectively. This standard orientation shows the Pry subdomain on the left and with the central cavity in front. Loops that are most likely involved in the recognition of the binding partner are indicated in red letters. (b) Topology diagram of the B30.2 fold.

and 777–780. The 191-amino-acid polypeptide chain folds into a compact β-barrel domain with overall dimensions of 47×35×31 Å^3 (Fig. 1a). The β-barrel consists of two antiparallel β-sheets that are connected in a jelly-roll topology. These six- and seven-stranded β-sheets possess pronounced left-handed twists and build up the hydrophobic core of the B30.2 domain. Besides some short helical loops, there is just one α-helix (residues 590–594). This helix packs against the seven-stranded β-sheet and runs perpendicular to the directions of the β-strands (Fig. 1a).

Based on sequence profile methods, B30.2 domains were subdivided into N-terminal Pry and C-terminal Spry subdomains.[26,27] Although pyrin B30.2 folds into a compact three-dimensional domain, this sequence-based subdivision is also structurally justified because the Spry subdomain of pyrin B30.2 (residues 650–776) possesses a similar structural architecture like carbohydrate-binding plant lectins from the agglutinin family, whereas the Pry subdomain is absent from the lectin fold. The Spry subdomain contains two five-stranded β-sheets in a sandwich-like arrangement, and each of these sheets is extended by additional β-strands from the Pry subdomain (Fig. 1b). The Pry subdomain serves as a N-terminal lid to shield the hydrophobic core of the larger Spry subdomain from the solvent. Both subdomains share an interface of approximately 1800 Å^2. The pyrin B30.2 structure reveals a pronounced *B*-factor distribution. The average *B*-factors for the Pry and Spry subdomains are 32.4 and 21.5 Å^2, respectively. The higher average *B*-factor of the Pry subdomain is caused by the increased flexibility of loop 2 (residues 625–634).

Residues involved in loops 0, 2, 4, 5, 6, 7, and 12 and β-strands 5, 6, 7, and 12 create a shallow cavity, with overall dimensions of approximately 15×11×6 Å^3, on the surface of the pyrin B30.2 domain. With the exceptions of Ser702 and Ser757, the bottom of this cavity is covered entirely by hydrophobic amino acids. The hydroxyl groups of Ser702 and Ser757 form hydrogen bonds with Leu682-O (2.38 Å) and Gly759-N (3.13 Å), respectively. During the refinement process, an ethylene glycol molecule from the cryoprotectant was observed. The hydroxyl group of this ethylene glycol molecule forms a hydrogen bond with Met693-O (3.13 Å). Besides two further ethylene glycol molecules (close to residues 589 and 597), we observed two thiocyanate ions during the refinement process. Thiocyanate ions were distinguished from ethylene glycol molecules by the anomalous signal of the sulfur atoms (data not shown). Potassium thiocyanate was crucial for the crystallization of pyrin B30.2. The thiocyanate ions bind in crystal contacts (close to residues 707 and 751), providing an explanation for the thiocyanate dependence of the crystallization process.

Comparison with other B30.2 domains

Homologues of the C-terminal B30.2 domain of pyrin have been observed in over 1000 proteins, and some of these domains have been structurally inves-

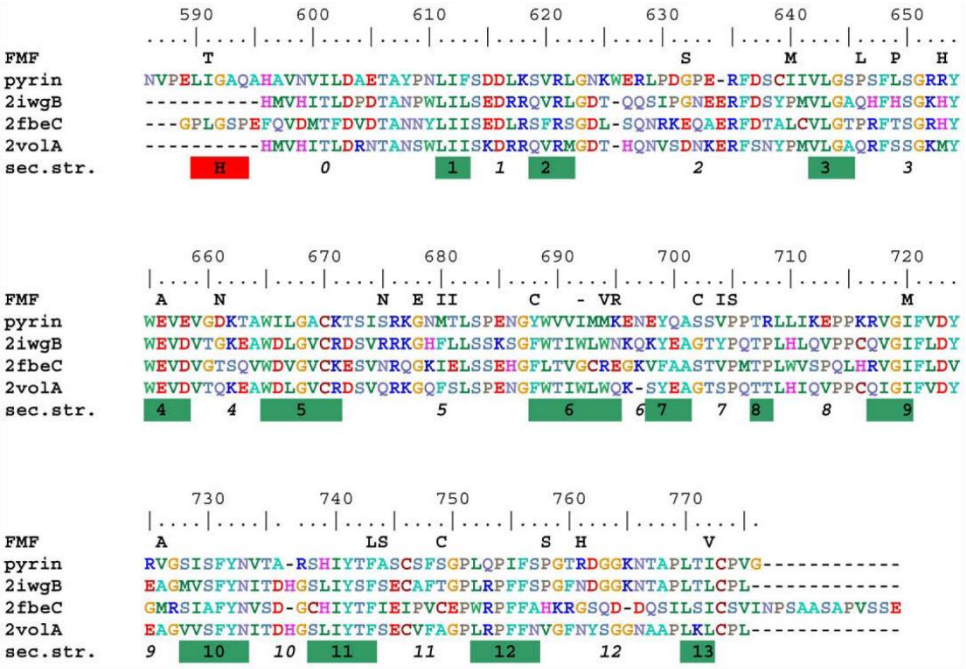

Fig. 2. Structure-based sequence alignment of B30.2 domains. Residues are numbered according to their positions in the full-length pyrin sequence (O15553). Mutations that are associated with FMF are given in the second row. Secondary structural elements including nomenclature of β-sheets (green squares) and loops (italic numbers) are indicated in the last row.

tigated. The structure of the pyrin B30.2 domain is similar to the structures of Trim21 in complex with an IgG-Fc fragment (2IWG; 1.02 Å for 178 C^{α} atoms),[25] sRFPL1 (2FBE; 1.44 Å for 179 C^{α} atoms),[22] and GUSTAVUS in complex with a 20-mer VASA-peptide (2IHS; 2.47 Å for 148 C^{α} atoms)[24] and is distantly related to galectin in complex with thio-digalactose (1A78; 3.28 Å for 120 C^{α} atoms).[28] A structure-based sequence alignment of B30.2 domains is given in Fig. 2. All of these proteins are involved in the recognition of peptides or carbohydrates, suggesting that pyrin B30.2 will also be involved in peptide or carbohydrate binding. The peptide binding modes of B30.2 domains were initially discovered in the dimerization interface of sRFPL1[22] and the GUSTAVUS/peptide complexes.[23,24] sRFPL1 recognizes the C-terminal tail of a symmetry-related molecule in a cavity, which is similar to the central cavity of pyrin described here, whereas the structures of GUSTAVUS/VASA and GUSTAVUS/elongin complexes revealed no central cavities and, thus, completely different peptide binding modes.[23,24] Since the pyrin B30.2 domain is more similar to sRFPL1 than to GUSTAVUS, we assume that its peptide binding site is similar to the dimerization interface of sRFPL1. Unfortunately, the biological function of sRFPL1 is currently unknown, but the significance of the sRFPL1 dimerization interface has been confirmed by its similarity with the Trim21/IgG-Fc complex.[25]

Figure 3a and b shows the superpositions of B30.2 domains from pyrin, sRFPL1,and TRIM21. In contrast to sRFPL1 and Trim21, the N-terminus of pyrin B30.2 adopts an α-helical conformation. In addition, loops 6 and 12, which contact the B30.2 binding partners in sRFPL1 and Trim21, as well as the flexible loops 2 and 5 possess different conformations in all three B30.2 structures. The molecular surfaces of the central cavities are also different. In sRFPL1, the central cavity recognizes the C-terminal tail of the symmetry-related sRFPL1 molecule. The α-helical conformation of the tail is stabilized by hydrogen bonds between main-chain atoms from the tail (Ser190′-O and Ser193′-O) and

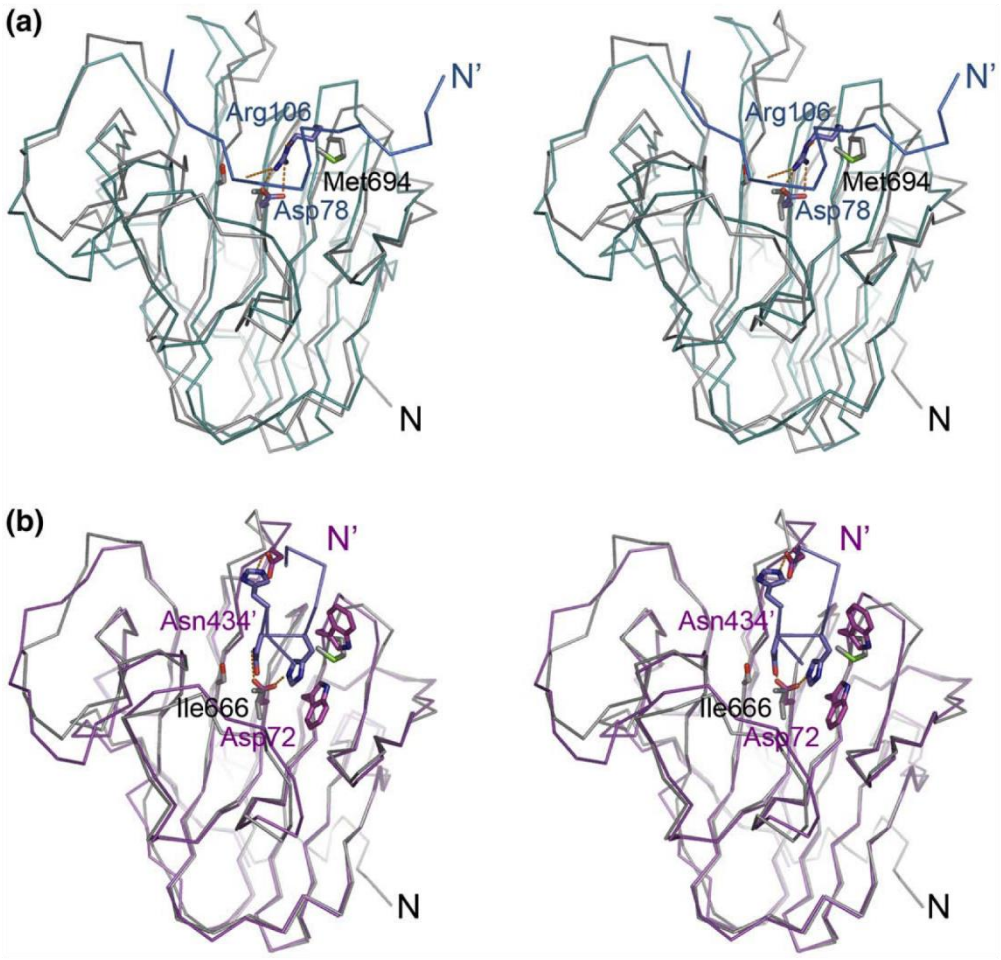

Fig. 3. (a) Superposition of pyrin B30.2 (grey ribbon) on sRFPL1 (blue ribbon) and (b) Trim21/Fc (magenta ribbon). Structures are given in the standard orientation as defined in Fig. 1a. The pyrin B30.2 N-terminus is labelled. Hyphenated labels refer to the peptide binding partners. Amino acids in black, blue, and magenta refer to pyrin, sRFPL1, and Trim21/Fc, respectively.

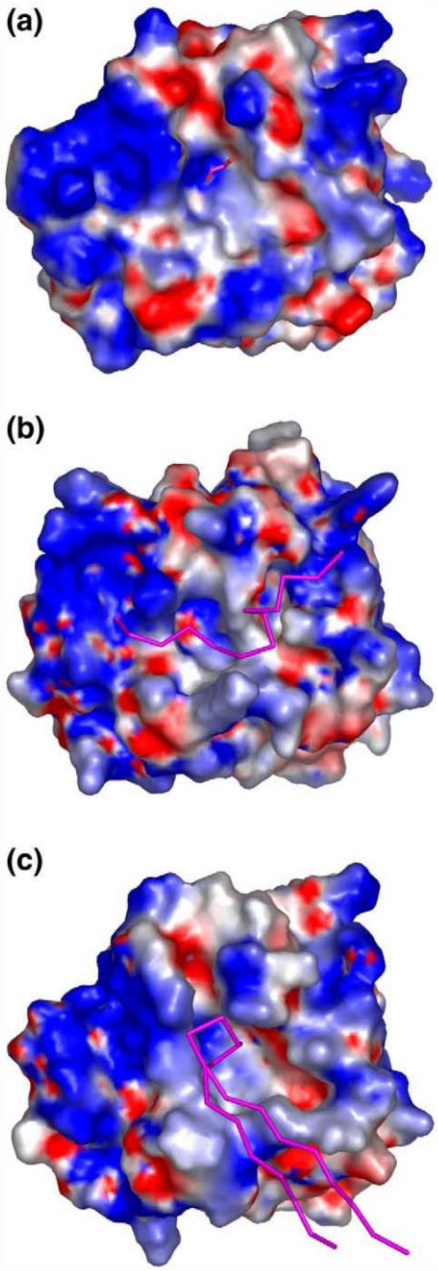

Fig. 4. Electrostatic surfaces of B30.2 domains from (a) pyrin, (b) sRFPL1, and (c) Trim21. The electrostatic potentials were contoured red and blue at −4 and +4, respectively. The bound ethylene glycol molecule in pyrin B30.2 and the bound peptides in sRFPL1 and Trim21 are indicated. Molecules are all shown in the standard orientation as defined in Fig. 1a.

the side chain of Arg106 from the central cavity (Fig. 3a). In sRFPL1, Arg106 points into the cavity due to a salt bridge between Arg106 and Asp78. In pyrin, B30.2 Arg78 and Asp106 have been replaced by Met694 and Ile666, respectively. The side chains of both hydrophobic amino acids are solvent exposed.

The central cavity of Trim21 recognizes a loop that is located at the hinge between the IgG domains of the Fc fragment. This hairpin loop contains a characteristic His_{433}-Asn-His_{435} sequence motif. In Trim21, the side chains of Asp72 (equivalent to Asp78 of sRFPL1) and Asp169 form hydrogen bonds with the side chains of His433, Asn434, and His435 from the IgG-Fc fragment (Fig. 3b). Although Asp169 of Trim21 is conserved in pyrin B30.2 (Asp762), it is unlikely that pyrin recognizes a β-hairpin conformation similar to Trim21 because the crucial Asp72 of Trim21 is replaced against Ile666 in pyrin. In summary, sRFPL1, Trim21, and pyrin contain central cavities for the binding of peptide ligands, but sRFPL1 and Trim21 recognize peptide ligands with completely different conformations. Because polar residues, which are crucial for the specific hydrogen-bonding patterns in Trim21 and sRFPL1, are replaced against hydrophobic amino acids in pyrin, the conformation of the pyrin B30.2 binding partner will be different from the conformations seen in the sRFPL1 and Trim21 complexes.

The central cavities possess similar distributions of positive- and negative-charge densities. Electrostatic surfaces of pyrin, sRFPL1, and Trim21 B30.2 domains reveal positively charged Pry and amphipathic Spry subdomains (Fig. 4). The conserved

Table 1. Mutations of pyrin B30.2 domain associated with FMF

Mutation	Phenotype	Location	Solvent accessibility	References
Ile591Thr	M	N	E	29, 30
Gly632Ser	U	A	E	31
Ile640Met	U	A	P	30, 32
Ile641Phe	U	A	B	32, 33
Pro646Leu	M	N	E	32, 33
Leu649Pro	M	N	E	32, 33
Arg653His	M	N	E	16, 29, 31
Glu656Ala	U	N	B	29, 32
Asp661Asn	M	A	E	32, 33
Ser675Asn	U	A	E	29, 34
Gly678Glu	M	A	E	29, 32
Met680Ile, Leu, Val	S	A	E	16, 29, 35
Thr681Ile	S	A	E	36
Thy688Cys	U	A	B	33
Ile692del	M	A	P	35
Met694Val, Ile, del	S	A	E	29, 35, 36
Lys695Arg	M	A	E	16, 29, 34, 35
Ser702Cys	U	A	P	32
Val704Ile	M	A	E	29, 33
Pro705Ser	U	A	E	29, 32
Ile720Met	U	C	B	29, 37
Val726Ala	M	N	E	15, 29, 35
Phe743Leu	M	C	B	16
Ala744Ser	M	N	E	29, 35
Ser749Cys	M	N	E	33
Pro758Ser	U	A	B	33
Arg761His	M	A	E	16, 29, 35
Ile772Val	M	C	B	33

M, mild form of FMF; S, severe form of FMF; U, unclassified disease outcome. A, at the central cavity; N, at the N-terminal site; C, in the hydrophobic core. E, solvent exposed; B, buried; P, partially solvent accessible.

distribution of positive- and negative-charge densities seems to be the effect of long-range interactions because charged residues within the central cavities differ significantly among the three B30.2 domains.

Mapping of FMF mutations

Most mutations that are associated with FMF cluster in the B30.2 domain of pyrin. Mutations of 28 positions that have been reported thus far are classified according to the severity of the FMF phenotype, the location in the B30.2 domain, and the solvent accessibility of the mutated residue (Table 1). Mutations that are associated with FMF are observed in three distinct areas of the pyrin B30.2 domain. Seventeen mutations cluster either directly inside or close to the central cavity, three mutations are located in the hydrophobic core, and eight mutations modify the molecular surface on the opposite side of the central cavity (Fig. 5a and b).

The high-resolution structure of pyrin B30.2 enables an accurate modelling of mutations that are associated with FMF. Many of these mutations are solvent exposed. These mutants will affect the binding to another interacting protein or protein domain. Mutations that will significantly alter the structure of pyrin B30.2 are discussed in the following sections (Fig. 6a and b).

Pro646Leu and Leu649Pro

Pro646 is located in loop 3 at the junction between Pry and Spry subdomains. The peptide bond of Pro646 is in a *cis* conformation. Since *cis*-peptide bonds of non-proline residues are extremely rare, the Pro646Leu mutation will affect the main-chain conformation of loop 3. Leu649 has main-chain dihedral angles of $\phi = -142°$ and $\varphi = 33°$. Since proline is unable to adhere to these dihedral angles, the Leu649Pro mutation will also affect the main-chain conformation of loop 3 (Fig. 6b).

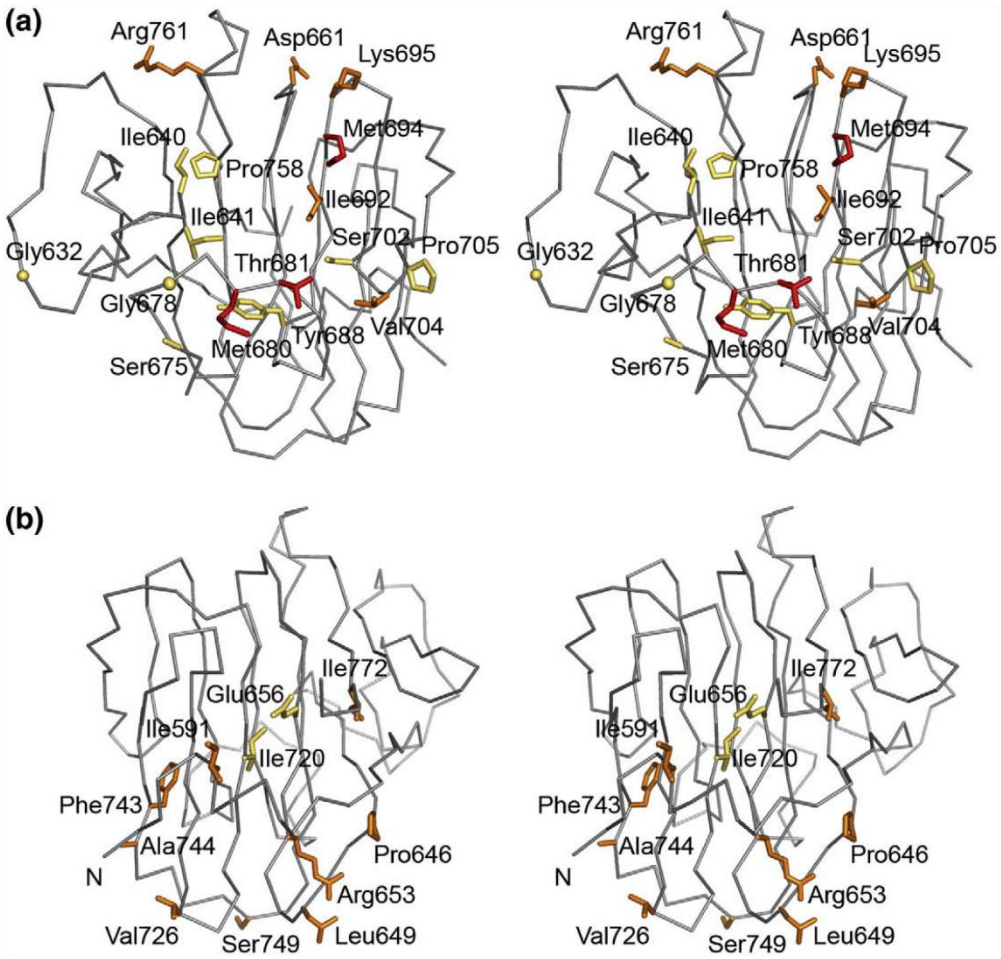

Fig. 5. Mutations of pyrin B30.2 that are associated with FMF (red, severe disease outcome; orange, mild disease outcome; yellow, unclassified). (a) Seventeen mutations map to the central cavity. The structure is shown in the standard orientation as defined in Fig. 1a. (b) Eleven mutations map to the hydrophobic core and the N-terminal surface. The structure in the standard orientation has been rotated approximately 180° around the vertical axis.

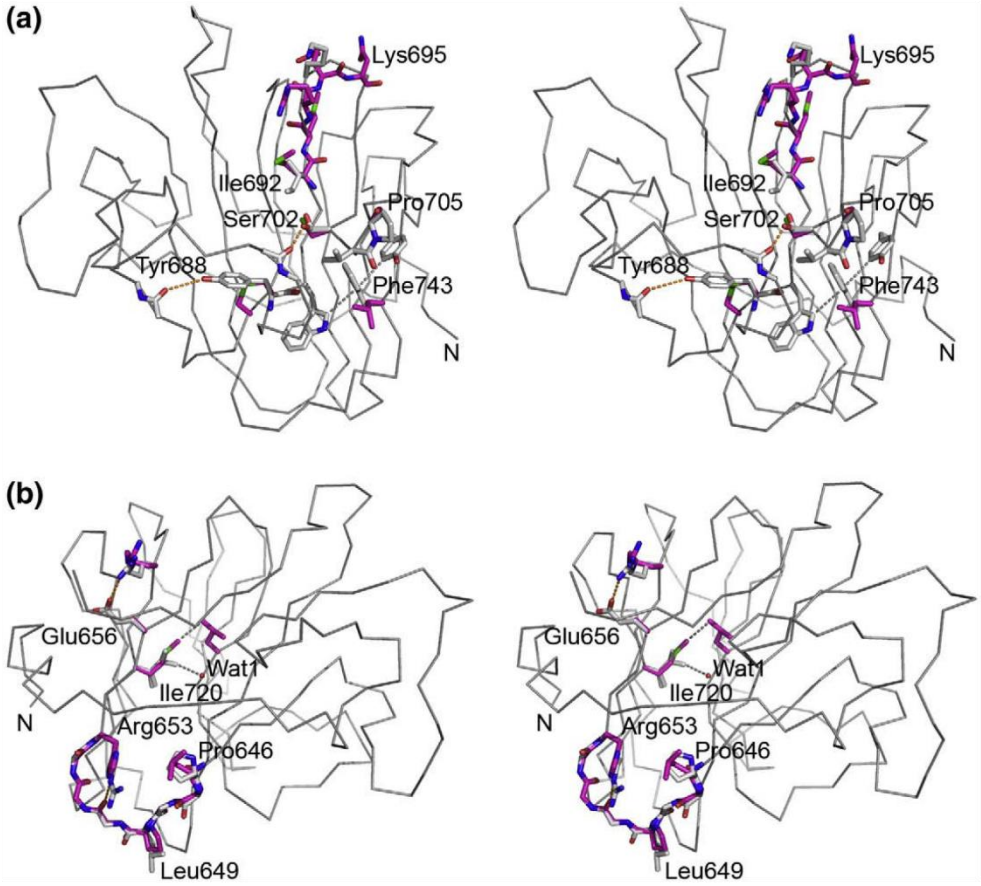

Fig. 6. Modelling of FMF-associated mutations at the central cavity (a) and the N-terminal site (b). Wild-type pyrin B30.2 is shown as a grey ribbon, and selected side chains as sticks with grey carbon atoms. Modelled FMF pyrin B30.2 is shown with magenta carbon atoms. Amino acids refer to the wild-type sequence. Dotted orange and grey lines refer to hydrogen bonds and general van der Waals contacts, respectively.

Glu656Ala

The side chain of Glu656 is completely buried, which is rather exceptional for a charged amino acid. However, Glu656 is conserved throughout all B30.2 structures that have been determined thus far. The charge of Glu656 is compensated by Arg717. The mutation Glu656Ala would disrupt this salt bridge and would destabilize the pyrin B30.2 structure (Fig. 6b).

Ser675Asn, Gly678Glu, Met680Ile, and Thr681Ile

Loop 5 contains four mutations, two of which are associated with severe FMF phenotypes. This loop is located at the rim of the central cavity, and it is most likely involved in direct recognition of the pyrin binding partner. This loop is extremely flexible. It adopts primarily two alternative conformations in the pyrin B30.2 structure. Gly678, which is conserved throughout all available B30.2 structures, adopts in both conformations dihedral angles that are forbidden for non-glycine residues ($\phi = 158°/\varphi = 170°$ and $\phi = 54°/\varphi = -161°$). Therefore, the Gly678Glu mutation is changing the main-chain conformation of loop 5. Mutations Met680Ile and Thr681Ile are associated with severe forms of FMF. In one conformation, the side chain of Met680 rests against the side chains of Phe636, Ile641, and Tyr688. The side chain of Thr681 is pointing into the solvent. The Thr681Ile mutation would render the binding pocket more hydrophobic.

Tyr688Cys

The side chain of Tyr688 is completely shielded from the solvent and stabilizes the bottom of the central cavity by forming a hydrogen bond with Ser675-O (3.65 Å) (Fig. 6a). The Tyr688Cys mutation eliminates this interaction. The side chain of the newly introduced Cys688 would be in a suitable position to form a disulfide bridge with Cys670 from the neighbouring β-strand. Therefore, the Tyr688Cys mutation would impose a different conformation of the active site loop 5.

ΔIle692, Met694Val, and Lys695Arg

These mutations are located at the C-terminal side of β-strand 6 and its subsequent β-turn (Fig. 6a). Particularly, mutations of Met694 are associated

with severe FMF phenotypes, suggesting that Met694 might be a key residue for substrate binding. Although the precise conformation of the B30.2/ligand complex is unknown, the structural similarity between pyrin and sRFPL1 B30.2 domains supports this hypothesis. Met694 is equivalent to Arg106 of sRFPL1, which is directly involved in the dimerization of sRFPL1.[22] The deletion of Ile692 is surprising, since Ile692 is located in the center of β-strand 6. This mutation is perhaps better described by an Ile692Met substitution and a deletion inside the following β-turn. This deletion is supported by the presence of two subsequent methionine residues at positions 693 and 694. In case of the ΔIle692 mutation, Met693 occupies the position of the isoleucine, Met694 occupies the Met693 binding pocket, and Lys695 moves closer towards the central cavity.

Ser702Cys, Val704Ile, and Pro705Ser

All three mutations are located in the loop that connects β-strands 7 and 8. Ser702 is one of two polar amino acids at the bottom of the central cavity. The side chain of Ser702 is located at hydrogen-bonding distance to Leu682-O. Although this distance is rather short (2.38 Å), the observation that Ser702 adopts two alternative conformations indicates that this hydrogen bond must be relatively weak. In addition, there is sufficient space to accommodate the bulkier mercapto group of Cys702 (Fig. 6a). The replacement of Pro705 against serine will have an impact on the main-chain conformation of loop 7 because Pro705 adopts a *cis*-peptide bond that would probably not be observed in the Pro705Ser mutant. Since loop 7 is involved in target binding in sRFPL1, the Pro705Ser mutant might directly affect the binding of the pyrin ligand.

Ile720Met

Ile720 is located in the center of the well-conserved hydrophobic core. The observation that Ile720 adopts two alternative conformations and the presence of an integral water molecule nearby (Wat1) illustrate that the hydrophobic B30.2 core is loosely packed (Fig. 6b). Therefore, the larger methionine side chain could be accommodated at this site, but Met720 would be placed at van der Waals distance to Leu667. Since Leu667 is located at the bottom of the central cavity, the Ile720Met mutation could affect ligand binding by subtle long-range distortions.

Phe743Leu

Phe743 is partially solvent accessible and rests against the main chain of Ser702. In addition, the side chain of Phe743 makes T-stacking interactions with the aromatic side chains of Trp689 and Tyr741 (Fig. 6a). Phe743 is conserved throughout all known B30.2 structures, suggesting that it might be important for the integrity of the fold. The Phe743-Leu mutation places an aliphatic side chain at this position, which is much less efficient in T-stacking than the aromatic side chain of Phe743.

Pro758Ser

Pro758 is located at the C-terminus of β-strand 12 right at the bottom of the central cavity. Ser758 could adopt the same main-chain conformation, but its polar side chain could also interact with either integral water molecules or other polar atoms nearby (e.g., Leu622-N), which could ultimately distort the conformation of loop 12.

In summary, the high-resolution pyrin B30.2 structure allows an accurate modelling of mutations that are associated with FMF. Unfortunately, the discussion of these mutations is hampered by the lack of information on pyrin B30.2 ligands.

Discussion

The 1.35-Å resolution crystal structure of pyrin B30.2 serves as a basis to understand the molecular principles that lead to FMF. Although no ligand is bound—except an ethylene molecule from the cryobuffer—the structural similarity between the B30.2 domains of pyrin, Trim21, and sRFPL1 as well as the distribution of FMF-associated mutations strongly suggests that the pyrin B30.2 ligand binds to the central cavity. sRFPL1 and Trim21 utilize ligand-specific hydrogen-bonding networks to distinguish between ligands that bind to the central cavities. However, all residues that form ligand-specific hydrogen bonds in sRFPL1 and Trim21 are replaced against hydrophobic amino acids in pyrin. Even though some key residues from Trim21 and sRFPL1 (such as Asp72 and Asp78, respectively) are conserved, the ligand conformations are significantly different. Since the central cavities between sRFPL1 and Trim21 are more similar compared to pyrin, the peptide binding mode of pyrin B30.2 will deviate significantly from the binding modes observed in sRFPL1 and Trim21.

In the pyrin B30.2 cavity, all key residues have been replaced against hydrophobic amino acids. Therefore, it is assumed that pyrin B30.2 recognizes its ligands through surface complementarities and hydrophobic interactions rather than direct hydrogen-bonding interactions involving side-chain contacts.

Residues that are associated with FMF cluster around two distinct sites. Most mutations, including those with the most severe disease outcomes, are located in direct vicinity to the central cavity. However, one third of all mutations are located on the opposite side of the central cavity, creating a second mutational hot spot. Due to the surface exposure of mutations in this secondary site, it is rather unlikely that these remote mutations disrupt the conformation of the central cavity by long-range interactions. The largest distance between FMF-associated mutations in B30.2 is observed between positions 591 and 632 (approximately 40 Å). Provided that both sites are in direct contact

with the pyrin B30.2 ligand, the ligand must have a very extended binding site. Pyrin binds via its N-terminal Pyd domain and ASC to NALP3.[3,14] NALP3 contains a leucine-rich repeat (LRR) domain consisting of nine repeats. Depending on the curvature of the LRR domain, nine repeats would be sufficient to span the distance between pyrin residues 591 and 632. Thus, from a pure structural point of view, NALP3 and pyrin could interact via their LRR and B30.2 domains, respectively.

A second possibility might be that pyrin B30.2 recognizes two different ligands utilizing two independent binding sites. NALP3 forms the building block of the inflammasome, a large macromolecular assembly that recruits procaspase-1 via the adaptor molecule ASC.[3] The spatial distribution of FMF mutations might indicate that pyrin B30.2 interacts with two components of the inflammasome. A third possible explanation of the clustering of FMF-associated mutations on opposite sites relies on the hypothesis that only mutations around the central cavity directly affect the binding of the B30.2 ligand, whereas mutations around the N-terminus modify the spatial orientation between the C-terminal B30.2 domain and the central coiled-coil domain. However, it is uncertain if the relative spatial orientations of B30.2 and coiled-coil domains have any functional implications. Thus, although the structural implications of FMF-associated mutations can be predicted, it is extremely difficult to deduce any functional consequences in the absence of detailed structural knowledge of pyrin binding partners.

Material and Methods

Expression and purification of the pyrin B30.2 domain

The B30.2 domain from the human *mefv* gene was cloned into a pGEX-6P vector (GE Healthcare) resulting in a GST-B30.2 fusion protein with a PreScission™ protease cleavage site in between. The B30.2 insert, coding for the C-terminal 204 amino acids of human pyrin (gene 16p13.3; *mefv*), was amplified by PCR from the full-length *mefv* gene with the primers 5′-GATCCCCGAATTCCTG-CGTTCAGAATG-3′ (sense) and 5′-GCGGCCGCT-CGAGTCAGTCAGGCCCCTGACC-3′ (antisense). Ligation into the pGEX-6P vector was performed using the EcoRI and XhoI restriction sites. The resulting GST fusion protein was named GST-pyr204 according to the length of the inserted pyrin fragment.

GST-pyr204 was expressed in *E. coli* BL21(DE3) cells. The cells were grown to an $OD_{600\ nm}$ of 0.6 at 30 °C and expression was induced with 0.1 mM IPTG. The expression was carried out at 18 °C for 16 h. The fusion protein was extracted from the soluble fraction of the lysate using a GSTrap-4B affinity chromatography column (5 ml; GE Healthcare) according to the manufacturer's protocol. GST-pyr204 was incubated at room temperature for 2 h with recombinant/GST-tagged PreScission Protease (GE Healthcare) to eliminate the GST protein. The protein was further purified by anion exchange chromatography [Resouce™ Q, 10 mM Tris–HCl, 0.5 mM tris(2-carboxyethyl)phosphine, 1% (v/v) glycerol (pH 9.0), gradient from 0 to 500 mM sodium chloride], which yielded highly pure pyr204 (pyrin residues 577–780).

Analysis of the oligomeric state of pyr204 was performed using a S75 Superdex size-exclusion chromatography (GE Healthcare), with 50 mM Tris–HCl, 50 mM NaCl, 0.5 mM tris(2-carboxyethyl)phosphine, 15% (v/v) glycerol (pH 7.5). The correct molecular weight of pyr204 was checked by mass spectrometry. Using the electrospray ionization time-of-flight method, a mass of 23,305 Da was measured (theoretical mass, 23,305.6 Da).

Crystallization and structure determination

Pyr204 was crystallized using the vapour diffusion method at 4 °C against a reservoir solution consisting of 0.2 M potassium thiocyanate, 25% polyethylene glycol 2000 monomethyl ether in a 0.1 M Tris/acetic acid buffer at pH 7.5 (Table 2). Crystals were obtained after 3 days and belonged to the hexagonal space group $P6_522$. A native data set of a pyr204 crystal was recorded at the X06SA beamline of the Swiss Light Source (Paul-Scherrer Institut, Villigen, Switzerland) at a resolution of 1.35 Å. The data were indexed, integrated, and scaled with XDS.[39] Molecular replacement was done with Phaser[40] using a polyalanine model of a truncated version of chain A of the B30.2 structure from sRFPL1 (pdb code 2FBE, residues 12–170)[22]. Initial refinement was done with Refmac (version 5.2.0019)[41] and finalized with Phenix.[42] Manual fitting was done using the program Coot.[43] The geometry

Table 2. Data collection and refinement statistics

Data collection	
Wavelength (Å)	1.0000
Space group	$P6_522$
Matthews coefficient	2.108
Corresponding solvent content (%)	41.6
Unit cell parameters: *a*, *b*, *c* (Å); α, β, γ (°)	60.27, 60.27, 182.03; 90, 90, 120
Resolution range (Å)	30–1.35 (1.50–1.35)
R_{sym}	8.8 (41.1)
$I/\sigma(I)$	18.2 (4.85)
Completeness (%)	94.4 (80.0)
Wilson *B*-factor (Å^2)	15.37
Refinement	
Resolution range (Å)	29.7–1.35 (1.38–1.35)
No. of reflections, working set	42,229 (1 346)
No. of reflections, test set	2130 (74)
R_{work} (%)	19.30 (30.93)
R_{free} (%)	21.86 (28.48)
No. of residues	191
No. of water molecules	162
No. of hetero molecules	2 SCN^-, 3 ethylene glycol
RMS deviation of bond lengths (Å)	0.010
RMS deviation of angle (°)	1.33
Overall mean *B*-factor (Å^2)	26.04
Validation	
Ramachandran plot (excl. Gly and Pro)	
Residues in most favored regions	165
Residues in additional allowed region	4
Ramachandran outliers	0

Values in parentheses are statistics from the highest-resolution shell.

$R_{sym} = \Sigma\,|I_{obs} - I_{avg}\,| / \Sigma\,|I_{obs}\,|$; I_{obs} is the observed intensity of the individual reflection and I_{avg} is the averaged intensity over symmetry equivalents.[38]

R_{free} is calculated with 5.0% of reflections which were not used for refinement.

and stereochemistry of the final structure were validated using the validation tools implemented in Coot and SFCHECK[44] as it was implemented into the CCP4 software package.

Accession numbers

Coordinates and structure factors have been deposited in the Macromolecular Structure database with accession number 2WL1.

Acknowledgements

We would like to thank Prof. J. Tschopp (University of Lausanne, Switzerland) for providing us with the DNA for the *mefv* gene. This work was financially supported by a Swiss National Science Foundation grant (no. 31-1022181 to M.G.G.).

References

1. Goldsby, R. A., Kindt, T. J. & Osbourne, B. A. (2000). *Kuby Immunology*. W. H. Freeman and Company, New York.
2. Martinon, F. & Tschopp, J. (2007). Inflammatory caspases and inflammasomes: master switches of inflammation. *Cell Death Differ.* **14**, 10–22.
3. Martinon, F., Burns, K. & Tschopp, J. (2002). The inflammasome: a molecular platform triggering activation of inflammatory caspases and processing of proIL-β. *Mol. Cell*, **10**, 417–426.
4. Thornberry, N. A., Bull, H. G., Calaycay, J. R., Chapman, K. T., Howard, A. D., Kostura, M. J. *et al.* (1992). A novel heterodimeric cysteine protease is required for interleukin-1β processing in monocytes. *Nature*, **356**, 768–774.
5. Eckelman, B. P., Salvesen, G. S. & Scott, F. L. (2006). Human inhibitor of apoptosis proteins: why XIAP is the black sheep of the family. *EMBO Rep.* **7**, 988–994.
6. Chae, J. J., Komarow, H. D., Cheng, J., Wood, G., Raben, N., Liu, P. P. & Kastner, D. L. (2003). Targeted disruption of pyrin, the FMF protein, causes heightened sensitivity to endotoxin and a defect in macrophage apoptosis. *Mol. Cell*, **11**, 591–604.
7. Chae, J. J., Wood, G., Masters, S. L., Richard, K., Park, G., Smith, B. J. & Kastner, D. L. (2006). The B30.2 domain of pyrin, the familial Mediterranean fever protein, interacts directly with caspase-1 to modulate IL-1β production. *Proc. Natl Acad. Sci. USA*, **103**, 9982–9987.
8. Papin, S., Cuenin, S., Agostini, L., Martinon, F., Werner, S., Beer, H. D. *et al.* (2007). The SPRY domain of Pyrin, mutated in familial Mediterranean fever patients, interacts with inflammasome components and inhibits proIL-1β processing. *Cell Death Differ.* **14**, 1457–1466.
9. Meroni, G. & Diez-Roux, G. (2005). TRIM/RBCC, a novel class of 'single protein RING finger' E3 ubiquitin ligases. *BioEssays*, **27**, 1147–1157.
10. Nisole, S., Stoye, J. P. & Saib, A. (2005). TRIM family proteins: retroviral restriction and antiviral defence. *Nat. Rev. Microbiol.* **3**, 799–808.
11. Henry, J., Ribouchon, M. T., Offer, C. & Pontarotti, P. (1997). B30.2-like domain proteins: a growing family. *Biochem. Biophys. Res. Commun.* **235**, 162–165.
12. Papin, S., Duquesnoy, P., Cazeneuve, C., Pantel, J., Coppey-Moisan, M., Dargemont, C. & Amselem, S. (2000). Alternative splicing at the MEFV locus involved in familial Mediterranean fever regulates translocation of the marenostrin/pyrin protein to the nucleus. *Hum. Mol. Genet.* **9**, 3001–3009.
13. Tidow, N., Chen, X., Muller, C., Kawano, S., Gombart, A. F., Fischel-Ghodsian, N. & Koeffler, H. P. (2000). Hematopoietic-specific expression of MEFV, the gene mutated in familial Mediterranean fever, and subcellular localization of its corresponding protein, pyrin. *Blood*, **95**, 1451–1455.
14. Richards, N., Schaner, P., Diaz, A., Stuckey, J., Shelden, E., Wadhwa, A. & Gumucio, D. L. (2001). Interaction between pyrin and the apoptotic speck protein (ASC) modulates ASC-induced apoptosis. *J. Biol. Chem.* **276**, 39320–39329.
15. Consortium, F. F. (1997). A candidate gene for familial Mediterranean fever. The French FMF Consortium. *Nat. Genet.* **17**, 25–31.
16. Aksentijevich, I., Torosyan, Y., Samuels, J., Centola, M., Pras, E., Chae, J. J. *et al.* (1999). Mutation and haplotype studies of familial Mediterranean fever reveal new ancestral relationships and evidence for a high carrier frequency with reduced penetrance in the Ashkenazi Jewish population. *Am. J. Hum. Genet.* **64**, 949–962.
17. Galeazzi, M., Gasbarrini, G., Ghirardello, A., Grandemange, S., Hoffman, H. M., Manna, R. *et al.* (2006). Autoinflammatory syndromes. *Clin. Exp. Rheumatol.* **24**, S79–85.
18. Yu, J. W., Wu, J., Zhang, Z., Datta, P., Ibrahimi, I., Taniguchi, S. *et al.* (2006). Cryopyrin and pyrin activate caspase-1, but not NF-κB, via ASC oligomerization. *Cell Death Differ.* **13**, 236–249.
19. Yu, J. W., Fernandes-Alnemri, T., Datta, P., Wu, J., Juliana, C., Solorzano, L. *et al.* (2007). Pyrin activates the ASC pyroptosome in response to engagement by autoinflammatory PSTPIP1 mutants. *Mol. Cell*, **28**, 214–227.
20. Jeru, I., Papin, S., L'Hoste, S., Duquesnoy, P., Cazeneuve, C., Camonis, J. & Amselem, S. (2005). Interaction of pyrin with 14.3.3 in an isoform-specific and phosphorylation-dependent manner regulates its translocation to the nucleus. *Arthritis Rheum.* **52**, 1848–1857.
21. Balci-Peynircioglu, B., Waite, A. L., Hu, C., Richards, N., Staubach-Grosse, A., Yilmaz, E. & Gumucio, D. L. (2008). Pyrin, product of the MEFV locus, interacts with the proapoptotic protein, Siva. *J. Cell Physiol.* **216**, 595–602.
22. Grutter, C., Briand, C., Capitani, G., Mittl, P. R., Papin, S., Tschopp, J. & Grutter, M. G. (2006). Structure of the PRYSPRY-domain: implications for autoinflammatory diseases. *FEBS Lett.* **580**, 99–106.
23. Woo, J. S., Imm, J. H., Min, C. K., Kim, K. J., Cha, S. S. & Oh, B. H. (2006). Structural and functional insights into the B30.2/SPRY domain. *EMBO J.* **25**, 1353–1363.
24. Woo, J. S., Suh, H. Y., Park, S. Y. & Oh, B. H. (2006). Structural basis for protein recognition by B30.2/SPRY domains. *Mol. Cell*, **24**, 967–976.
25. James, L. C., Keeble, A. H., Khan, Z., Rhodes, D. A. & Trowsdale, J. (2007). Structural basis for PRYSPRY-mediated tripartite motif (TRIM) protein function. *Proc. Natl Acad. Sci. USA*, **104**, 6200–6205.

26. Rhodes, D. A., de Bono, B. & Trowsdale, J. (2005). Relationship between SPRY and B30.2 protein domains. Evolution of a component of immune defence? *Immunology*, **116**, 411–417.
27. Ponting, C., Schultz, J. & Bork, P. (1997). SPRY domains in ryanodine receptors (Ca^{2+}-release channels). *Trends Biochem. Sci.* **22**, 193–194.
28. Bianchet, M. A., Ahmed, H., Vasta, G. R. & Amzel, L. M. (2000). Soluble β-galactosyl-binding lectin (galectin) from toad ovary: crystallographic studies of two protein–sugar complexes. *Proteins*, **40**, 378–388.
29. Touitou, I. (2001). The spectrum of Familial Mediterranean Fever (FMF) mutations. *Eur. J. Hum. Genet.* **9**, 473–483.
30. Aldea, A., Casademont, J., Arostegui, J. I., Rius, J., Maso, M., Vives, J. & Yague, J. (2002). I591T MEFV mutation in a Spanish kindred: is it a mild mutation, a benign polymorphism, or a variant influenced by another modifier? *Hum. Mutat.* **20**, 148–150.
31. Shinar, Y., Kuchuk, I., Menasherow, S., Kolet, M., Lidar, M., Langevitz, P. & Livneh, A. (2007). Unique spectrum of MEFV mutations in Iranian Jewish FMF patients—clinical and demographic significance. *Rheumatology (Oxford)*, **46**, 1718–1722.
32. Goulielmos, G. N., Fragouli, E., Aksentijevich, I., Sidiropoulos, P., Boumpas, D. T. & Eliopoulos, E. (2006). Mutational analysis of the PRYSPRY domain of pyrin and implications for familial mediterranean fever (FMF). *Biochem. Biophys. Res. Commun.* **345**, 1326–1332.
33. Sarrauste de Menthiere, C., Terriere, S., Pugnere, D., Ruiz, M., Demaille, J. & Touitou, I. (2003). INFEVERS: the Registry for FMF and hereditary inflammatory disorders mutations. *Nucleic Acids Res.* **31**, 282–285.
34. Dode, C., Pecheux, C., Cazeneuve, C., Cattan, D., Dervichian, M., Goossens, M. *et al.* (2000). Mutations in the MEFV gene in a large series of patients with a clinical diagnosis of familial Mediterranean fever. *Am. J. Med. Genet.* **92**, 241–246.
35. Bernot, A., da Silva, C., Petit, J. L., Cruaud, C., Caloustian, C., Castet, V. *et al.* (1998). Non-founder mutations in the MEFV gene establish this gene as the cause of familial Mediterranean fever (FMF). *Hum. Mol. Genet.* **7**, 1317–1325.
36. Booth, D. R., Gillmore, J. D., Booth, S. E., Pepys, M. B. & Hawkins, P. N. (1998). Pyrin/marenostrin mutations in familial Mediterranean fever. *QJM*, **91**, 603–606.
37. Medlej-Hashim, M., Salem, N., Chouery, E., Rawashdeh, M., Delague, V., Haffar, M. *et al.* (2002). Familial Mediterranean fever: the potential for misdiagnosis of E148V using the E148Q usual RFLP detection method. *Clin. Genet.* **61**, 71–73.
38. Diederichs, K. & Karplus, P. A. (1997). Improved *R*-factors for diffraction data analysis in macromolecular crystallography. *Nat. Struct. Biol*, **4**, 269–275.
39. Kabsch, W. (1988). Evaluation of single crystal X-ray diffraction from a position-sensitive detector. *J. Appl. Crystallogr.* **21**, 916–924.
40. McCoy, A. J., Grosse-Kunstleve, R. W., Storoni, L. C. & Read, R. J. (2005). Likelihood-enhanced fast translation functions. *Acta Crystallogr., Sect. D: Biol. Crystallogr.* **61**, 458–464.
41. Murshudov, G. N., Vagin, A. A., Lebedev, A., Wilson, K. S. & Dodson, E. J. (1999). Efficient anisotropic refinement of macromolecular structures using FFT. *Acta Crystallogr., Sect. D: Biol. Crystallogr.* **55**, 247–255.
42. Adams, P. D., Grosse-Kunstleve, R. W., Hung, L. W., Ioerger, T. R., McCoy, A. J., Moriarty, N. W. *et al.* (2002). PHENIX: building new software for automated crystallographic structure determination. *Acta Crystallogr., Sect. D: Biol. Crystallogr.* **58**, 1948–1954.
43. Emsley, P. & Cowtan, K. (2004). Coot: model-building tools for molecular graphics. *Acta Crystallogr., Sect. D: Biol. Crystallogr.* **60**, 2126–2132.
44. Vaguine, A. A., Richelle, J. & Wodak, S. J. (1999). SFCHECK: a unified set of procedures for evaluating the quality of macromolecular structure-factor data and their agreement with the atomic model. *Acta Crystallogr., Sect. D: Biol. Crystallogr.* **55**, 191–205.

3 Manuscript: Structural consequences of FMF associated mutations in the pyrin B30.2 domain.

Title

Structural consequences of FMF associated mutations in the pyrin B30.2 domain

Authors

C. Weinert[1,#], D. D. D. Possner[2,#], P. M. G. Mittl[1], M. G. Grütter[1,3]

Affiliations

# These authors contributed equally to the work

[1] Departement of Biochemistry, University of Zurich, Winterthurerstrasse 190, CH-8057 Zürich

[2] Current address: Division of Molecular Structural Biology, Department of Medical Biochemistry and Biophysics, Karolinska Institutet, Tomtebodavägen 6, 4tr, Stockholm S-171 77, Sweden.

[3] to whom correspondence should be addressed: gruetter@bioc.uzh.ch, Tel. +41-44-6355580, Fax. +41-44-6356834

Keywords

B30.2 domain, SPRY, PRYSPRY, pyrin, TRIM20, FMF, mutational analysis, M694V, crystal structure, auto-inflammatory disease

Abbreviations

NLRP3: NLR family, pyrin domain containing protein 3, PSTPIP1: Proline-Serine-Threonine Phosphatase Interacting Protein 1**,** AIM2: absent in melanoma 2, caspase 1: cysteine-aspartic acid dependent protease 1, LPS: Lipopolysaccharide, MDP: Muramyl dipeptide, dsDNA: double stranded deoxyribonucleic acid; IgG: Immunoglobulin G

Abstract

Familial Mediterranean Fever (FMF) is a recessively inherited auto-inflammatory disorder characterized by recurrent episodes of fever. The gene responsible, *MEFV*, encodes a 781 amino acid multi-domain protein called pyrin/TRIM20. Throughout the gene more than 120 FMF related mutations have been identified, however the most frequently occurring mutations reside in the C-terminal B30.2 domain that acts as a ligand binding domain. Structures of homologous B30.2 domains in complex with ligands revealed their common binding epitope created by variable loops and an enclosed cavity on the concave β-sheet. Residues creating this putative binding interface in pyrin are frequently mutated in FMF patients suggesting an alteration of the binding mode of the pyrin B30.2 domain.

To elucidate the structural consequences induced by FMF related mutations, we have determined the crystal structures of five mutants. We focused on mutations positioned in one variable loop as well as on mutations on the β-sheet where the most prominent mutation, M694V, is located.

The mutations do not lead to changes in the overall structure of the B30.2 domain but manifest in local changes of the binding interface. Mutations located on the β-sheet lead to a reshaped central cavity and changes in the electrostatic surface potential of the epitope. Mutations found within the variable loop-5 affect the conformational flexibility of loop-5 and the adjacent loop-2. Whereas the mutation M680L stabilizes loop-5 in a distinct conformation the mutation G678V reveals the importance of a hydrogen bond network formed between loop-2 and -5. Once the network is broken loop-2 experiences a greater flexibility, disclosing the possibility of a communication between the loops.

Introduction

The autosomal recessive disorder Familial Mediterranean Fever (FMF) is characterized by recurrent episodes of fever, usually accompanied with serositis in the peritoneum, pleura and synovium[1]. The self-limiting attacks normally last for 12 to 72h and are intermitted by symptom-free periods of weeks to months. FMF is mostly found in ethnics around the Mediterranean basin, namely Jews, Armenians, Turks and Arabs[2]. If untreated with colchicine, FMF patients can develop amyloidosis which eventually leads to renal failure[1]. In 1997, two FMF consortia have identified the gene responsible for FMF, *MEFV*[3,4]. The 3.5kb gene is located on chromosome 16 consisting of 10 exons and encodes a 781 amino acid protein that was named pyrin. A growing number of FMF associated mutations have been identified throughout the gene, however the most frequent mutations are clustered in exon 10[5-12].

Pyrin is a multidomain protein that belongs to the tripartite motif-containing (TRIM) family of proteins, and is therefore also called TRIM20[13]. As most TRIM proteins, pyrin contains a C-terminal B30.2 (PRYSPRY/SPRY) domain that in case of pyrin is encoded by exon 10[14]. Two opposing functions are suggested for pyrin, namely the inhibition and activation of innate immune signaling.

The recognition of danger associated molecular patterns (e.g. , extracellular ATP or reactive oxygen species) by the NOD-like receptor NLRP3 triggers the formation of a large cytoplasmic complex called NLRP3-inflammasome[15]. This complex leads to the activation of the inflammatory protease caspase-1 that subsequently cleaves Pro-Interleukin-1β (pro-IL-1β). Mature IL-1β is secreted and acts a major pro-inflammatory cytokine[16]. Through its B30.2 domain pyrin can interact both with caspase-1 and pro-IL-1β thus inhibiting IL-1β maturation[17].

In certain cellular challenges pyrin can act alone as an inflammasome and initiate the maturation of IL-1β[18-22]. The formation of a pyrin inflammasome can be induced by disease associated mutants of the Proline-Serine-Threonine Phosphatase Interacting Protein 1 (PSTPIP1), a *Burkholderia cenocepacia* infection or by ribotoxic-stress. As for NLRP3, the formation of a pyrin inflammasome leads to caspase-1 activation and IL-1β maturation. The effect of FMF related mutations in pyrin in either anti- or pro-inflammatory function has not been elucidated or is contradictory (see references above).

As the most frequent mutations occurring in FMF are clustered in the C-terminal B30.2 domain, we have recently determined its crystal structure to identify the locations of the mutations and provide a structural basis for the mutant effect[23]. The B30.2 domain of pyrin folds into two antiparallel β-sheets which are connected in a jellyroll like topology, as seen for all B30.2 domains[24-27]. The variable loops and the enclosed central cavity were shown to create the domain typical binding epitope and confer the specificity for ligand binding[24,29,30]. Mapping the FMF

associated mutants on the pyrin B30.2 structure showed that most of them superimpose with the commonly found epitope and define a putative binding interface for pyrin[23]. This includes two hotspots where mutations are associated to a severe phenotype. One hotspot is the methionine 680 (M680) located in loop-5, which has been found to be mutated to isoleucine or leucine (M680I,L) in about 13% of the sequenced alleles of FMF patients[6-12,28]. The second hotspot harbors the most frequently mutated residue methionine 694 (found in over 50% of the alleles) and resides in β-strand 6 located at the rim of the central binding cavity. Mutations of M694 to valine, leucine, isoleucine or a deletion (M694V,I,L,del) are all associated with FMF, where the mutant M694V is associated to a severe phenotype with increased risk of developing amyloidosis, the most severe effect of FMF which can ultimately lead to renal failure[29,30].

In order to elucidate the structural changes in these two hotspots that confer a FMF phenotype, we have solved the crystal structures of several FMF related mutants, namely G678V, M680L, I692del and M694V. The mutant structures reveal the distinct kind of alterations that lead to modifications in the binding characteristics of the pyrin B30.2 domain.

Materials and Methods

Expression and purification of B30.2 domain mutants

Mutants were generated using QuikChange mutagenesis (Invitrogen™, United States) using the previously reported construct of the pyrin B30.2 domain (coding for residues 578-781) in a pGEX-6P-1 vector (GE Healthcare, United States)[23]. Correct mutagenesis was confirmed by DNA sequencing. The mutants were expressed as a GST-fusion protein and purified as described[23]. Briefly, the mutants were expressed in *Escherichia coli* BL21(DE3) cells. Cultures were grown to an OD_{600nm} of 0.6 at 30 °C and protein expression was induced with 0.1 mM or 0.5 mM IPTG for mutants I692del, M694V and R653H, G678V, M680L, respectively. The expression was carried out at 18 °C for 18 h. Cells were harvested (4000 g, 20 min) and the pellet resuspended in lysis buffer (50 mM Tris-HCl, pH 7.5, 300 mM NaCl, 20 mM NaH_2PO_4, DNase 1, 0.5 mg/ml lysozyme) and lysed using an Emulsi-Flex C3 homogenizer (Avestin, Canada). The lysate was cleared by centrifugation (20 000 g, 45 min) and the fusion protein extracted from the soluble fraction using a GSTrap 4B affinity chromatography column (5 ml; GE Healthcare, United States) according to the manufacturer's protocol. The fusion protein was digested by incubation with recombinant/GST-tagged PreScission Protease (GE Healthcare) and simultaneous dialysis against PreScission protease cleavage buffer (50 mM Tris-HCl, pH 7.5, 150 mM NaCl, 1 mM EDTA, 0.5 mM TCEP), followed by reapplication onto a GSTrap 4B affinity column to remove the GST and protease. The mutants were further purified by anion exchange chromatography (Resource™ Q, 10 mM Tris-HCl pH 9.0, 0.5 mM TCEP, 1 % (v/v) glycerol, gradient

from 0 to 500 mM sodium chloride), and the oligomeric state was analysed using a Superdex 75 10/300 size exclusion chromatography column (GE Healthcare; 50 mM Tris-HCl, pH 7.5, 50 mM NaCl, 0.5 mM TCEP, 10 % (v/v) glycerol).

Crystallisation and structure determination

All mutants were concentrated to 10 mg/ml and crystallized using the sitting drop vapour diffusion method. The crystallisation conditions for R653H, G678V, M680L, I692del and M694V were [0.1 M Na-Acetate, pH 5.5. 0.2 M KSCN, 25 % (w/v) PEG 2k MME, 4 °C], [0.1 M Tris-AcOH, pH 7.4, 0.2 M KSCN, 23.3 % (w/v) PEG 2k MME, 20 °C], [0.1 M Tris-AcOH, pH 8.0, 0.2 M KSCN, 23.3 % (w/v) PEG 2k MME, 20 °C], [0.1 M Tris-AcOH, pH 7.6, 0.2 M KSCN, 30 % (w/v) PEG 2k MME, 20 °C] and [0.1 M Tris-AcOH, pH 7.5, 0.2 M KSCN, 25 % (w/v) PEG 2k MME, 20 °C], respectively. Prior to freezing the crystals were briefly soaked in a cryoprotectant solution consisting of the mother liquor supplemented with 10 % ethylene glycol. Native data sets of the mutants were recorded at the X06SA or X06DA beamline at the Swiss Light Source (PSI, Villigen, Switzerland). While the mutants G678V, I692del and M694V crystallized in the same space group as the wild type ($P6_522$), mutants R653H and M680L crystallized in space group $P2_12_12_1$. Data were indexed, integrated and scaled with *XDS*[31]. For mutants R653H and M680L, molecular replacement was performed using *Phaser* with the wild type structure as search model[32]. Structures were refined using *Phenix* and *Refmac* and manually edited using *Coot*[33-35].

Structure analysis

Structures were analysed with the in-built structure comparison tool in *Phenix*. The electrostatic surface potential was created using the Adaptive Poisson-Boltzmann Solver plugin (version 2.0) implemented in *PyMOL* (Schrödinger, LLC)[36]. PQR files were generated using the *PDB2PQR* server[37].

Sequence alignment

Sequences used correspond to the UniProt entries O15553, Q9C035, Q9C029, P19474, Q8IYM9, P14373, Q8NG06, Q9BVG3 and Q86WT6 for pyrin, TRIM5α, TRIM7, TRIM21, TRIM22, TRIM27, TRIM58, TRIM62 and TRIM69 respectively. Alignment was generated using T-coffee[38] and Jalview[39].

Results

We solved the crystal structure of the mutants R653H, G678V, M680L, I692del and M694V (see Fig. 1). All mutants displayed monomeric behavior when analyzed by size exclusion chromatography (data not shown). Whereas the mutants M694V, I692del, and G678V all crystallized in the same space as the wild type, namely $P6_522$ the mutants R653H and M680L crystallized in space group $P2_12_12_1$ (for data collection and refinement statistics see Suppl. Table1+2). Both crystal forms contained one molecule in the asymmetric unit. The achieved resolutions for the

structures are between 1.5 Å for the R653H mutant and 2.4 Å for the G678V mutant. The overall structural changes are small with root mean square deviations (rmsd) of the backbone between 0.163 Å for the M694V mutant and 0.482 Å for the I692del mutant (see Suppl. Table 2).

Mutations within loop-5

In the previously determined wild type structure loop-5 (loop-5-wt) was weakly defined and could not be traced in a defined conformation, which is attributed to its flexibility[23]. A mutation distantly located from loop-5 is R653H. However, loop-5 of this mutant structure (loop-5-R653H) is present in a distinct conformation which is probably due to the crystallization of the mutant in $P2_12_12_1$ compared to $P6_522$ for the wild type (Suppl. Fig. 1A+B). Nevertheless loop-5-R653H still shows a 3-fold increased temperature factor (i.e. flexibility) compared to the mean temperature factor of the whole molecule confirming the intrinsic flexibility of this loop.

The mutant structure of the hotspot mutation M680L, residing in loop-5, also crystallized in space group $P2_12_12_1$ and is therefore compared to loop-5-R653H. The mutation of M680L leads to a different orientation of the side chain of residue 680 with consequences for the entire loop-5 (see Fig. 2A). While the wild type M680 is pointing into the solvent and is flexible, L680 points towards a hydrophobic patch created by residues F636, I641 of loop-2 and I674, L682 and Y688 of loop-5. The packing of L680 into the hydrophobic patch results in a defined rotamer of the side chain, as manifested by its well defined electron density and to significant lower temperature factors of loop-5-M680L compared to loop-5-R653H (see Fig. 2E and Suppl. Fig. 1B+C). The different orientation of the leucine side chain compared to the wild type methionine also leads to small differences of backbone trace for residues K677 to T681.

Notably, both the side chain of L680 and the backbone of the entire loop-5-M680L adopts a similar conformation as the corresponding F369 and loop-5 in the structure of the ligand bound B30.2 domain of pyrin homologue TRIM21, in which the side chain also orients towards the hydrophobic patch (see Fig. 2B).

The differences between loop-5 in the two different space groups are small, but loop-5-R653H and loop-5-M680L form a larger and more defined hydrogen bond network with loop-2 (see Fig. 2C). Residues R676, K677 and G678 of loop-5 form hydrogen bonds through their side and main chain atoms to residues of loop-2 with a coordinated water molecule between the loops. The involved residues in loop-2 (G632-C639) contribute almost exclusively with their backbone atoms to the hydrogen bond network. Loop-5-wt differs most in the position of G678, which can not be localized in the wild type and therefore does not contribute to the hydrogen bond network. Also K677 and the coordinated water are less well defined compared to the mutant structures (see Suppl. Fig. 1A-C). A possible consequence of the enlarged hydrogen bond network in the mutant structures is the stabilization of loop-2 as seen by its improved definition of the electron density compared to the

wild type (see Suppl. Fig. 2). A detailed summary of the hydrogen bond network is given in the Supplementary Information which also includes the B30.2 domain of TRIM21, where the same hydrogen bond network is seen (see Suppl. Table. 3)[25]. Additionally, the RKG motif of loop-5 is conserved among some members of the TRIM family (Suppl. Fig. 3).

In both space groups, the Φ and Ψ angles of G678 of the RKG motif are in a Ramachandran plot region which is not allowed for non-glycine residues. The mutation of this residue to valine (G678V) is rare but associated to FMF (Infevers registry[5]). Similar to the wild type structure, loop-5 is weakly defined revealing that a hydrophobic residue at this position, compared to residue 680, does not alter the flexibility of loop-5. In comparison to loop-5-wt, there is no electron density seen for the side chain of R676. However the backbone of loop-5 can be traced at a lower σ-cutoff of 0.8. Through the mutation to valine, whose Ramachandran restraints are more limited, the backbone conformation for residues V678 and N679 is changed (see Fig. 3A). The two residues are further apart from loop-2 and point into the solvent leading to a complete loss of the hydrogen bonds between loop-2 and -5 also lacking the coordinated water molecule. The lack of interaction between both loops results in a destabilized loop-2 with no apparent electron density for residues 626-634. Also residues 639-634 show an increased flexibility in the G678V mutant structure as judged from the increased temperature factors for these residues as compared to the wild type (see Fig. 3B). This is particularly pronounced for the phenylalanine at position 636. This residue is part of the aforementioned hydrophobic patch formed between the two loops and is a highly conserved residue in the B30.2 domain of TRIM proteins (see Suppl. Fig. 3). These results suggest that the RKG motif is an important motif to stabilize loop-2, and that this stabilizing effect is lost in case of a G678V mutation.

Mutations in β-strand 6

The second hotspot region associated with FMF is β-strand 6 (β-6) located on the concave surface of the β-sandwich. This strand is creating the rim of the central cavity in the putative binding interface. In the B30.2 domain of TRIM21, residues of β-6 are key residues in the interaction with the IgG[25]. In pyrin, a mutation of M694 to valine induces a strong phenotype and is correlated with the development of amyloidosis. Structurally, the mutation exhibits the smallest changes among all studied mutants with an rmsd of the backbone of 0.163 Å compared to the wild type. The mutation to valine induces structural changes that are limited to the side chains of residues 694, 695 and 698 (see Fig. 4A). While in the wild type the longer M694 is pointing into the central cavity, the Cγ1 of the Cβ-branched valine is directed towards K695 that introduces minor changes in the neighboring residues. The side chain of K695 is flexible in the wild type structure. In the M694V mutant structure the lysine side chain seems to be stabilized as its position is defined by the experimental electron density. The same effect is seen for the glutamate 698, which side chain is clearly defined in the M694V mutant (not illustrated). Due to the

smaller valine in the M694V mutation the central binding cavity becomes slightly larger but no apparent changes in the electrostatic surface potential are seen (see Fig. 4C). The severity of the associated phenotype compared to small local changes suggests that M694 is a key residue in the interaction with pyrin's putative ligand.

As M694, I692 is located in β-6 (res. 687-695), which runs antiparallel to β-7. The I692del mutation induces a register shift of one amino acid, by pulling residues C-terminal of V691 in the N-terminal direction (see Fig. 4B). The analysis of the hydrogen bonds present between β-6 and β-7 reveal that the register shift is limited to β-6. Whereas in the wild type the E698 of β-7 forms an "irregular" hydrogen bond pattern with both the amide of M694 and the carbonyl of K695, it forms both hydrogen bonds to the lysine residue (K694) in the deletion mutant creating a hydrogen bond pattern typical for anti-parallel β-sheets. As a consequence β-6 is shortened by one residue and the adjacent β-turn is positioned closer towards the central cavity. The sequence of the β-6 is changed from Ile-Met-Met-Lys (res. 692-695) in the wild type to Met-Met-Lys (res. 692-694) in the deletion mutant. The resulting changes in the surface exposed side chains and the shortening of the β-6 have an impact on both the shape and the electrostatic surface potential of the central cavity. The pronounced rim created by M694 is lost and the central cavity reshaped. In addition, through the replacement of the hydrophobic M694 by a charged lysine the rim of the central binding pocket becomes more positively charged (see Fig. 4C). The I692del mutation also resembles anM694del mutation because the β-6 gets shortened by this specific residue.

Local effects of the R653H mutation

Although not located in the putative binding interface a R653H mutation confers a mild phenotype. An arginine at this position is rather rare throughout the B30.2 domains of TRIM proteins, while a histidine at this position is conserved (see Suppl. Fig. 3). The shorter histidine at this position leads to the loss of a hydrogen bond to S650 (see Fig. 5A). The wild type arginine binds through its guanidinium group both to the carbonyl oxygen as well as to the hydroxyl oxygen of S650. The histidine only mediates a hydrogen bond to the main chain oxygen. A probably larger effect of this mutation is the resulting change in the electrostatic surface potential. Whereas the arginine is positively charged, the histidine is negatively charged at physiological conditions (see Fig. 5B).

Discussion

The B30.2 domains are protein binding domains that interact with various different targets[41]. The common binding interface is defined by variable loops enclosing a central binding pocket, which confers the ligand specificity for each B30.2 domain. As most of FMF associated mutations map to the common binding interface, it is thought that these mutations alter the binding behavior of the B30.2 domain to its

ligand(s). Due to the severe phenotype associated with different mutations, two hotspot regions within this interface have been postulated[29].

We solved the crystal structure of five B30.2 domain mutants, which are associated with an FMF phenotype. Their structural changes are local such as changes in the shape of the central binding cavity (I692del, M694V) and alterations in the electrostatic surface potential (I692del, R653H) but also affect entire loops in their flexibility (M680L) as well as conformation (G678V).

The hotspot mutation in loop-5, M680L, rigidifies the loop it is positioned in through the binding of the leucine side chain to the hydrophobic patch between loops -2 and -5. The same effect can be suggested for the more often occurring FMF mutant M680I. The loop-5 of TRIM21 has similar characteristics as found in the pyrin M680L mutant by having a stable conformation of this loop. As the B30.2 domain of TRIM21 is thought to bind to the IgG in a lock-and-key mode, i.e. without undergoing large structural changes upon ligand binding, a rigid loop conformation is probably a prerequisite for high affine binding[26,42]. In wild type pyrin however this loop requires some conformational flexibility for its correct function, which is altered.

Our mutant study reveals the importance of the interactions between loop-2 and 5. Both mutants that crystallized in space group $P2_12_12_1$ show a well defined hydrogen bond network between these two adjacent loops that involves the residues RKG of loop-5. This network of hydrogen bonds is also seen in TRIM21, and judging from the sequence alignment is probably also present in homologous B30.2 domains due to the conservation of the amino acids RKG. By disrupting the hydrogen bond network created by the RKG motif in loop-5, loop-2 can be markedly affected and becomes more flexible as seen in the G678V mutant structure. Through a conformational change of loop-5 the interactions to loop-2 are lost resulting in an increased flexibility of loop-2 that is partly not traceable in the crystal structure of the G678V mutant. The loss of interaction between the loops also results in an increased mobility of phenylalanine 636 that is part of the hydrophobic patch between the loops. This phenylalanine has been suggested to play a crucial role in hooking loop-2 to the compact B30.2 domain fold, as its replacement from the hydrophobic patch between loop-2 and -5 leads to very mobile loop-2 as seen in the structure of the rhTRIM5α B30.2 domain (Ivanov, Cold Spring Habor Meeting on Retrovirus, 2013)[26]. In summary, the conserved RKG motif and the participation of F636 in the hydrophobic patch lead to a distinct conformation of loop-2 and -5.

With respect to the effect of the FMF mutation G678V in pyrin, two plausible consequences can be suggested. First, the conformational space for loop-5 is altered due to the restriction of valine with respect to the backbone dihedral angles, therefore altering the contribution of this loop to ligand binding. A second consequence could be the increased flexibility of loop-2. Although no severe

mutations are located in loop-2, it contributes to the binding in case of TRIM5, TRIM21 and also in the further distant related B30.2 like domain (SPRY domain) of GUSTAVUS[44] and changes in the flexibility of loop-2 of pyrin might change the binding affinity.

Due to the intrinsic flexibility of loop-5 in pyrin as seen in the wild type structure and its putative involvement in ligand binding, a possible communication between these loops can be suggested. One can imagine that upon ligand binding loop-5 is rearranged in such a way that a change in the hydrogen bond network is induced, resulting in a greater flexibility of loop-2. The reduced intrinsic flexibility in case of the M680L mutant might inhibit such a communication. As a methionine at this position is thought to have evolved during evolution[43], this might also introduced a possible communication between the loops.

M694V harbors one of the most abundant mutations in FMF patients and is associated to a severe phenotype. However, the changes in the M694V mutant are very subtle. The exchange from methionine to valine only affects the side chain of this residue. As the residue 694 is creating a rim of the central cavity, a M694V mutation alters the shape of the central cavity. This suggests that the side chain of M694 is crucial for the interaction of pyrin with its ligand probably because it is directly involved in the interaction as observed for the corresponding residue in TRIM21.

A larger influence is seen for the I692del mutant due to the shortening of β-6. This mutation is considered to confer mild FMF symptoms[29]. As the M694 seems to be crucial for a correct function of pyrin, the effect of the mutation is probably exerted by the exchange of M694 by R694 with the resulting change in the shape and electrostatic surface potential of the central cavity. In this mutant the β-6 is shortened by residue 694, therefore a similar effect can be suggested for the M694del mutant, which would again lead to an lysine residue at position 694. This mutant is associated with a severe phenotype and, apart from still containing the native isoleucine at position 692, is probably structurally highly similar to the I692del[29].

A residue not superimposing with the reported binding interfaces of other B30.2 domains is R653. However, a mild phenotype is associated with mutations at this position, suggesting that the pyrin B30.2 domain has more than one binding interface[7,23,40]. Interestingly, only human, gorilla and chimpanzee carry an arginine at this position, while other primates carry a conserved histidine[43]. The same is true for B30.2 domains of human TRIM proteins, where a histidine is conserved. The R653H mutant shows the same local structural features as TRIM5α, which has a histidine at this position. The major effect of this mutation is a change in the electrostatic potential that might alter the interaction with a ligand. However, no specific function for the histidine or arginine at this position has not yet been assigned in any B30.2 domain.

Several binding partners are proposed for the B30.2 domain, including pro-IL-1β, caspase-1 and the nucleotide-binding domain of the NLRP1-3[17,45]. Pyrin has also been associated to both anti- as well as pro-inflammatory functions and it is therefore hard to speculate about the precise effect of the mutants on function. However, our data reveal that the structural changes induced by FMF associated mutations locally affect the shape of the central cavity, but also alter the conformational flexibility of entire loops. For a correct binding mode of the B30.2 domain of pyrin, not only the shape of the cavity in crucial, but also a flexible loop-5 and a stabilized loop-2 are prerequisites for ligand binding.

Acknowledgement

We would like to thank the late Prof. J. Tschopp (University of Lausanne, Switzerland) for providing us with the DNA for the *MEFV* gene. We also thank Beat Blattmann and Celine Stutz-Ducommun of the NCCR crystallisation facility and the staff of the Swiss Light Source, Villigen, Switzerland. CW is participant of the Biomolecular Structure and Function PhD program of the NCCR Structural Biology. This work was financially supported by a Swiss National Science Foundation grant (No. 31-1022181 to M.G.G.).

Figures legends

Figure 1

The B30.2 domain is shown in a cartoon representation. The positions of the mutations, of which the crystal structures have been determined in this study, are indicated by orange spheres. The affected loops and β-sheets are labeled according to Weinert et al.[23]. Structural elements labeled in red indicate their involvement in putative ligand binding. The chosen perspective serves as a reference for subsequent figures.

Figure 2

Stereo representation of the structural features of loop-5 shown for the individual mutants M680L and R653H: A) The mutant M680L crystallized in the same space group as R653H. Both structures are superimposed and presented in the orientation as indicated in D. The R653H and M680L mutant structures are shown in purple and orange stick, respectively. Only hydrogen bonds between loop-2 and -5 that are found to be different are indicated in dashed lines according to the color of each mutant structure. B) The mutant M680L was superimposed with the B30.2 domain of TRIM21 that was solved in complex with an IgG (pdb-code: 2iwg). The M680L is colored as in A and the TRIM21 B30.2 domain in white sticks. The coordinated water (red sphere) and the hydrogen bond network (dashed lines) are shown only for the M680L mutant, but are comparable for TRIM21 C) The conformation of loop-5 and the adjacent loop-2 of mutant R653H is superimposed with the wild type structure. Both structures are shown in a stick representation and colored green and purple for the wild type and the R653H mutant, respectively. Hydrogen bonds found in the R653H mutant are indicated as black dashed lines. The coordinated water molecule is shown as a red sphere. For simplicity only one of the two conformations seen in the wild type structure is presented. D) Standard view of the B30.2 domain as in Figure 1. The residues depicted in Fig.2 A-C are colored in orange and the chosen viewpoint is indicated. E) Normalized B-factors of the protein backbone are shown for residues of loop-5 of mutants R653H (resembling the wild type) and M680L in purple and orange, respectively.

Figure 3

Structural effects of the G678V mutation. A) Superimposed loop-5 and loop-2 are shown in a stereo representation for the wild type and the G678V mutant structure in green and in orange, respectively. B) The normalized B-factors are plotted in green and orange for loop-2 residues of the wild type and G678V, respectively. Indicated is the position of the Phe636 that plays a crucial role for the fixation of loop-2. Residues 626-633 could not be traced in the electron density of the G678V mutant structure. The view is identical as in Figure 2.

Figure 4

Structural features of mutations in β-strand 6: A) Stereo view of the M694V mutant structure compared to the wild type is shown for β-strand 6 and 7 in a stick representation. Wild type and M694V mutant are colored green and orange, respectively. B) The same close up view of β-strand 6 and 7 for superimposed wild type and I692del mutant structure colored in green and orange, respectively. The hydrogen bond network between the two strands is indicated by dashed lines in the corresponding color and schematically illustrated on the right. C) The electrostatic surface potential for wildtype, M694V and I692del mutant structures are displayed between -5 kT/e and 5 kT/e.

Figure 5

Structural and electrostatic changes introduced by the R653H mutation. A) Loop-3 is superimposed and illustrated in green and orange sticks for the wild type and the R653H mutant, respectively. The hydrogen bonds between Ser650 and R653 or H653 are indicated by dashes in the according color. B) The change of the positively charged arginine to the more negatively charged histidine is visualized by the electrostatic surface potential of wild type (on the left) and mutant (on the right) between -5 kT/e and 5 kT/e. On the right, residues depicted in A are colored orange and the chosen viewpoint indicated.

Supplememtary Figure 1

Changes in the electron density of loop-5. Loop-5 of wild type (2wl1) (A), the R653H (B) and M680L (C) structure are shown in sticks in green, purple and orange, respectively. In all structures the electron density for residues 674-684 is displayed with a σ-cutoff of 1.5 rmsd. The view is similar as in Figure 2.

Supplememtary Figure 2

Differences in the observed electron density for loop-2. Residues 622-636 are shown in sticks and their corresponding electron density displayed with a σ-cutoff of 1.0 rmsd. Wild type, G678V, M680L and R653H are colored green, orange, orange and purple, respectively. The orientation of the B30.2 domain is as displayed in Figure 1.

Supplememtary Figure 3

Sequence alignment of the B30.2 domains of different human TRIM proteins. Secondary structure elements are assigned according to Weinert et al.[23]. Residues are shaded according the BLOSUM62 score between white and blue from no conservation to full conservation, respectively. The alignment in ordered according to the sequence similarity to pyrin. Highlighted in red boxes are the amino acids involved in hydrogen bonding between loop-2 and 5 in the pyrin B30.2 domain. Residues involved in hydrophobic interaction between the loops are marked in red. The R653 forms two hydrogen bonds to the S650, whereas H653 only bonds to the carbonyl oxygen of the serine residue. These residues are highlighted by a

grey box, also showing that a histidine at this position is conserved in most TRIM proteins.

Supplememtary Table 1
Data Collection Statistics.

Supplememtary Table 2
Refinement Statistics

Supplememtary Table 3
Hydrogen bonding network between loop-2 and loop-5.

References

1. Soriano, A. & Manna, R. Familial Mediterranean fever: new phenotypes. *Autoimmunity reviews* **12**, 31-7 (2012).
2. Ben-Chetrit, E. & Levy, M. Familial Mediterranean fever. *Lancet* **351**, 659-64 (1998).
3. A candidate gene for familial Mediterranean fever. *Nature genetics* **17**, 25-31 (1997).
4. Ancient missense mutations in a new member of the RoRet gene family are likely to cause familial Mediterranean fever. The International FMF Consortium. *Cell* **90**, 797-807 (1997).
5. Milhavet, F. et al. The infevers autoinflammatory mutation online registry: update with new genes and functions. *Human mutation* **29**, 803-8 (2008).
6. Akar, N. et al. MEFV mutations in Turkish patients suffering from Familial Mediterranean Fever. *Human mutation* **15**, 118-9 (2000).
7. Ayesh, S.K., Nassar, S.M., Al-Sharef, W.A., Abu-Libdeh, B.Y. & Darwish, H.M. Genetic screening of familial Mediterranean fever mutations in the Palestinian population. *Saudi medical journal* **26**, 732-7 (2005).
8. Albayrak, F., Selcuk, N.Y., Odabas, A.R., Cetinkaya, R. & Pirim, I. Genotype-phenotype correlation in patients with familial Mediterranean fever in East Anatolia (Turkey). *Genetic testing and molecular biomarkers* **14**, 325-8 (2010).
9. el-Garf, A., Salah, S., Iskander, I., Salah, H. & Amin, S.N. MEFV mutations in Egyptian patients suffering from familial Mediterranean fever: analysis of 12 gene mutations. *Rheumatology international* **30**, 1293-8 (2010).
10. El Gezery, D.A., Abou-Zeid, A.A., Hashad, D.I. & El-Sayegh, H.K. MEFV gene mutations in Egyptian patients with familial Mediterranean fever. *Genetic testing and molecular biomarkers* **14**, 263-8 (2010).
11. Dundar, M. et al. A molecular analysis of familial Mediterranean fever disease in a cohort of Turkish patients. *Annals of Saudi medicine* **32**, 343-8 (2012).
12. Chaabouni, H.B. et al. MEFV mutations in Tunisian patients suffering from familial Mediterranean fever. *Seminars in arthritis and rheumatism* **36**, 397-401 (2007).
13. Kawai, T. & Akira, S. Regulation of innate immune signalling pathways by the tripartite motif (TRIM) family proteins. *EMBO molecular medicine* **3**, 513-27 (2011).
14. Short, K.M. & Cox, T.C. Subclassification of the RBCC/TRIM superfamily reveals a novel motif necessary for microtubule binding. *The Journal of biological chemistry* **281**, 8970-80 (2006).
15. Latz, E., Xiao, T.S. & Stutz, A. Activation and regulation of the inflammasomes. *Nature reviews. Immunology* **13**, 397-411 (2013).
16. Dinarello, C.A. Immunological and inflammatory functions of the interleukin-1 family. *Annual review of immunology* **27**, 519-50 (2009).
17. Papin, S. et al. The SPRY domain of Pyrin, mutated in familial Mediterranean fever patients, interacts with inflammasome components and inhibits proIL-1beta processing. *Cell death and differentiation* **14**, 1457-66 (2007).
18. Yu, J.W. et al. Pyrin activates the ASC pyroptosome in response to engagement by autoinflammatory PSTPIP1 mutants. *Molecular cell* **28**, 214-27 (2007).
19. Gavrilin, M.A. et al. Pyrin critical to macrophage IL-1beta response to Francisella challenge. *Journal of immunology* **182**, 7982-9 (2009).
20. Gavrilin, M.A. et al. Activation of the pyrin inflammasome by intracellular Burkholderia cenocepacia. *Journal of immunology* **188**, 3469-77 (2012).
21. Yu, J.W., Farias, A., Hwang, I., Fernandes-Alnemri, T. & Alnemri, E.S. Ribotoxic Stress through p38 Mitogen-activated Protein Kinase Activates in Vitro the Human Pyrin Inflammasome. *The Journal of biological chemistry* **288**, 11378-83 (2013).

22. Wang, D. et al. Inflammation in mice ectopically expressing human Pyogenic Arthritis, Pyoderma Gangrenosum, and Acne (PAPA) Syndrome-associated PSTPIP1 A230T mutant proteins. *The Journal of biological chemistry* **288**, 4594-601 (2013).
23. Weinert, C., Grutter, C., Roschitzki-Voser, H., Mittl, P.R. & Grutter, M.G. The crystal structure of human pyrin b30.2 domain: implications for mutations associated with familial Mediterranean fever. *Journal of molecular biology* **394**, 226-36 (2009).
24. Grutter, C. et al. Structure of the PRYSPRY-domain: implications for autoinflammatory diseases. *FEBS letters* **580**, 99-106 (2006).
25. James, L.C., Keeble, A.H., Khan, Z., Rhodes, D.A. & Trowsdale, J. Structural basis for PRYSPRY-mediated tripartite motif (TRIM) protein function. *Proceedings of the National Academy of Sciences of the United States of America* **104**, 6200-5 (2007).
26. Biris, N. et al. Structure of the rhesus monkey TRIM5alpha PRYSPRY domain, the HIV capsid recognition module. *Proceedings of the National Academy of Sciences of the United States of America* **109**, 13278-83 (2012).
27. Park, E.Y. et al. Crystal structure of PRY-SPRY domain of human TRIM72. *Proteins* **78**, 790-5 (2010).
28. Ait-Idir, D., Khilan, A., Djerdjouri, B. & El-Shanti, H. Spectrum of mutations and carrier frequency of familial Mediterranean fever gene in the Algerian population. *Rheumatology* **50**, 2306-10 (2011).
29. Goulielmos, G.N. et al. Mutational analysis of the PRYSPRY domain of pyrin and implications for familial mediterranean fever (FMF). *Biochemical and biophysical research communications* **345**, 1326-32 (2006).
30. Akpolat, T., Ozkaya, O. & Ozen, S. Homozygous M694V as a risk factor for amyloidosis in Turkish FMF patients. *Gene* **492**, 285-9 (2012).
31. Kabsch, W. Xds. *Acta crystallographica. Section D, Biological crystallography* **66**, 125-32 (2010).
32. McCoy, A.J. et al. Phaser crystallographic software. *Journal of applied crystallography* **40**, 658-674 (2007).
33. Adams, P.D. et al. PHENIX: a comprehensive Python-based system for macromolecular structure solution. *Acta crystallographica. Section D, Biological crystallography* **66**, 213-21 (2010).
34. Murshudov, G.N. et al. REFMAC5 for the refinement of macromolecular crystal structures. *Acta crystallographica. Section D, Biological crystallography* **67**, 355-67 (2011).
35. Emsley, P., Lohkamp, B., Scott, W.G. & Cowtan, K. Features and development of Coot. *Acta crystallographica. Section D, Biological crystallography* **66**, 486-501 (2010).
36. Baker, N.A., Sept, D., Joseph, S., Holst, M.J. & McCammon, J.A. Electrostatics of nanosystems: application to microtubules and the ribosome. *Proceedings of the National Academy of Sciences of the United States of America* **98**, 10037-41 (2001).
37. Dolinsky, T.J., Nielsen, J.E., McCammon, J.A. & Baker, N.A. PDB2PQR: an automated pipeline for the setup of Poisson-Boltzmann electrostatics calculations. *Nucleic acids research* **32**, W665-7 (2004).
38. Keller, O., Kollmar, M., Stanke, M. & Waack, S. A novel hybrid gene prediction method employing protein multiple sequence alignments. *Bioinformatics* **27**, 757-63 (2011).
39. Waterhouse, A.M., Procter, J.B., Martin, D.M., Clamp, M. & Barton, G.J. Jalview Version 2--a multiple sequence alignment editor and analysis workbench. *Bioinformatics* **25**, 1189-91 (2009).
40. Perron, M.J. et al. TRIM5alpha mediates the postentry block to N-tropic murine leukemia viruses in human cells. *Proceedings of the National Academy of Sciences of the United States of America* **101**, 11827-32 (2004).

41. Perfetto, L. et al. Exploring the diversity of SPRY/B30.2-mediated interactions. *Trends in biochemical sciences* **38**, 38-46 (2013).
42. Keeble, A.H., Khan, Z., Forster, A. & James, L.C. TRIM21 is an IgG receptor that is structurally, thermodynamically, and kinetically conserved. *Proceedings of the National Academy of Sciences of the United States of America* **105**, 6045-50 (2008).
43. Schaner, P. et al. Episodic evolution of pyrin in primates: human mutations recapitulate ancestral amino acid states. *Nature genetics* **27**, 318-21 (2001).
44. Woo, J.S., Suh, H.Y., Park, S.Y. & Oh, B.H. Structural basis for protein recognition by B30.2/SPRY domains. *Molecular cell* **24**, 967-76 (2006).
45. Chae, J.J. et al. The B30.2 domain of pyrin, the familial Mediterranean fever protein, interacts directly with caspase-1 to modulate IL-1beta production. *Proceedings of the National Academy of Sciences of the United States of America* **103**, 9982-7 (2006).

Figures

Figure 1

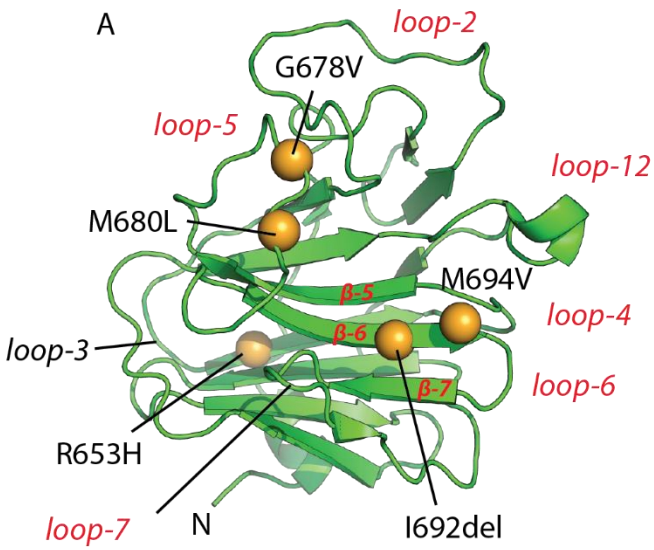

Figure 2

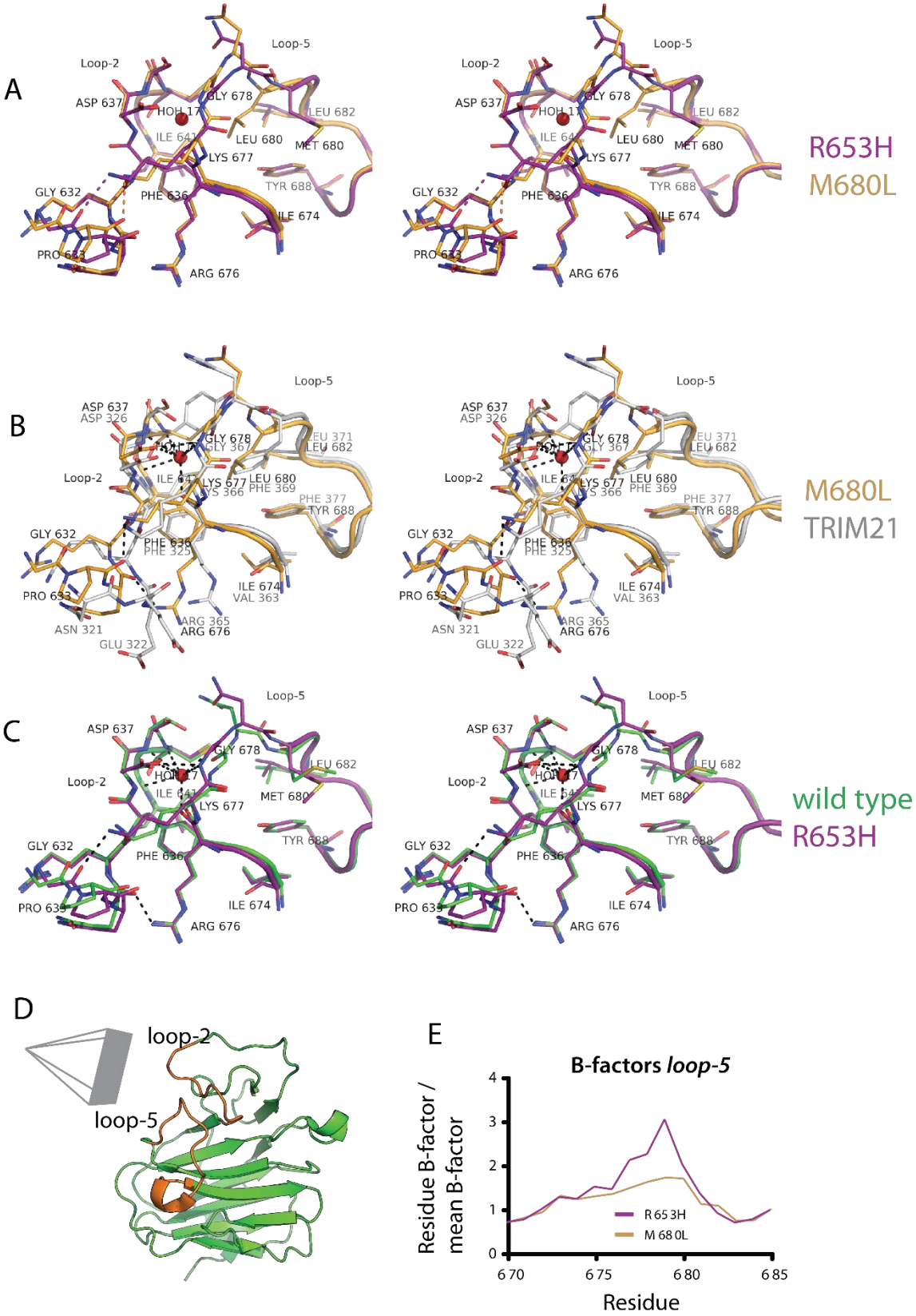
A
Loop-5
Loop-2
ASP 637
GLY 678
LEU 682
ILE 641
LEU 680
MET 680
LYS 677
GLY 632
PHE 636
TYR 688
ILE 674
PRO 633
ARG 676
R653H
M680L
B
ASP 637
ASP 326
LEU 371
GLY 367
LYS 366
PHE 369
PHE 377
PHE 325
VAL 363
ARG 365
ASN 321
GLU 322
M680L
TRIM21
C
wild type
R653H
D
loop-2
loop-5
E
B-factors loop-5
Residue B-factor / mean B-factor
R653H
M680L
Residue

Figure 3

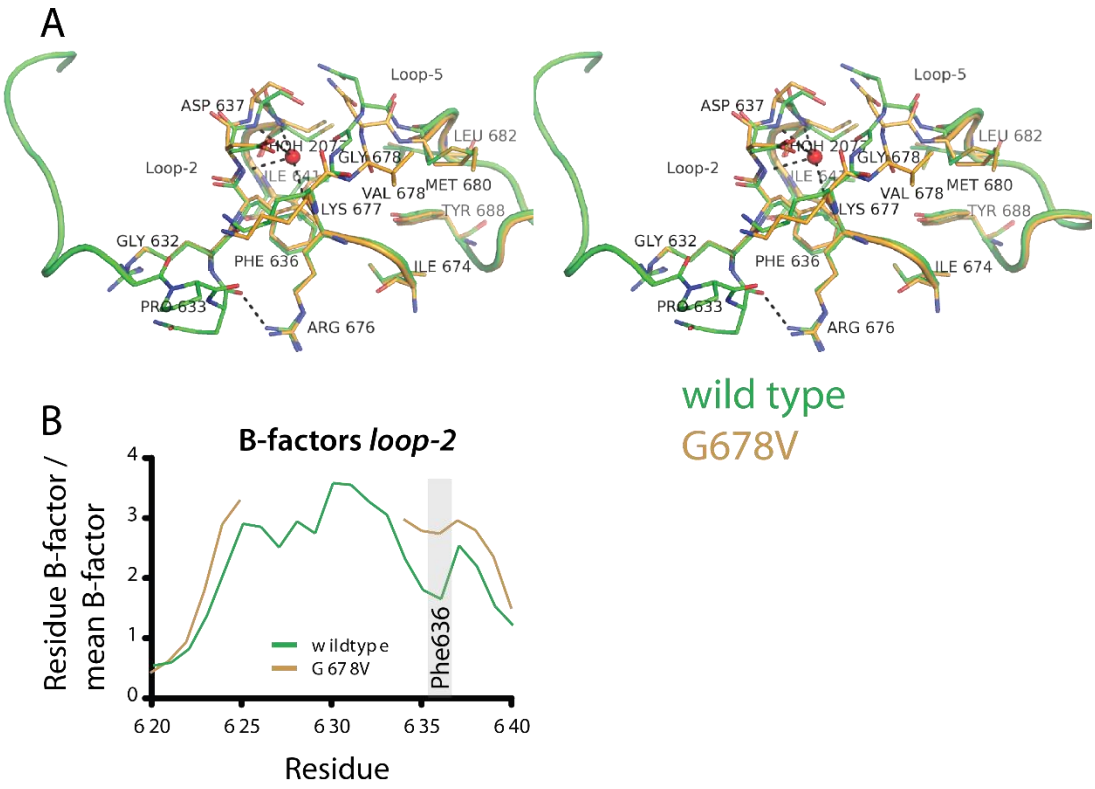
A
Loop-5
ASP 637
LEU 682
Loop-2
GLY 678
MET 680
VAL 678
LYS 677
TYR 688
GLY 632
PHE 636
ILE 674
ARG 676
wild type
G678V
B
B-factors loop-2
Residue B-factor / mean B-factor
wildtype
G678V
Phe636
Residue

Figure 4

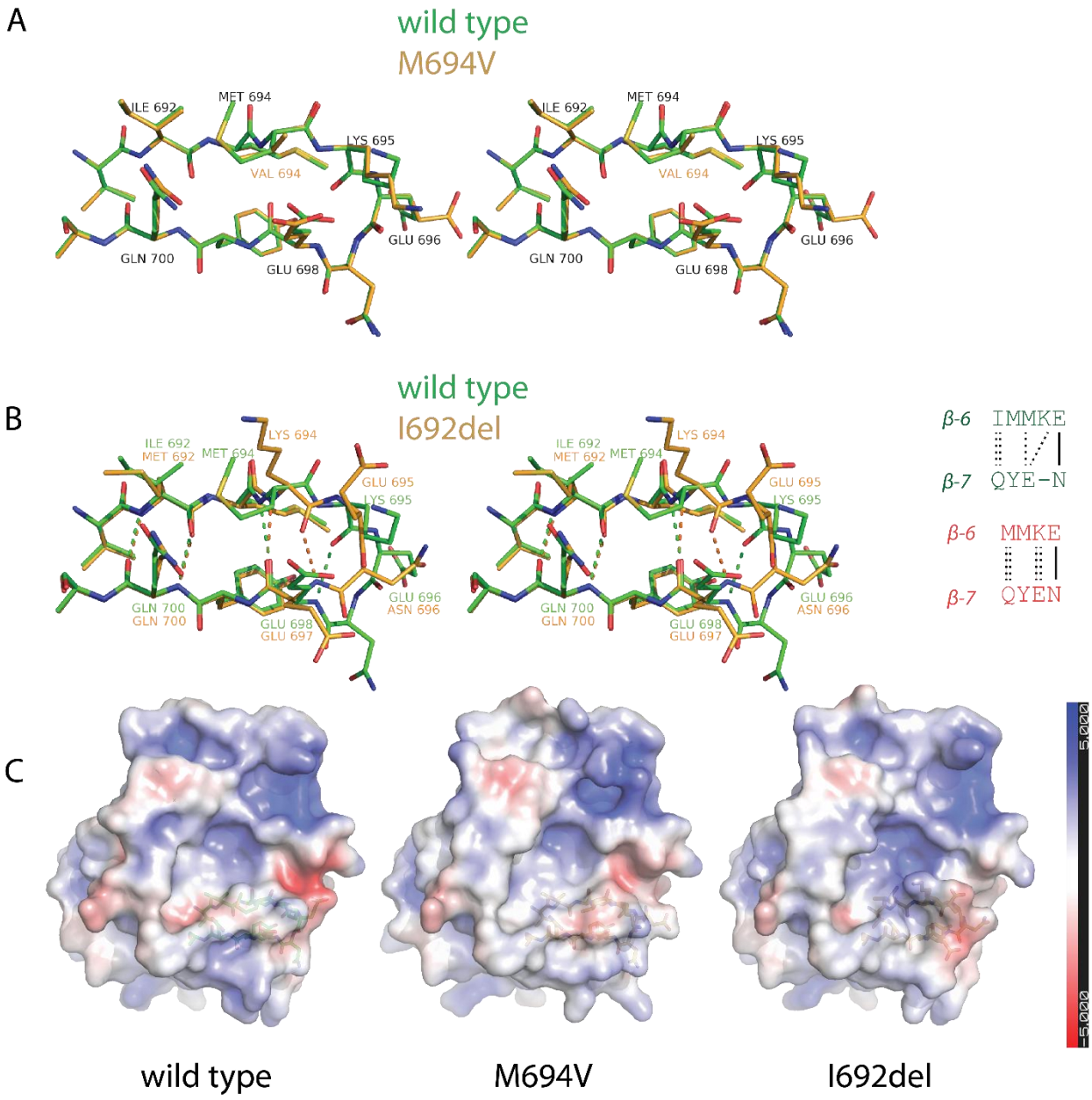
A
wild type
M694V
ILE 692
MET 694
LYS 695
VAL 694
GLU 696
GLN 700
GLU 698
B
wild type
I692del
ILE 692
MET 692
MET 694
LYS 694
GLU 695
LYS 695
GLN 700
GLN 700
GLU 698
GLU 697
GLU 696
ASN 696
β-6 IMMKE
β-7 QYE-N
β-6 MMKE
β-7 QYEN
C
5.000
-5.000
wild type
M694V
I692del

Figure 5

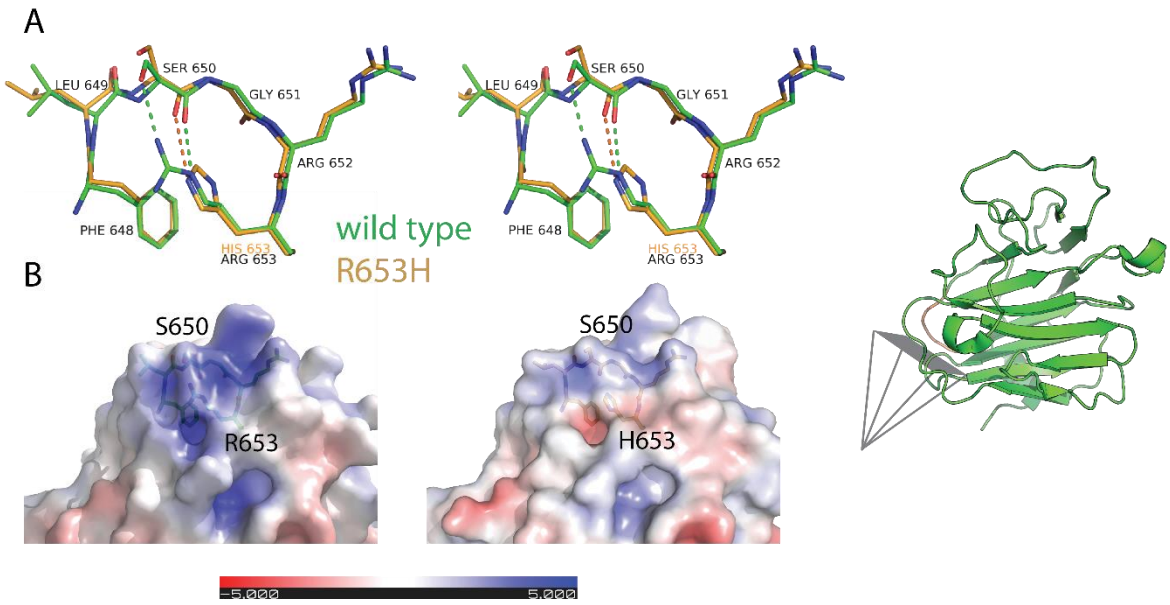
A
LEU 649
SER 650
GLY 651
ARG 652
PHE 648
HIS 653
ARG 653
wild type
R653H
B
S650
R653
S650
H653
−5.000
5.000

Supplementary Figure 1

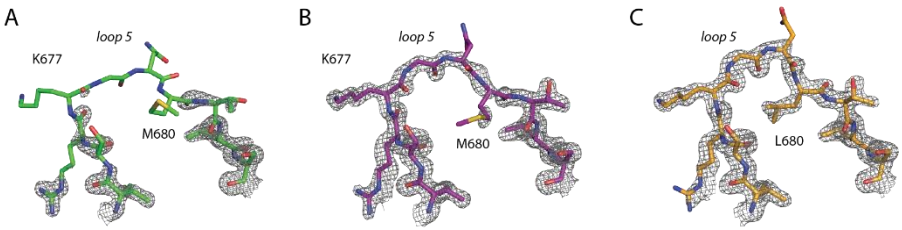

2wl1 ($P6_522$) R653H ($P2_12_12_1$) M680L ($P2_12_12_1$)

Supplementary Figure 2

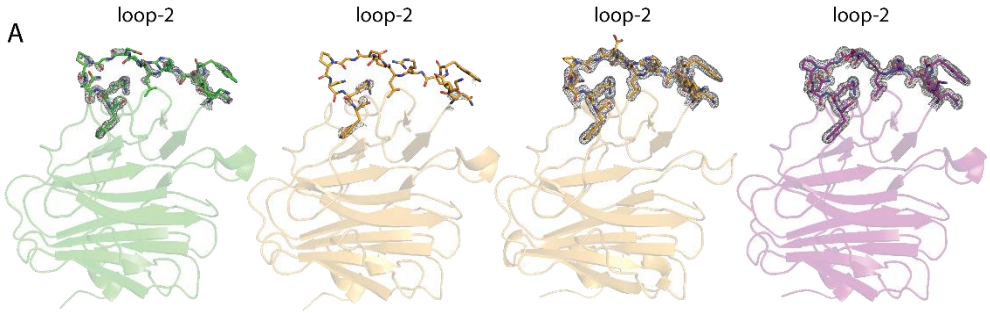

wild type ($P6_522$) G678V ($P6_522$) M680L ($P2_12_12_1$) R653H ($P2_12_12_1$)

Supplementary Figure 3

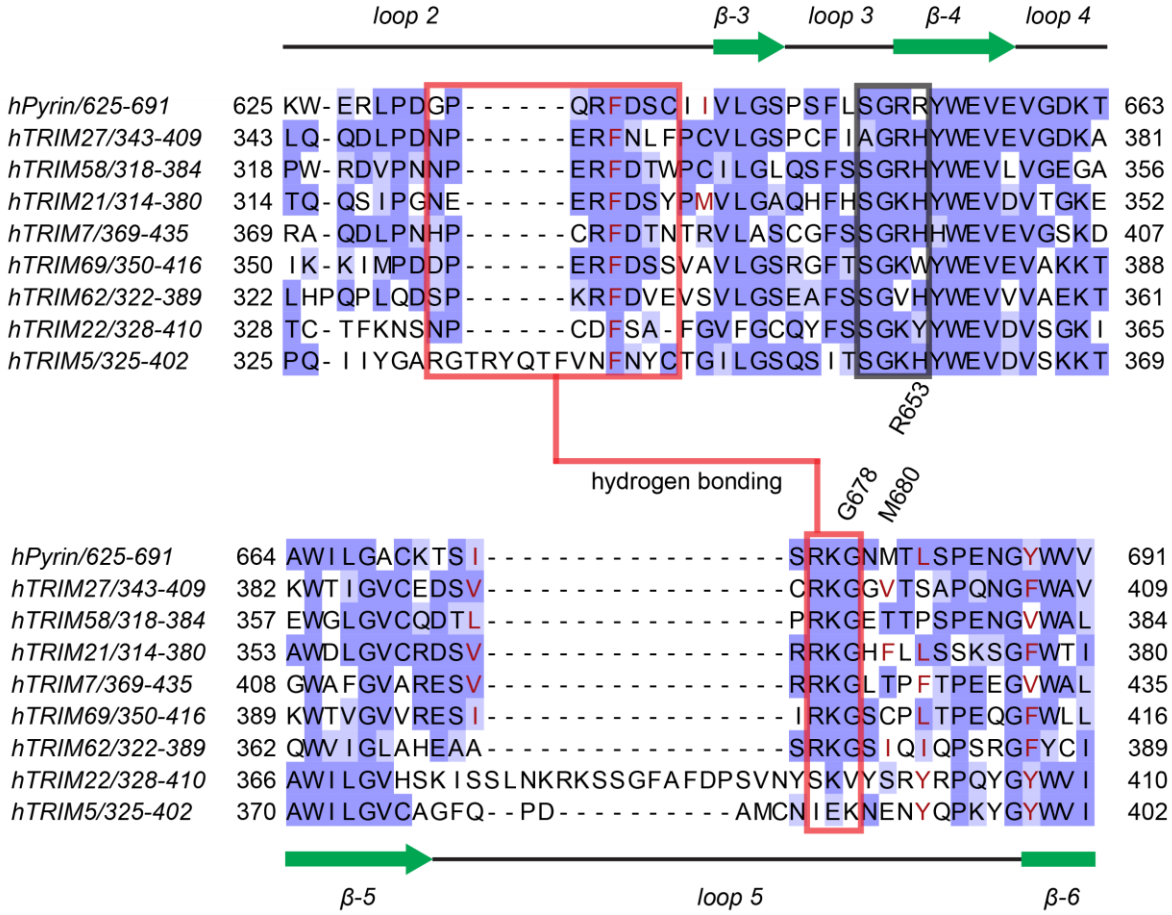

Supplementary Table 1

Data Statistics	R653H	G678V	M680L	I692del	M694V
Wavelength (Å)	1.0000	0.9793	1.0000	1.0000	0.9999
Resolution (Å)[a]	38.49 - 1.5 (1.554 - 1.5)	39.69 - 2.4 (2.486 - 2.4)	49.12 - 1.6 (1.657 - 1.6)	39.31 - 1.7 (1.761 - 1.7)	31 - 1.7 (1.761 - 1.7)
Space group	P 2_1 2_1 2_1	P 6_5 2 2	P 2_1 2_1 2_1	P 6_5 2 2	P 6_5 2 2
Unit cell (a,b,c,α,β,γ) [Å,°]	43.27 60.85 84.31 90 90 90	60.34 60.34 183.08 90 90 120	42.56 60.44 84.29 90 90 90	59.98 59.98 180.39 90 90 120	60.20 60.20 186.02 90 90 120
Total reflections[a]	452578 (46756)	69414 (6962)	315088 (14728)	489787 (45654)	302930 (11116)
Unique reflections[a]	36361 (3596)	7925 (779)	28808 (2573)	22086 (2167)	22819 (2126)
Multiplicity[a]	12.4 (13.0)	8.8 (8.9)	10.9 (5.7)	22.2 (21.1)	13.3 (5.2)
Completeness[a]	99.90 (100.00)	94.76 (96.77)	98.03 (89.84)	99.99 (100.00)	99.53 (95.46)
Mean I/sigma(I)[a]	22.23 (5.73)	10.87 (5.67)	17.43 (1.44)	24.08 (5.22)	22.71 (1.35)
Wilson B-factor	13.45	17.28	18.96	19.41	20.21
R-merge[a,b]	0.08086 (0.5179)	0.1695 (0.438)	0.0892 (1.058)	0.09948 (0.7156)	0.07997 (1.13)

a) Values for the highest resolution shell are given in parentheses.

b) $R_{merge}=\sum_{hkl}\sum_j|I_{hkl,j}-(I_{hkl})/\sum_{hkl}\sum_j I_{hkl,j}$, where Ihkl,j is the j^{th} observation for the reflection hkl and (I_{hkl}) is the mean intensity of the reflection hkl.

Supplementary Table 2

Refinement Statistics	R653H	G678V	M680L	I692del	M694V
Rwork[a] (%)	15.80 (17.72)	17.45 (18.60)	17.50 (27.53)	17.64 (20.75)	18.80 (27.52)
Rfree[a,b] (%)	17.29 (19.62)	22.13 (24.66)	20.20 (30.94)	21.26 (25.72)	22.65 (30.97)
Protein residues	194	191	195	190	191
Water	176	143	126	126	166
Heteroatoms	8	17	15	10	7
Deviation from ideal geometry					
RMS(bonds)	0.018	0.007	0.016	0.019	0.012
RMS(angles)	1.69	1.17	1.66	2.02	1.51
Ramachandran plot					
favored (%)	98	96	98	98	96
outliers (%)	0	0	0	0	0
Average B-factor (Å^2)					
Protein	16.5	26.9	22.2	29	25.3
Water	26.8	24.6	31.1	33.9	31.3
Heteroatoms	34.8	23.2	32.1	28.3	27.1
Deviation from wild type					
RMSD to 2wl1 (Å)	0.316	0.166	0.289	0.482	0.163

a) Values for the highest resolution shell are given in parentheses.
b) 5 % of the total reflections were used for the calculation of Rfree and were not used for refinement.

Supplementary Table 3

Structure	R653H	M680L	wildtype	G678V	TRIM 21
Space group	$P2_12_12_1$	$P2_12_12_1$	$P6_522$	$P6_522$	-
***Loop5* residue**	***loop-2* residues**				
Arg676 O	Asp637 N 3.5 Å; H_2O 17 2.84 Å	Asp637 N 3.52 Å H_2O 17 2.76 Å	H_2O 2077 defined at σ= 1.2rmsd 2.78 Å	-	Asp43 N 3.25 Å H_2O 2008 3.20 Å
Arg676 NH1	Gln634 O 2.5 Å	Gln634 O 2.5 Å	Gln634 O 2.80 Å	-	Gln40 O 2.77 Å
Lys677 NZ1	Gly632 O 2.95 Å; Arg635 O 2.78 Å	Pro633 O 2.93 Å; Arg635 O 2.78 Å	Lys677 NZ defined at σ= 1.2rmsd; Arg635 O 2.74 Å	Lys677 NZ defined at σ=0.9 rmsd; Arg635 O 2.80 Å	Asn38 O 3.4 Å; Arg41 O 2.88 Å
Gly678 N	Asp637 OD1 2.88 Å	Asp 637 OD1 2.93 Å	-	-	Asp43 OD1 2.73 Å
Gly678 O	H_2O 17 2.86 Å	H_2O 17 3.00 Å	-	-	H_2O 2008 3.13 Å
coordinated H2O	Asp637 N 3.25 Å; Ser638 N 2.97 Å; Cys639 N 3.27 Å	Asp637 N 3.29 Å; Ser638 N 2.97 Å; Cys639 N 3.16 Å	H_2O 2077 defined at σ= 1.2rmsd; Asp637 N 3.12 Å; Ser638 N 2.85 Å; Cys639 N 2.92 Å	no coordinated water	Asp43 N 3.51 Å; Ser44 N 2.75 Å;

4 Manuscript: Overall architecture and mode of dimerization of TRIM proteins revealed by the TRIM20 structure

4.1 Main Article

Title

Overall architecture and mode of dimerization of TRIM proteins revealed by the TRIM20 structure

Authors

Christopher Weinert[1], Damien Morger[1], Aleksandra Djekic[1], Peer R E Mittl[1] and Markus G Grütter[1,2]

Affiliations

[1] Department of Biochemistry, University of Zurich, Winterthurerstrasse 190, CH-8057 Zürich, Switzerland

[2] to whom correspondence should be addressed: gruetter@bioc.uzh.ch, Tel. +41-44-6355580, Fax. +41-44-6356834

Keywords

Coiled coil, pro-IL-1β, pyrin, TRIM, TRIM20

Abstract

Tripartite motif-containing (TRIM) proteins comprise a RING finger, a B-Box, a predicted coiled coil here termed central helical scaffold (CHS) domain and in most cases a C-terminal B30.2 domain. So far the overall architecture of TRIM proteins is unknown since only structures of individual domains are available. Here we present the 2.4 Å crystal structure of a functional portion of TRIM20 consisting of the CHS and B30.2 domains. In contrast to the previously assumed parallel arrangement, two CHS domains arrange in antiparallel manner thereby forming elongated dimers with centrally positioned B30.2 domains and B-Boxes placed distal 170 Å apart. Interdimeric contacts between B30.2 and CHS domains construct a yet unknown TRIM tetramer and unveil the mechanism of higher order self assembly. Together with the full length model, our data provides unprecedented insights into the structural and functional modularity of these proteins.

Significance statement

TRIM proteins are involved in various processes that include regulation of the innate immune response. Despite their functional diversity they share a common domain architecture. A striking feature is their ability to form higher order self-assemblies that in case of TRIM5 creates a hexagonal lattice. However, due to the lack of high resolution structures, the connectivity of the domains as well as a precise model of higher order assemblies remained unknown. We present the first crystal structure of a functional TRIM20 C-terminal fragment that reveals the antiparallel mode of dimerization as well as how two dimers form a tetramer. The presented structure not only allows modeling a full length TRIM protein, but also a precise model of a TRIM lattice.

Introduction

Tripartite motif-containing (TRIM) proteins represent a large family of proteins comprising approximately 100 human members, linked to diverse cellular functions including regulation of the innate immune system, retroviral restriction, cell proliferation and differentiation (1, 2). They share a conserved domain architecture consisting of an N-terminal RING domain, one or two B-Box domains followed by a predicted coiled coil motif here called central helical scaffold (CHS) domain (3). The RING and B-Box domains are zinc fingers that confer E3-ligase activity and protein-protein interactions to form higher order oligomers (HO), respectively (2, 4-6). The B-Box is followed by the CHS domain, which is responsible for low order oligomerization (3). C-terminal of the CHS domain about half of the TRIMs contain a B30.2 domain that mediates ligand binding (7-9).

TRIM20, also named pyrin, has an N-terminal pyrin domain (PYD) and a linker region of unknown structure, preceding a degenerated RING sequence (10). The PYD belongs to the death domain superfamily enabling homotypic interactions with other PYD containing proteins (11, 12). TRIM20 is involved in the modulation of the pro-inflammatory cytokine pro-Interleukin-1β (pro-IL-1β) and is associated to the auto-inflammatory disease Familial Mediterranean Fever (FMF) (13, 14). Through a direct interaction to pro-IL-1β, TRIM20 is considered to inhibit the inflammasome mediated maturation of the cytokine (15). However, TRIM20 can also potently induce the maturation of pro-IL-1β (6, 16-18). The exact mechanism of regulation between these two contrary functions is not known.

Several structures of isolated RING, B-Box and C-terminal domains of TRIM proteins are known to date (5, 19, 20). With respect to the TRIM tripartite motif (RING, B-Box and CHS domain), the CHS is the only domain where no structural information exists so far. This domain is of particular interest as it defines the spatial arrangement of the adjacent domains and thus the overall architecture of TRIM proteins.

Within the CHS sequence a coiled coil (CC) motif and an L2 linker to the B30.2 domain is predicted (21). The CC motif is prognosticated within the first 100-120 amino acids C-terminal of the B-Box and the adjacent L2 linker is between 50 to 70 amino acids in length (22). For the retroviral restriction factor TRIM5α and the intracellular Fc-receptor TRIM21, the CHS domain is responsible for dimerization (23-25). This formation of low order oligomers is essential for function as in both TRIM20 and TRIM5α a deletion of the CHS results in a monomeric and inactive protein (6, 26). However, dimerization does not seem to be the only function of the CHS. In addition, residues have been identified in the CHS domain of TRIM5α that do not interfere with dimerization, but lead to a loss of restriction (27).

Here we present the crystal structure of a functional part of TRIM proteins, the TRIM20 CHS-B30.2 C-terminal portion, providing insight into the overall structure

of TRIM proteins. Using small angle X-ray scattering (SAXS) we revealed the flexibility between the CHS and the B30.2 domains mediated by a short hinge. In addition, we characterized the binding of the CHS-B30.2 fragment to pro-IL-1β *in vitro*.

Results

Crystal Structure of TRIM20Δ413. To investigate the mode of oligomerization and the relative arrangement of the B30.2 domain in TRIM proteins we designed a construct that comprises the CHS and the B30.2 domains. Secondary structure prediction for TRIM20 suggests that the bipartite CC motif of the CHS starts shortly after the B-Box domain (Fig. S1). We therefore engineered a construct that starts with the conserved glutamate 414 yielding a fragment called TRIM20Δ413 (Fig. 1*A*). Analytical ultracentrifugation at 4 °C shows that this C-terminal fragment is a dimer in solution (Fig. 1*B*).

TRIM20Δ413 crystallized in space group $P2_1$ with 3 dimers in the asymmetric unit (Table S1 and Fig. S2*A*). The protein has an elongated structure formed by the CHS dimer (E414-N586) that is connected to the globular B30.2 domains (E589-G776) through a short hinge region (Fig. 2*A*).

The monomeric CHS domain folds into 4 helices (α1-α4). The first α-helix that harbors the predicted CC motif consists of 106 residues (E414-E520) and spans a length of approximately 155 Å (Fig. 2*A*). The designated L2 linker consists of two short helices α2 and α3 (E524-T539) followed by an 11 amino acid extended stretch and helix α4 (N551-Q586). A short linker of 2 amino acids (V587 and P588) connects the C-terminus of α4 to the B30.2 domain. The extended stretch and α4 are oriented antiparallel to the helix α1 whereas helix α2 and α3 are in the peripheral turn forming a hairpin.

The two protomers arrange in an antiparallel fashion along helix α1 with a shared interface of over 4700 $Å^2$ that is created by all four helices including the extended stretch. As a result, the adjacent domains are distinctly placed where the N-termini of both monomers and consequently also the B-Box domains are positioned 167 Å apart from each other, while the B30.2 domains are in proximity close to the central 2-fold axis of the dimer.

The predicted two CC regions localize on the N- and C-terminal part of helix α1 that due to the antiparallel dimerization structurally align and form a 2-helical coiled coil (2-CC; Fig. 2*B*). In case of TRIM20, residues L427 and L430 coil with residues L513’ and L516’ (the prime indicates residues from the other protomer). Additionally, an antiparallel 3-helical coiled coil is formed between residues in α1, α4, and α1’ (L484, V487, and V491; L560, and I557, I553; L458’, T455’ and F451’, Fig. 2B). Whereas the residues involved in the 2-CC are highly conserved in TRIM proteins, the 3-CC seems to be TRIM20 specific as these residues show no

sequence conservation (Fig. S1). Nevertheless, compared to the length of helix α-1 and the size of the entire CHS domain, the CC character of the fold, i.e. the supercoiling of the helices, is small. In addition, the predicted CC motif and the designated L2 linker form one helical domain that is centrally located in TRIM proteins and provides the molecular scaffold for the placement of the adjacent domains (Fig. 2*A* and *C*). Therefore, we suggest the term CHS domain.

In the central core around the 2-fold axis, helices α1 and α4 of both subunits form an antiparallel four helix bundle. This bundle is slightly bent, which leads to a curvature of the entire CHS domain, reminiscent of a coat hanger. Due to the crystal packing, the overall curvature found in the three dimers of the asymmetric unit varies (Fig. S2*B*). The changes in the curvature appear in the bundle while the rest remains identical suggesting the bundle of the CHS domain to be a flexible structural element.

The B30.2 domain is only connected through a short linker point upwards along the 2-fold axis of the dimer, just like the hook on a coat hanger. As a consequence the CHS and the B30.2 domains do not share any interaction surface within the dimer structure. There is some degree of flexibility in the linker since the B30.2 domain orientation relative to the CHS domain is different in the six monomers in the crystal (Fig. S2*C*). This flexibility is more pronounced in solution and demonstrated by the SAXS measurements (see below).

An interesting feature of the X-ray structure is the contact between two neighboring dimers in the crystal that form a tetramer. This contact is created by the B30.2 domains of one dimer (orange and purple), which interact with the extended stretch between α3 and α4 of the CHS domain of the other dimer (blue and green respectively) (Fig. 3*A*). An additional tetramer interface exists between the N-terminal helices of the involved B30.2 domains (Fig. 3*A*). In total, the interaction surface amounts on average to 1830 $Å^2$ which represents an unusually large crystal contact and can be interpreted to be a surface area of biological relevance (Fig. 3*B*). In support of this notion are *in-vivo* co-immunoprecipitation experiments by Papin et al. (15) which have shown that the isolated B30.2 domain interacts with an isolated B-Box-CHS construct. Further evidence comes from a construct TRIM20Δ303 (see also below) for which we see the formation of a tetramer in solution as indicated by size exclusion chromatography (Fig. S6*D*).

We prepared a CHS-B30.2 domain construct for the homologue TRIM5α and performed SAXS measurements of two oligomeric species separated by SEC. These experiments reveal the presence of a dimer and a tetramer (Fig. S3*A*). The experimental radius of gyration (R_G) of 4.5 and 5.3 nm for the dimer and the tetramer, respectively, match closely the calculated values using the TRIM20Δ413 crystal structure (4.3 nm and 5.4 nm for the dimer and tetramer, respectively). The same is true for the determined maximal diameter (Fig. S3*B-D*).

Solution structure of TRIM20Δ413. SAXS measurements of the TRIM20Δ413 reveal an increasing radius of gyration (R_G) in a concentration dependent manner (Fig. S4*A* and *B*, Table S2) indicative for the presence of HO's in solution, with the tetramer being a likely intermediate. The R_G for an infinitely diluted sample is 4.27 nm, which is in perfect agreement with the calculated R_G for the structure of the dimer (4.29 nm; Fig. S4*C*). The crystal structure however does not fit well to the experimental data (χ^2=3.62) in the middle resolution scattering range s (nm^{-1})=0.8-1.8 (Fig. 4*A* and *B*). Since the Kratky plot reveals an interdomain flexibility (Fig. S4*D*), we generated a rigid body model by introducing flexibility between the CHS and the B30.2 domains, which significantly improves the fit to the experimentally determined scattering profile (χ^2=2.01). In this derived model, one of the two B30.2 domains is arranged as in the crystal structure whereas the second B30.2 domain is rotated perpendicular to the dimeric 2-fold axis placing it sideways the CHS domain (Fig. 4*A* and *C*; Fig. S4*F*). A flexibility of the CHS domain, as it is suggested by the differences in curvature of the three dimers in the crystal structure, was not modeled. Nevertheless, conformational flexibility of the CHS domain is also suggested from SAXS data as the average diameter found in solution is around 160 Å, which is a little less than in the crystal structure (173 Å).

Binding to pro-IL-1β. To elucidate the TRIM20Δ413 functionality, we investigated the reported binding to pro-IL-1β (15). Co-immunoprecipitation experiments revealed a direct interaction *in-vitro* between the purified proteins. The interaction required the presence of both the CHS and B30.2 domain as the individual domains could not be precipitated with pro-IL-1β (Fig. 5*A*). Surface Plasmon Resonance (SPR) experiments between TRIM20Δ413 and pro-IL-1β revealed a heterogeneous ligand behavior of TRIM20, suggesting that it is present in two states with measured affinities of 0.70 µM and 13.7 µM (Table S3 and Fig. S5*A*). A complex formation of the TRIM20Δ413 and pro-IL-1β in solution was detected by size exclusion chromatography (SEC). Stable complex formation however was only observed after incubating the proteins at room temperature (rt) whereas no complex was observed after incubation at 4 °C (Fig. 5*B* and Fig. S5*B*). The complex shows a large peak shift towards lower retention volumes corresponding to a molecular weight of approximately 400 kDa. This suggests a complex of more than one TRIM20Δ413 dimer (85.5 kDa) binding two pro-IL-1β (31.9 kDa) molecules but rather a higher oligomeric species. The complex is in equilibrium with its individual components which can be shown by reinjecting the isolated complex (Fig.S4*C*). Incubation of TRIM20Δ413 or pro-IL-1β alone does not show signs of higher oligomerization upon incubation at room temperature (Fig. 5*C*). The formation of an apparent higher oligomeric complex in solution could explain the heterogeneous ligand behavior of TRIM20 in the SPR experiments, where presumably the dimer binds with a low affinity, and oligomers of the dimer (e.g. tetramer) have a significantly increased affinity to pro-IL-1β.

Stereotype TRIM model. Between the N-terminal PYD domain and the CHS domain, TRIM20 has a 318 amino acid region of mostly unknown structure, which makes a prediction of the TRIM20 full length structure impossible. However, the TRIM20Δ413 structure reveals around 75% of a TRIM full length molecule missing only the N-terminal RING and B-Box domains (Fig. 1*A*). A linkage between the B-Box and the CHS domain can be observed in the NMR structure of the TRIM29 B-Box domain as its C-terminal eight residues form an α-helix that aligns with α1 residues of the TRIM20 CHS domain (Fig. S6*A*) (29). As B-Box and RING domains share a common fold (30), a template for the connectivity between RING and B-Box domain is given by TRIM18 tandem B-Box (B-Box1/2) structure. It features an interaction surface between the two adjacent B-Box domains and based on the hypothesis that there is an equivalent RING/B-Box interface, this TRIM18 B-Box1/2 structure was used to generate a RING/B-Box model that was annealed to the CHS domain structure via the proposed domain linkage of TRIM29 (Fig. 6*A* and Fig. S6*B*). This model has a calculated R_G and diameter of 6.2 nm and 21.1 nm, respectively. We prepared a corresponding TRIM20 construct starting just N-terminal of the degenerated RING domain called TRIM20Δ303 which in SAXS provided a R_G and diameter of 6.2 nm and 20.7 nm, respectively (Fig. S6*D-I*). This matches the values obtained for the presented model.

Discussion

TRIM proteins share a common domain architecture, of which structures of isolated domains have been determined. Due to the lack of structural information on the relative spatial arrangement of the domains in a full length TRIM context, detailed molecular mechanisms for ligand binding, self-assembly and signal transduction remained elusive.

Here, the first high resolution structure of a TRIM CHS-B30.2 fragment at 2.4 Å resolution is presented. The predicted CC of the tripartite motif and the designated L2 linker to the B30.2 domain form one domain that we termed CHS domain. The elongated and helical CHS domain dimerizes over a large interface in an antiparallel fashion creating a coat hanger like structure and reveals the overall architecture of TRIM proteins. Furthermore, a crystal contact between two dimers provides a structural template for a B30.2 domain dependent formation of HOs.

The necessity for dimerization for correct function has been shown for several TRIM proteins. In TRIM20, a deletion of the CHS domain leads to a monomeric and inactive protein (6). The same is true for the TRIM20 homologue TRIM5α, for which extensive mutational studies of the CHS domain have revealed insights into the precise contribution of this domain to the protein's function. The fact that the CHS domain of TRIM20 can be functionally exchanged with the corresponding region of TRIM5α suggests a structural conservation and allows comparison (6). Rhesus TRIM5α that potently restricts HIV-1 by binding to the capsid surface of

the virion core, self-assembles into HOs (31). This oligomerization is dependent on the RING, B-Box as well as the CHS domain. Whereas dimerization is mediated by the CHS domain, the B-Box is thought to connect two dimers through a B-Box/B-Box interaction (4). However, several residues in the CHS domain of TRIM5α have been identified that are crucial for HO association and retroviral restriction activity regardless of dimerization (21, 27, 32). Based on these findings a CHS/CHS interaction was proposed to contribute to the self-assembly.

The CHS-B30.2 structure of TRIM20 provides a model to understand the structure function behavior of the CHS domain in TRIM proteins. The CHS domain not only acts as a scaffold for the surrounding domains but also as a mediator for dimerization and tetramerization.

As the B-Box directly precedes the α1 helix of the CHS domain without an appreciable linker, the peripheral edge of the CHS domain is a critical factor for the correct orientation of the B-Box, which is formed by the N-terminus of the α1 helix, the C-terminus of the α1' helix and by helices α2 and α3. Sequence comparison between several TRIM proteins shows that residues of these structural elements are conserved and mutations in the α2 helix of TRIM5α have been shown to interfere with the ability of the protein to self-assemble (Fig. S1; (32)). The TRIM20 structure suggests that this effect is due to alterations in the relative positioning of the B-Box relative to the CHS domain. From the modeled stereotype TRIM protein, even a direct interaction between the α2 helix and the B-Box domain can be imagined (Fig. 6*A*).

The 3-dimensional shape of a TRIM self-assembly has been shown by Ganser-Pornillos and colleagues (28). They have revealed that a TRIM21-TRIM5α chimera spontaneously forms hexagonal lattices with a length between 180 and 205 Å of each hexagonal side (Fig. 6*B*). Together with the modeled RING finger and B-Box domain the elongated CHS fold is roughly 210 Å in diameter. This reveals that the elongated fold of the CHS is providing the dimensions for a putative TRIM lattice and one could assume a single dimer to be sufficient to match the length of the hexagonal lattice. However, this leads to only 3 B-Box domains at each hexagon edge due to the antiparallel dimer arrangement. As the B-Box connects two dimers via a complementary surface, it introduces a two-fold symmetry (4). Therefore having only three B-Box domains connecting three dimers imposes a symmetry problem. Based on the suggested CHS/CHS interaction, Ganser-Pornillos and colleagues have proposed that each side of the hexagonal lattice is made of a tetramer, placing six B-Box domains at each hexagon edge (Fig. 6*C*). The structure determined here also implies the formation of tetramers, however with a different arrangement of its domains. Instead of the proposed CHS/CHS interaction that connects two neighboring dimers, the tetramer is formed by the CHS/B30.2 interaction (Fig. 3*B* and Fig. 6*D*). This suggests a new mechanism for TRIM lattice formation where all symmetry axis' arising from oligomerization are parallel to each

other and perpendicular to the created surface. As a consequence, all B30.2 domains are presented to the same side of the lattice, an essential feature missing in the previously suggested model. Our model is further supported by the ability of TRIM5αΔ132 to form tetramers and the fact that TRIM21-TRIM5α lattice formation was less efficient and less ordered, when the B30.2 domain was deleted (28). However, the general ability to form a lattice was retained. Remarkably, mutations of residues in TRIM5α that align with the extended stretch of the CHS domain cause a loss of restriction capability (27). Those TRIM5α mutants were stable dimers, but unable to form cytoplasmic bodies. As this stretch is distant from the outer conserved edge, one can assume that such mutations do not interfere with correct arrangement and connectivity to the B-Box and but rather lead to the inability to bind to the B30.2 domain of another dimer.

Our data on the TRIM20Δ413/pro-IL-1β interaction also supports the physiological relevance of higher oligomers in case of TRIM20 as the complex formed between the two proteins indicates an oligomerization of TRIM20Δ413 dimers. The existence of a TRIM20 tetramer is suggested by the longer TRIM20Δ303 SEC profile. Additionally, SPR experiments suggest two states for TRIM20 with different affinities to pro-IL-1β that could be explained by a dimer binding with low affinity (13.7 µM) and a higher oligomer binding more affine (0.7 µM). The binding of pro-IL-1β to TRIM20 is thought to inhibit the caspase-1 dependent maturation of the cytokine. This inhibition might be disrupted in case of FMF mutations (15). Interestingly, several FMF associated residues are located within the tetramer interface, these include I591, A595, L649 and R653 (33). Mutations could alter the affinity of dimers to assemble into tetramers, therefore preventing TRIM20 to effectively bind pro-IL-1β and inhibit its maturation. Mutational studies have to address the particular role of TRIM20 HO's and the involved tetramer interface in the binding to pro-IL-1β and the putative inhibition of is maturation.

As the designated L2 linker is fully structured and forms together with the CC motif the CHS domain, the flexible connection to the B30.2 domain is only mediated by a short hinge region that allows the B30.2 domain to adopt different orientations relative to the CHS domain. Together with the flexibility of the CHS domain, this feature adds to the structural and functional flexibility of TRIM proteins. For instance, various antibody coated surfaces, such as bacteria, non-coated viruses or latex beads are recognized by the intracellular Fc-receptor TRIM21 and induce downstream signaling (34). TRIM5α can adapt to different capsid curvatures and restricts various retroviruses. The presented structure reveals how TRIM proteins can adopt their modular structure to adapt to differently presented ligands.

When comparing different TRIM proteins in sequence N-terminal of the B30.2 domain, namely the extended stretch and helix α4, it is noteworthy that conservation in length and sequence identity is low (Fig. S1). For instance, TRIM27 has a similar length of the α4 helix as TRIM20, while TRIM5α, 21 and 22 are shorter

in sequence. This suggests that helix α4 and the extended stretch act as a ruler to specifically define the position the B30.2 domains, accommodating for ligand specificity of TRIM proteins.

Overall, the TRIM20Δ413 reveals the antiparallel dimerized and elongated structure of the CHS domain leading to distinct positioning of the adjacent domains, which are in case of the B30.2 domain flexibly connected. The structure fits very well to the functional data on TRIM5α with respect to the overall architecture and the domain contributions for lattice formation. The ability of TRIM5α to form tetramers strengthens the hypothesis, that the presented TRIM20 tetramer structure resembles a building block for lattice formation. The quantitative results of the interaction between TRIM20 and pro-IL-1β set the basis for the analysis of FMF associated mutations and their effect towards pro-IL-1β binding and putative inhibition of the cytokine's activation.

Experimental Procedure

Cloning, expression and purification, SAXS experiments, Co-IP experiment, surface Plasmon resonance analysis, size exclusion experiments and model building are described in the *SI Methods.*

Crystallisation and structure determination

First crystals were found in 0.1 M Tris-AcOH, pH 8-8.5, 0.2-0.4% (w/v) Cystamine, 0.2 M $LiSO_4$, 8% (w/v) PEG 20'000, 8% (w/v) PEG 550 MME using sitting drop vapor diffusion at 20 °C. TRIM20Δ413 (7.5 mg/ml) was mixed in a 1:1 ratio with mother liquor. The obtained crystals were used for micro-seeding in 0.1 M Tris-AcOH, pH 7.4-8.0, 0.26% (w/v) Cystamine, 0.2 M $LiSO_4$, 8% (w/v) PEG 20'000, 8% (w/v) PEG 550 MME using sitting drop vapor diffusion at 20 °C. The protein sample was concentrated to 5 mg/ml and mixed in a 1:1 ratio. Crystals grew within 24 h and were fished within 18 days. Prior to flash freezing in liquid nitrogen, crystals were soaked in the mother liquor supplemented with 20% (v/v) ethylene glycol. A native data set of a TRIM20Δ413 crystal was recorded at the X06SA beam line of the Swiss Light Source (Paul-Scherrer Institut, Villigen, Switzerland). The protein crystallized in $P2_1$ with 6 molecules in the asymmetric unit forming 3 dimers. Data was indexed, integrated and scaled with XDS(35) to a resolution of 2.4 Å. Molecular replacement was done with Phaser (36) using the B30.2 domain of TRIM20 as search model (pdb entry: 2WL1). Model building and manual fitting was done in Coot (37). Refinement was performed with Phenix (38). In the final model, 98% of all residues are in the favored ramachandran area and no outliers. The accession code is 4cg4.

Acknowledgements

We would like to thank the late Prof. J. Tschopp (University of Lausanne, Switzerland) for providing us with the DNA for the *MEFV* gene. We also thank Beat Blattmann and Celine Stutz-Ducommun of the NCCR crystallization facility and the staff of the Swiss Light Source (PSI, Villigen, Switzerland). Thilo Schroeder provided us the plasmid for pro-IL-1β. Stefan Schauer and Manfred Rössle are thanked for the support in surface plasmon resonance and SAXS experiments, respectively. Andreas Flütsch is thanked for carefully reviewing the manuscript. CW was participant of the Biomolecular Structure and Function PhD program of the NCCR Structural Biology. This work was financially supported by a Swiss National Science Foundation grant (No. 31-1022181 to M.G.G.).

References

1. Han K, Lou DI, & Sawyer SL (2011) Identification of a genomic reservoir for new TRIM genes in primate genomes. *PLoS Genet* 7(12):e1002388.
2. Ozato K, Shin DM, Chang TH, & Morse HC, 3rd (2008) TRIM family proteins and their emerging roles in innate immunity. *Nat Rev Immunol* 8(11):849-860.
3. Reymond A*, et al.* (2001) The tripartite motif family identifies cell compartments. *Embo J* 20(9):2140-2151.
4. Diaz-Griffero F*, et al.* (2009) A B-box 2 surface patch important for TRIM5alpha self-association, capsid binding avidity, and retrovirus restriction. *J Virol* 83(20):10737-10751.
5. Mrosek M*, et al.* (2008) Structural analysis of B-Box 2 from MuRF1: identification of a novel self-association pattern in a RING-like fold. *Biochemistry* 47(40):10722-10730.
6. Yu JW*, et al.* (2007) Pyrin activates the ASC pyroptosome in response to engagement by autoinflammatory PSTPIP1 mutants. *Mol Cell* 28(2):214-227.
7. Grutter C*, et al.* (2006) Structure of the PRYSPRY-domain: implications for autoinflammatory diseases. *FEBS Lett* 580(1):99-106.
8. Rhodes DA & Trowsdale J (2007) TRIM21 is a trimeric protein that binds IgG Fc via the B30.2 domain. *Mol Immunol* 44(9):2406-2414.
9. Stremlau M, Perron M, Welikala S, & Sodroski J (2005) Species-specific variation in the B30.2(SPRY) domain of TRIM5alpha determines the potency of human immunodeficiency virus restriction. *J Virol* 79(5):3139-3145.
10. Chae JJ, Aksentijevich I, & Kastner DL (2009) Advances in the understanding of familial Mediterranean fever and possibilities for targeted therapy. *Br J Haematol* 146(5):467-478.
11. Martinon F, Hofmann K, & Tschopp J (2001) The pyrin domain: a possible member of the death domain-fold family implicated in apoptosis and inflammation. *Curr Biol* 11(4):R118-120.
12. Kohl A & Grutter MG (2004) Fire and death: the pyrin domain joins the death-domain superfamily. *C R Biol* 327(12):1077-1086.
13. Anonymous (1997) A candidate gene for familial Mediterranean fever. *Nat Genet* 17(1):25-31.
14. Anonymous (1997) Ancient missense mutations in a new member of the RoRet gene family are likely to cause familial Mediterranean fever. The International FMF Consortium. *Cell* 90(4):797-807.
15. Papin S*, et al.* (2007) The SPRY domain of Pyrin, mutated in familial Mediterranean fever patients, interacts with inflammasome components and inhibits proIL-1beta processing. *Cell Death Differ* 14(8):1457-1466.
16. Yu JW*, et al.* (2006) Cryopyrin and pyrin activate caspase-1, but not NF-kappaB, via ASC oligomerization. *Cell Death Differ* 13(2):236-249.
17. Gavrilin MA*, et al.* (2012) Activation of the pyrin inflammasome by intracellular Burkholderia cenocepacia. *J Immunol* 188(7):3469-3477.
18. Yu JW, Farias A, Hwang I, Fernandes-Alnemri T, & Alnemri ES (2013) Ribotoxic Stress through p38 Mitogen-activated Protein Kinase Activates in Vitro the Human Pyrin Inflammasome. *J Biol Chem* 288(16):11378-11383.
19. Roa A*, et al.* (2012) RING domain mutations uncouple TRIM5alpha restriction of HIV-1 from inhibition of reverse transcription and acceleration of uncoating. *J Virol* 86(3):1717-1727.
20. Perfetto L*, et al.* (2013) Exploring the diversity of SPRY/B30.2-mediated interactions. *Trends Biochem Sci* 38(1):38-46.
21. Javanbakht H*, et al.* (2006) Characterization of TRIM5alpha trimerization and its contribution to human immunodeficiency virus capsid binding. *Virology* 353(1):234-246.

22. Sardiello M, Cairo S, Fontanella B, Ballabio A, & Meroni G (2008) Genomic analysis of the TRIM family reveals two groups of genes with distinct evolutionary properties. *BMC Evol Biol* 8:225.
23. Langelier CR*, et al.* (2008) Biochemical characterization of a recombinant TRIM5alpha protein that restricts human immunodeficiency virus type 1 replication. *J Virol* 82(23):11682-11694.
24. Mallery DL*, et al.* (2010) Antibodies mediate intracellular immunity through tripartite motif-containing 21 (TRIM21). *Proc Natl Acad Sci U S A* 107(46):19985-19990.
25. Pertel T*, et al.* (2011) TRIM5 is an innate immune sensor for the retrovirus capsid lattice. *Nature* 472(7343):361-365.
26. Stremlau M*, et al.* (2006) Specific recognition and accelerated uncoating of retroviral capsids by the TRIM5alpha restriction factor. *Proc Natl Acad Sci U S A* 103(14):5514-5519.
27. Sastri J*, et al.* (2010) Identification of residues within the L2 region of rhesus TRIM5alpha that are required for retroviral restriction and cytoplasmic body localization. *Virology* 405(1):259-266.
28. Ganser-Pornillos BK*, et al.* (2011) Hexagonal assembly of a restricting TRIM5alpha protein. *Proc Natl Acad Sci U S A* 108(2):534-539.
29. Tao H*, et al.* (2008) Structure of the MID1 tandem B-boxes reveals an interaction reminiscent of intermolecular ring heterodimers. *Biochemistry* 47(8):2450-2457.
30. Lienlaf M*, et al.* (2011) Contribution of E3-ubiquitin ligase activity to HIV-1 restriction by TRIM5alpha(rh): structure of the RING domain of TRIM5alpha. *J Virol* 85(17):8725-8737.
31. Sebastian S & Luban J (2005) TRIM5alpha selectively binds a restriction-sensitive retroviral capsid. *Retrovirology* 2:40.
32. Li X, Yeung DF, Fiegen AM, & Sodroski J (2011) Determinants of the higher order association of the restriction factor TRIM5alpha and other tripartite motif (TRIM) proteins. *J Biol Chem* 286(32):27959-27970.
33. Milhavet F*, et al.* (2008) The infevers autoinflammatory mutation online registry: update with new genes and functions. *Hum Mutat* 29(6):803-808.
34. McEwan WA*, et al.* (2013) Intracellular antibody-bound pathogens stimulate immune signaling via the Fc receptor TRIM21. *Nat Immunol* 14(4):327-336.
35. Kabsch W (2010) Xds. *Acta Crystallogr D Biol Crystallogr* 66(Pt 2):125-132.
36. McCoy AJ*, et al.* (2007) Phaser crystallographic software. *J Appl Crystallogr* 40(Pt 4):658-674.
37. Emsley P, Lohkamp B, Scott WG, & Cowtan K (2010) Features and development of Coot. *Acta Crystallogr D Biol Crystallogr* 66(Pt 4):486-501.
38. Adams PD*, et al.* (2010) PHENIX: a comprehensive Python-based system for macromolecular structure solution. *Acta Crystallogr D Biol Crystallogr* 66(Pt 2):213-221.

Figure legends

Figure 1

Central position of the CHS domain in TRIM proteins and its importance in dimerization. (*A*) Schematic representation of the domains of TRIM proteins comprising a RING, B-Box, and CHS domain. In the literature the CHS domain is referred to as coiled coiled domain with a L2 linker that connects to the C-terminal B30.2 domain. TRIM20 is a RING-less TRIM member and has a long N-terminal insertion composed of a PYD domain and a long linker region. For crystallization a construct starting at position 414 was designed. (*B*) Sedimentation velocity analytical ultracentrifugation of the B30.2 domain and the CHS-B30.2 fragment of TRIM20 show a monomer and a dimer, respectively. The calculated monomeric masses are 23.305 kDa and 42.737 kDa for the B30.2 domain and the TRIM20Δ413 construct, respectively.

Figure 2

Crystal structure of TRIM20Δ413. The crystal structure of one of the three dimers (chain A and B) in the asymmetric unit is presented. The chains of monomer A and B are colored in blue and red, respectively. The helices of each CHS monomer are numbered α-1 to α-4. The parts of the CHS domain that show a 2 helical (2-CC) or 3 helical coiled coil (3-CC) are indicated and depicted in more detail in *B*. (*A*) The dimer is shown from a side and a top view and its dimensions indicated. (*B*) Residues involved in the 2-CC (top) and 3-CC (bottom) are shown as sticks and labeled in the corresponding color of the helix. (*C*) Topology of the CHS domain including its structural motifs are shown schematically.

Figure 3

Tetramer interface. (*A*) The crystal contact between two dimers is shown in a cartoon representation. Chain A and B are colored as in Fig. 2. The second dimer made of chain C and D is colored in orange and green, respectively. The black box indicates the display detail shown in *B*. (*B*) Detailed view of half of the tetramer interface. Residues involved in the interface are depicted in sticks and hydrogen bonds are indicated by black dashed lines. The coordinated water between the B30.2 domains is shows as a red sphere.

Figure 4

Solution structure of TRIM20Δ413. (*A*) Data extrapolated to infinite dilution is shown together with the fits of the crystal structure and rigid body modeling with the indicated χ^2 values. (*B*) The crystal structure is shown in a cartoon representation next to the (*C*) rigid body model. The orientation found to be similar to the crystal structure is shown in a blue surface representation. The other orientation of the B30.2 domain found in the rigid body fit is colored violet.

Figure 5

Interaction between TRIM20 and pro-IL-1β. (A) 10 µM of the indicated TRIM20 constructs were incubated with 10 µg FLAG-tagged pro-IL-1β in 100 µl total volume. Complex was co-immunoprecipitated using ANTI-FLAG® M2 Affinity Gel (Sigma-Aldrich) and subjected to SDS-PAGE analysis. (B) TRIM20Δ413, pro-IL-1β and a mixture of both proteins (complex) were incubated at room temperature and their SEC elution profiles are shown with the corresponding retention volumes of 1.27 ml, 1.64 ml, and 1.81 ml for the complex, TRIM20Δ413 and pro-IL-1β, respectively. Co-elution of both proteins in the appearing complex peak was verified by SDS-PAGE of the fractions indicated by black horizontal bars. Number 1 and 2 indicate the bands corresponding to TRIM20Δ413 and pro-IL-1β, respectively. The asterisks indicate TRIM20 multimers.

Figure 6

Models of TRIM full length and lattice formation. (*A*) The modeled TRIM full length structure is shown in a cartoon representation with the B30.2 domain, CHS, B-Box2, and RING domain colored in orange, red, green, and blue, respectively. The coordinated Zn^{2+} atoms are shown in grey spheres. (*B*) Schematic drawing showing the dimensions of the reported hexagonal lattice formed by a TRIM21/TRIM5α chimera (28). Part of the lattice that is shown in detail in *C* and *D* is indicated in red with the central 3-fold axis depicted by the black triangle. (*C*) The currently proposed model suggests parallel arranged TRIM dimers that form tetramers via a L2/L2 contact. The tetramers assemble via B-Box/B-Box interactions into the hexagonal lattice. (*D*) Lattice formation using the B30.2 dependent tetramer as observed in the TRIM20 crystal. The revealed flexibility of the B30.2 domains is indicated by the arrows.

Figures

Figure 1

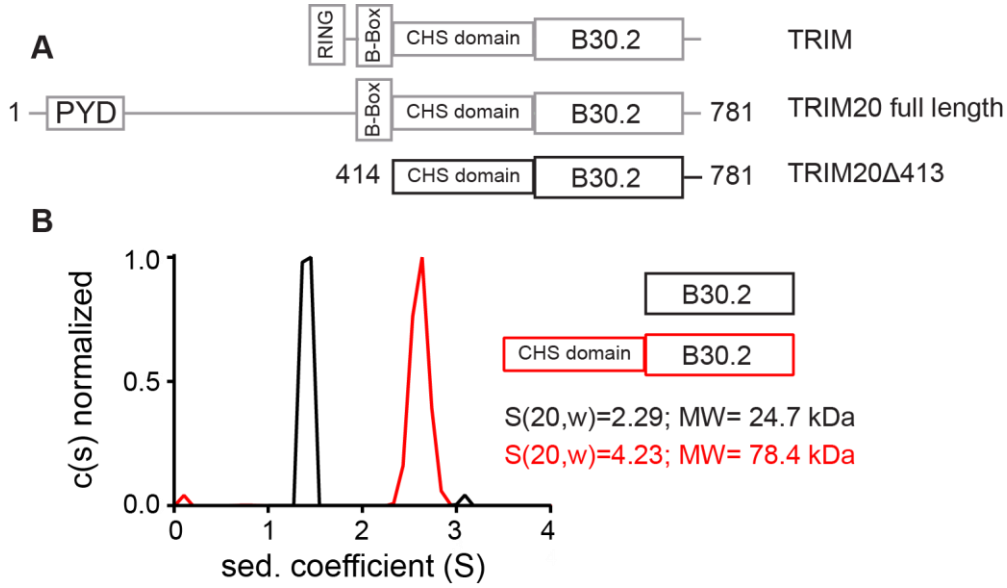

Figure 2

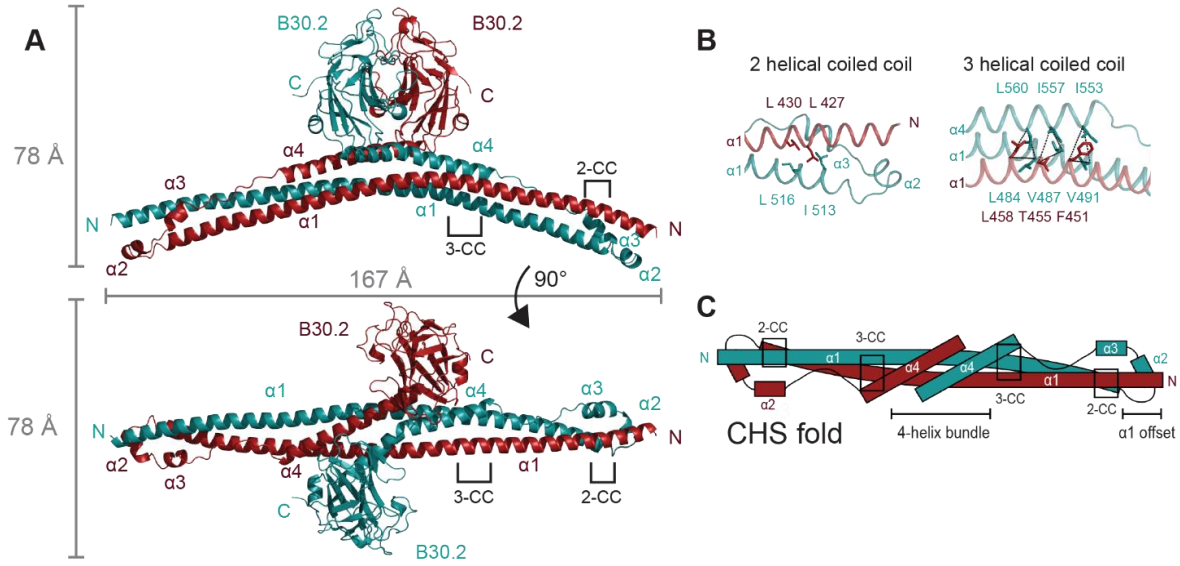

Figure 3

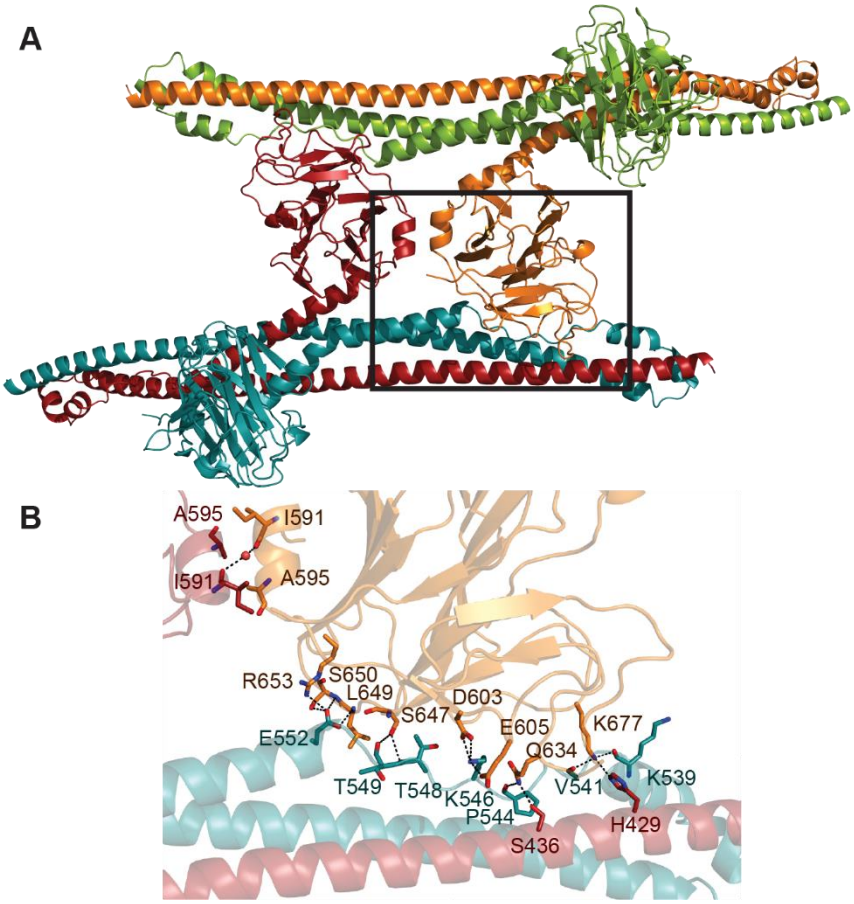

Figure 4

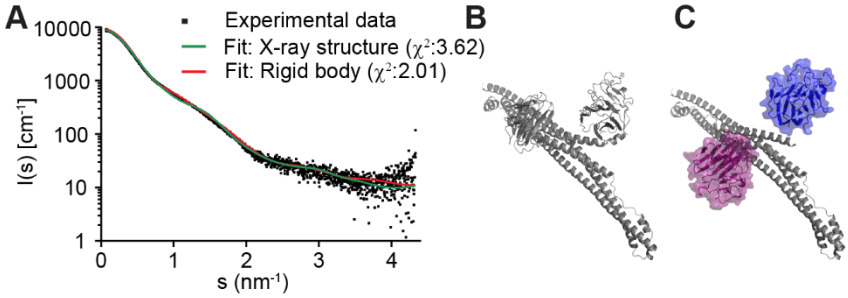

Figure 5

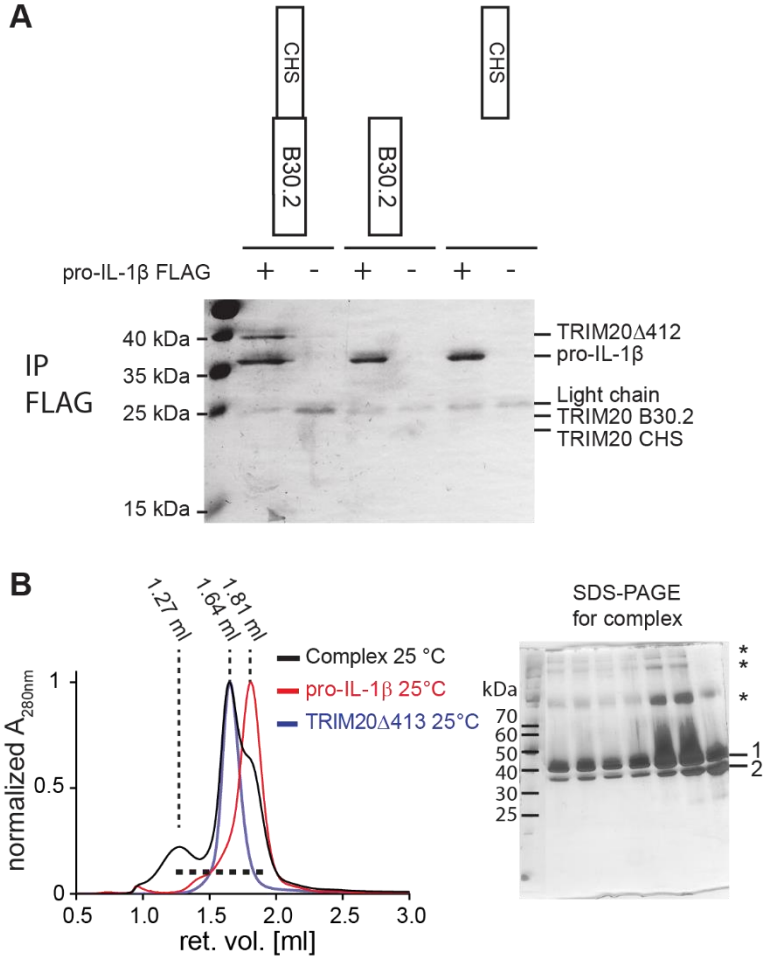

Figure 6

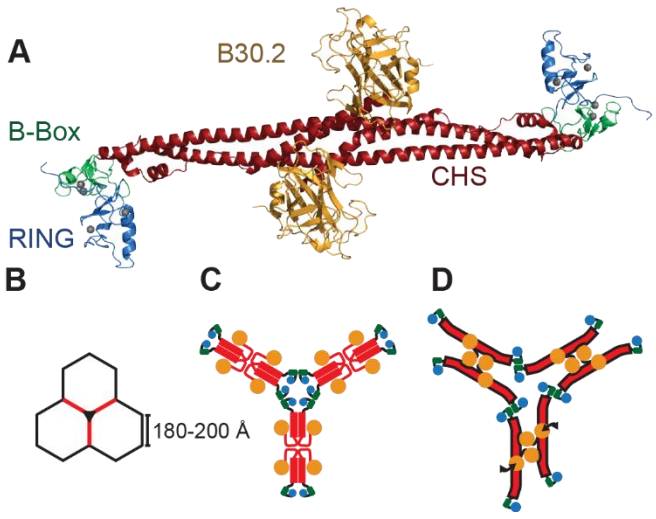

4.2 Supporting Information

SI Methods

Construction of Expression Plasmids

The multiple cloning site 1 (MCS1) of the transfer vector pFBDM (1) was modified to enable fragment exchange (FX) cloning (2). The *Sap*I restriction site between the transposon element Tn7R and the Col-E1 origin of replication was removed using Quikchange mutagenesis (Invitrogen). An *Nde*I restriction site was inserted into the MCS1 by Quikchange. The FX-cassette of the pBXC3H vector (2) was used as template (incl. coding region for C-terminal His_{10}-tag and 3C cleavage site) and cloned into the modified pFBDM vector using *Nde*I and *Xba*I restriction sites yielding a pFX3CH vector. The *Nde*I restriction site was later removed. All TRIM20 constructs and human TRIM5αΔ132 were cloned into the pFX3CH template vector. Primers and coding regions are stated in Table S4.

A similar procedure as for pFX3CH was applied to modify a pET28 (Novagen) vector. The *Sap*I site near the BR322 origin of replication was removed with Quikchange. The FX-cassette of pBXH3C (incl. coding region for N-terminal His_{10}-tag and 3C-cleavage site) was inserted using the *NdeI* and *XhoI* restriction yielding a pET28-FXH3C vector. Pro-IL-1β (codon optimized for *E.coli* expression) was cloned into the pET28-FXH3C vector using primers as stated in Table S4.

Expression and Purification

All TRIM constructs were expressed in *Sf*9 cells using the manufactures protocol (Invitrogen). Cells were harvested after 48-72 h expression at 27 °C. *Sf*9 cells expressing TRIM20Δ413 were lysed in lysis buffer (50 mM Tris-HCl, pH 8, 300 mM NaCl, 20 mM imidazole, DNAse I, RNase I, Benzoase, and EDTA-free complete inhibitor cocktail (Roche Diagnostics)) using an Emulsi-Flex C3 homogenizer (Avestin, Canada). Cell debris was centrifuged (1 h, 4 °C, 20'000 rpm) and supernatant applied to Protino Ni-NTA agarose (Machery Nagel). His-tag was cleaved by His-3C Protease, the sample dialysed in 50 mM Tris-HCl, pH 8, 150 mM NaCl, 10 mM imidazole, 0.5 mM TCEP, and reapplied to Ni-NTA agarose. Cleaved TRIM20Δ413 was dialyzed in low salt buffer (20 mM Tris-HCl, pH 8, 50 mM NaCl, 0.5 mM TCEP) and applied on a RESOURCE Q anion exchange column (GE Healthcare). The protein was eluted with 7.5% high salt buffer (20 mM Tris-HCl, pH 8, 1 M NaCl, 0.5 mM TCEP) and dialysed in 20 mM Tris-HCl, pH 8, 100 mM NaCl, 0.5 mM TCEP. The protein could be stored at 4 °C for up to two weeks, or it was frozen in liquid nitrogen and stored at -80 °C until further use.

Human TRIM5Δ132 was purified as described above and after His-tag removal applied on a Superdex 200 (10/300 GL; GE Healthcare; 50 mM Tris-HCl, pH 8, 100 mM NaCl, 0.5 mM TCEP). Fractions containing dimeric human TRIM5Δ132 were pooled and stored at 4°C until further use.

All other TRIM constructs were lysed using 0.5% CHAPS in lysis buffer, and purified as described above. After His-tag removal the proteins were applied on a Superdex 200 (10/300 GL; GE Healthcare; 50 mM Tris-HCl, pH 8, 150 mM NaCl, 0.5 mM TCEP). Proteins were stored at 4°C or frozen in liquid nitrogen after addition of glycerol to a final concentration of 8.7% (v/v). For TRIM20-CHS 300 mM NaCl was used throughout the purification. For TRIM20Δ303 400 mM NaCl was used in the elution buffer and for SEC chromatography to separate TRIM20Δ303 from aggregates. Fractions corresponding to dimeric TRIM20Δ303 were pooled and analyzed in a second SEC in 50 mM Tris-HCl, pH 8, 150 mM NaCl, and 0.5 mM TCEP.

Pro-IL-1β was expressed in *E.coli* BL21 (DE3) strain. Cells were grown in LB-media at 30 °C to an OD_{600nm} of 0.8, cooled down at 4°C for 30 min and expression induced with 0.1 mM IPTG (OD_{600nm} of 1.0). After 15 h expression at 18 °C, cells were harvested (4°C, 20 min, 4000 rpm) and lysed in 50 mM Tris-HCl, pH 8, 150 mM NaCl, 10 mM imidazole, DNAse I, RNase I, lysozyme, 0.5 mM PMSF, EDTA-free complete inhibitor cocktail (Roche Diagnostics) using an Emulsi-Flex C3 homogenizer (Avestin, Canada). Lysate was cleared and supernatant applied to Ni-NTA agarose. His-tag was cleaved by His-3C Protease, the sample dialysed in 50 mM Tris-HCl, pH 8, 50 mM NaCl, 0.25 mM TCEP) and reapplied to Ni-NTA agarose. As a final purification step the sample was applied on a Superdex 200 in 50 mM Tris-HCl, pH 8, 50 mM NaCl, 0.5 mM TCEP). Fractions corresponding to monomeric pro-IL-1β were pooled and either used directly or frozen in liquid nitrogen after the addition of 8.7% glycerol and stored at -80 °C.

Co-IP experiments

10 µg of FLAG-pro-IL-1β were incubated with 10 µM TRIM20Δ412, TRIM20-B30.2 or TRIM20-CHS in a total volume of 100 µl (50 mM Tris-HCl, pH 7.4, 50 mM NaCl, 0.05% Tween 20). The mixture was incubated for 30 min at room temperature (RT) to allow complex formation. Putative complexes were co-immunoprecipitated using 20 µl ANTI-FLAG® M2 Affinity Gel (Sigma-Aldrich) for 10 min at RT. Beads were washed 3 times, and proteins eluted with 45 µl 2x SDS loading buffer. Eluted samples were analyzed by SDS-PAGE and visualized using silver staining (3).

Surface Plasmon Resonance

The interaction between TRIM20Δ412 and pro-IL-1β was measured on a ProteOn™ XPR 36 using a ProteOn™ GCL sensor chip (Bio Rad) equilibrated with running buffer (PBS, pH 7.5, 0.02% Tween 20). Monoclonal Anti-c-Myc IgG1 (20 µg/ml in 10 mM acetate, pH 5; Roche Diagnostics) was immobilized using amine coupling chemistry until the chip was saturated (6000-6400 RU). TRIM20Δ412 (1 µM) was applied to the immobilized antibody in running buffer and equilibrated until a stable baseline was reached (550-600 RU TRIM20Δ412; ΔRU < 0.2 RU/min). In total 5 lanes were immobilized with TRIM20Δ412. The sixth lane was coated with antibody only and used as a reference for unspecific binding. Single shot kinetic

was applied using a two-fold dilution series of pro-IL-1β in running buffer (1.56, 3.125, 6.25, 12.5, 25 µM). For each lane two single shot experiments were performed. Data was double referenced against buffer and the antibody control lane. Binding affinity (K_D) was determined kinetically for each experiment using the heterogenous ligand model implemented in the ProteOn™-Software (Bio Rad). The mean and standard deviation of the measured K_Ds was determined using GraphPad Prism6 (GraphPad Software).

Size exclusion chromatography analysis of complex formation

TRIM20Δ413 was mixed with freshly prepared pro-IL-1β. 3 mg of each protein were mixed and concentrated to a final concentration of 19 mg/ml. The buffer was exchanged to 20 mM Tris-HCl, pH 8, 100 mM NaCl, 0.5 mM TCEP while concentrating. Individual proteins were concentrated to 8 mg/ml and buffer was exchanged as for the complex. Samples were incubated for 60 min at room temperature or 20 h at 4 °C, centrifuged (14'000 g, 10 min, 4 °C) and 5 µl injected onto a Superdex 200 (5/150 GL, GE Healthcare) in 20 mM Tris-HCl, pH 8, 100 mM NaCl, 0.5 mM TCEP at 4 °C. 50 µl fractions were collected, analyzed by SDS-PAGE and visualized using silver staining.

Small-angle X-ray scattering

SAXS data were collected at the Petra III (P62) beam line at the Deutsches Elektronen Synchroton (DESY), Hamburg. The incident wavelength was 1.24 Å. Data was recorded on a 2M Pilatus detector for the angular range of s between 0.0668-4.336 nm^{-1} ($s=4\pi \sin(\theta)/\lambda$, where $2*\theta$ is the diffraction angle and λ the wavelength of the incident beam). All samples were measured at 10 °C. TRIM20Δ413 was measured in PBS and 5 mM DTT at several concentrations (1.7, 2.88, 4.6, 8.75, 13.3 mg/ml). TRIM20Δ303 was measured at several concentration (0.87, 6.1, 8.7 mg/ml) in 20 mM Tris-HCl, pH 8, 400 mM NaCl, 1 mM TCEP. TRIM5Δ132 was concentrated to 10 mg/ml and injected onto a Superdex 200 (10/300 GL; GE Healthcare; 50 mM Tris-HCl, pH 8, 100 mM NaCl, 0.5 mM TCEP) prior to SAXS data collection. Peak fractions were measured by SAXS immediately after elution from size exclusion. Data was processed with PRIMUS (4) and a scattering curve extrapolated to infinite dilution was created using ALMERGE (5). The pair distribution function (P (r)) was calculated with GNOM (6). Radius of gyration R_G was estimated from the Guinier plot using PRIMUS and the P (r) function using GNOM. Rigid body modeling was carried out in CORAL(7) defining residues 586-590 of TRIMas a flexible linker. Comparison with the crystal structure and the experimental scattering profile was done with CRYSOL(8). The P(r) function of the X-ray structure and the rigid body fit was generated using SOMO (9).

Sequence alignment

Sequences used correspond to the UniProt entries O15553, Q9C035, P19474, Q8IYM9, P14373 for TRIM20, TRIM5α, TRIM21, TRIM22, TRIM27, respectively.

Alignments were generated using T-coffee (10) and Jalview (11). Coiled coil predictions are taken from secondary structure predictions using Jpred 3 (12).

Modeling

The TRIM full-length model was generated using the MODELLER software (version 9.12) (13). Homology modeling was performed according to the Advanced Tutorial on the MODELLER homepage (http://salilab.org/modeller/tutorial/advanced.html) with a few modifications. The templates for the modeled RING and for the modeled B-Box were aligned separately using the SALIGN function and were subsequently merged manually to yield one multiple structure alignment for all the templates. TRIM5 RING (pdb entry 2ECV, residues 8-69 (14)) and B-Box1 of the TRIM18 tandem B-Boxes (pdb entry 2JUN, residues 114-173 (15)) served as templates for the modeled RING. TRIM5 B-Box (pdb entry 2YRG, residues 8-51 (16)), TRIM29 B-Box (pdb entry 2CSV, residues 16-63) and B-Box2 of the TRIM18 tandem B-Boxes (pdb entry 2JUN, residues 171-214) were taken as templates for the modeled B-Box. The target sequence, corresponding to residues 1-131 of human TRIM5α followed by residues 413-419 of TRIM20, was aligned to the pre-aligned template structures using the SALIGN function. To incorporate the zinc atoms into the modeling process, following lines were added to the alignment and modeling scripts: Env.io.atom_files_directory = ['.', '../atom_files'] and env.io.hetatm = True. The final multiple sequence alignment of template structures and target sequence is shown in Supplementary Fig. 4. A tandem model of RING and BBox domains was built using the automodel class of MODELLER and structurally aligned onto the TRIM20Δ413 structure via the shared pyrin residues 413-419 yielding the TRIM full-length model.

Analytical ultracentrifugation

The B30.2 domain, expressed and purified as described (17), and TRIM20Δ413 were measured in PBS (pH 7.4) 10 mM β-Mercaptoethanol at a concentration of 0.6 mg/ml and 0.8 mg/ml, respectively. The sedimentation velocity measurements were carried out at 4°C on a ProteomeLab XL-1 (Beckman Coulter) ultracentrifuge at a speed of 30000 rpm. Data was analyzed with SEDFIT (18).

References

1. Berger I, Fitzgerald DJ, & Richmond TJ (2004) Baculovirus expression system for heterologous multiprotein complexes. *Nat Biotechnol* 22(12):1583-1587.
2. Geertsma ER & Dutzler R (2011) A versatile and efficient high-throughput cloning tool for structural biology. *Biochemistry* 50(15):3272-3278.
3. Nesterenko MV, Tilley M, & Upton SJ (1994) A simple modification of Blum's silver stain method allows for 30 minute detection of proteins in polyacrylamide gels. *J Biochem Biophys Methods* 28(3):239-242.
4. Konarev PV, Volkov VV, Sokolova AV, Koch MHJ, & Svergun DI (2003) PRIMUS: a Windows PC-based system for small-angle scattering data analysis. *J Appl Crystallogr* 36(5):1277-1282.
5. Franke D, Kikhney AG, & Svergun DI (2012) Automated acquisition and analysis of small angle X-ray scattering data. *Nuclear Instruments and Methods in Physics Research Section A: Accelerators, Spectrometers, Detectors and Associated Equipment* 689(0):52-59.
6. Svergun D (1992) Determination of the regularization parameter in indirect-transform methods using perceptual criteria. *J Appl Crystallogr* 25(4):495-503.
7. Petoukhov MV*, et al.* (2012) New developments in the ATSAS program package for small-angle scattering data analysis. *J Appl Crystallogr* 45(2):342-350.
8. Svergun D, Barberato C, & Koch MHJ (1995) CRYSOL– a Program to Evaluate X-ray Solution Scattering of Biological Macromolecules from Atomic Coordinates. *J Appl Crystallogr* 28(6):768-773.
9. Rai N*, et al.* (2005) SOMO(SOlution MOdeler): Differences between X-ray- and NMR-derived bead models suggest a role for side chain flexibility in protein hydrodynamics. *Structure* 13(5):723-734.
10. Keller O, Kollmar M, Stanke M, & Waack S (2011) A novel hybrid gene prediction method employing protein multiple sequence alignments. *Bioinformatics* 27(6):757-763.
11. Waterhouse AM, Procter JB, Martin DM, Clamp M, & Barton GJ (2009) Jalview Version 2--a multiple sequence alignment editor and analysis workbench. *Bioinformatics* 25(9):1189-1191.
12. Cole C, Barber JD, & Barton GJ (2008) The Jpred 3 secondary structure prediction server. *Nucleic Acids Res* 36(Web Server issue):W197-201.
13. Eswar N*, et al.* (2007) Comparative protein structure modeling using MODELLER. *Curr Protoc Protein Sci* Chapter 2:Unit 2 9.
14. Lienlaf M*, et al.* (2011) Contribution of E3-ubiquitin ligase activity to HIV-1 restriction by TRIM5alpha(rh): structure of the RING domain of TRIM5alpha. *J Virol* 85(17):8725-8737.
15. Tao H*, et al.* (2008) Structure of the MID1 tandem B-boxes reveals an interaction reminiscent of intermolecular ring heterodimers. *Biochemistry* 47(8):2450-2457.
16. Diaz-Griffero F*, et al.* (2009) A B-box 2 surface patch important for TRIM5alpha self-association, capsid binding avidity, and retrovirus restriction. *J Virol* 83(20):10737-10751.
17. Weinert C, Grutter C, Roschitzki-Voser H, Mittl PR, & Grutter MG (2009) The crystal structure of human pyrin b30.2 domain: implications for mutations associated with familial Mediterranean fever. *J Mol Biol* 394(2):226-236.
18. Schuck P (2000) Size-distribution analysis of macromolecules by sedimentation velocity ultracentrifugation and lamm equation modeling. *Biophys J* 78(3):1606-1619.
19. Krissinel E & Henrick K (2004) Secondary-structure matching (SSM), a new tool for fast protein structure alignment in three dimensions. *Acta Crystallogr D Biol Crystallogr* 60(Pt 12 Pt 1):2256-2268.
20. Sokolova AV, Volkov VV, & Svergun DI (2003) Prototype of a database for rapid protein classification based on solution scattering data. *J Appl Crystallogr* 36:865-868.

Supplementary Figure legends

Figure S1

Sequence alignment of the CHS domain of several TRIM20 homologues. Identical and similar residues are depicted by black and grey boxes, respectively. The predicted bipartite coiled coils for every TRIM are indicated by lines on top of the sequences and colored as indicated next to the protein names. The predicted L2 linker is marked by the grey line. Secondary structure elements as seen in the TRIM20 structure are indicated below the sequences. Residues that form the 2 helical coiled coil (2-CC) and 3 helical coil coiled (3-CC) are connected by black lines.

Figure S2

Different dimers in the asymmetric unit. Three dimers are found in the asymmetric unit (chains A&B, C&D, and E&F). For visualization only dimer of chain A&B and C&D were used. Dimer of chain E&F is similar as dimer CD. (*A*) Superposition of the TRIM20 dimers are shown in a top and side view. The chains are colored in blue, red, orange and green for monomer A, B, C and D, respectively. (*B*) For a better visualization of the differences between the CHS monomers residues 486-560 of each monomer were superposed using Superpose (19). For each monomer the corresponding second protomer is shown in transparent black. (*C*) The hinge region between the helix α4 and the B30.2 domain is visualized by superposing the first N-terminal helix of each B30.2 domain (residues 590-595, shown in black). Helix α4 of each monomer is colored as in *A* and *B*.

Figure S3

TRIM5Δ132 dimer-tetramer. (*A*) Size exclusion profile of TRIM5Δ132 reveals the presence of two oligomeric states. Fraction of the peak 1 that was reinjected unto SEC is indicated by the black bar. Its SEC profile is shown in the middle of the panel, showing an identical elution profile. SDS-PAGE analysis of all fractions of peak 1 and 2 are shown on the left indicating that both peaks origin from TRIM5Δ132. (*B*) Immediately after SEC peak 1 and 2 were analyzed by SAXS. The resulting scattering curves are plotted in log X-log Y manner. Their guinier plot is shown in the inlet and reveals linear behavior for both species. (*C*) Scattering profile of peak 1 & 2 are shown together with the calculated curves of the TRIM20Δ413 tetrameric and dimeric structure, respectively. (*D*) Biophysical values for TRIM5αΔ132 obtained by SEC and SAXS analysis are stated in comparison to the calculated values for TRIM20Δ413. Values were obtained using[1)] DARA (20), [2)] CRYSOL, [3)] see Table S2, [4)] based on amino acid sequence, [5)] and via mass spectrometry analysis of the monomer.

Figure S4

SAXS data. (*A*) and (*B*) Overlay of experimental scattering curves are shown for all measured concentrations as indicated. For structural modeling a dataset was

created corresponding to an infinite dilution. In (*A*) and (*B*) the data is plotted as X-log Y and log X-log Y, respectively, with the error bars depicted as lines in the corresponding color. (*C*) For the dataset extrapolated to infinite dilution (black dots) the guinier plot (black line) shows linearity without signs of interparticle attraction. (*D*) The Krakty-plot (black dots) shows a typical curve for a two domain protein with interdomain flexibility. The errors are depicted by grey lines. (*E*) The P(r) curve approaches zero for r = rmax. For r = 0, P(r) does not fully approach zero suggesting a minimal mismatch of the buffers in the sample and in the buffer control. (*F*) Overlay of the P(r) curve derived from the experimental data, the crystal structure and the rigid body fit is shown.

Figure S5

Binding of TRIM20 to pro-IL-1β. (*A*) Typical sensogram of the SPR measurements is shown. Myc-TRIM20Δ412 was immobilized and a dilution series of pro-IL-1β, as indicated, was subjected (black lines). The obtained fit for every concentration using the heterogeneous ligand model is shown by the grey lines and the resulting K_Ds and their standard deviations (s.d.) are stated. (*B*) SEC profile for pro-IL-1β, TRIM20Δ413 and a mixture of both proteins incubated for 20 h at 4 °C are shown in the corresponding color. The dotted lines indicate the retention volumes for the individual proteins and the complex as seen in Fig. 5*B*. (*C*) SEC profile of a mixture of both proteins (Complex) incubated at room temperature is shown (left y-axis). The fraction that was reinjected is indicated by the black bar and its SEC profile shown (Reinject complex; right y-axis).

Figure S6

Modeling a stereotype TRIM full length protein. (*A*) The periphery of the TRIM20 CHS domain and the NMR structure of the TRIM29 B-Box (pdb code: 2CSV) are shown in a cartoon representation. A sequence alignment of the structural overlap between the two structures is shown in the middle. Residues of the B-Box are colored in green. Residues that overlap in both structures are colored solid black while the rest of the CHS domain is colored transparent red. (*B*) The structure of the TRIM18 B-Box1/2 tandem motif (pdb code: 2JUN (15)), the TRIM5α RING (pdb code: 2ECV (14)), and the TRIM5α B-Box2 (pdb code: 2YRG (16)) are shown in a cartoon representation. (*C*) Multiple sequence alignment of the template structures TRIM5 RING, TRIM5 B-Box, TRIM29 B-Box and TRIM18 tandem B-Boxes (pdb entries 2ECV, 2YRG, 2CSV and 2JUN, respectively) and the target sequence used for homology modeling. Numbering of residues correspond to the pdb entries including the zinc atoms (z). Residues of the RING, B-Box and CHS domains are framed in blue, green and red, respectively. (*D*) Schematic representation of the TRIM20Δ303 construct and a TRIM full length protein. SEC profile and SDS-PAGE of the purified TRIM20Δ303are depicted. The corresponding elution volumes on a S200 (10/300) are indicated. Scattering curves of TRIM20Δ303 and a merged curve are illustrated in a X-log Y (*E*) and log X-log Y (*F*) manner. The guinier plot

(*G*), Krakty plot (*H*), and the radial distribution (*I*) are shown for the merged scattering curve. (*K*) The biophysical properties of TRIM20Δ303 are listed in comparison to the calculated values of the presented full length TRIM model. [1)] The experimental molecular weight (MW) of TRIM20Δ303 was calculated using the I(0) of TRIM20Δ413 as standart (see Table S2). [2)] The calculated MW is based on the amino acid sequence. [3)] Values were derived using CRYSOL.

Supplementary Figures

Figure S1

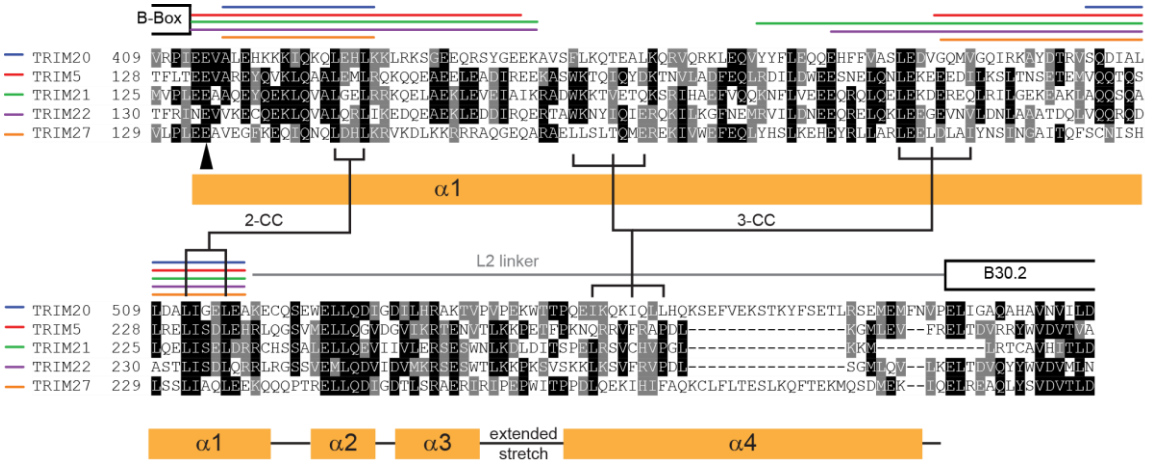

Figure S2

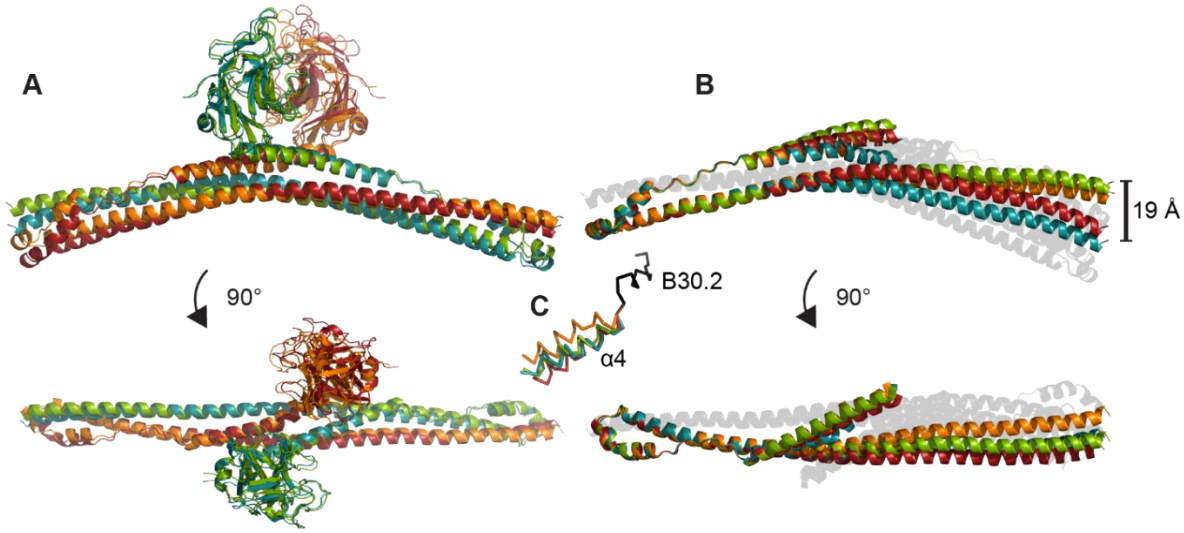

Figure S3

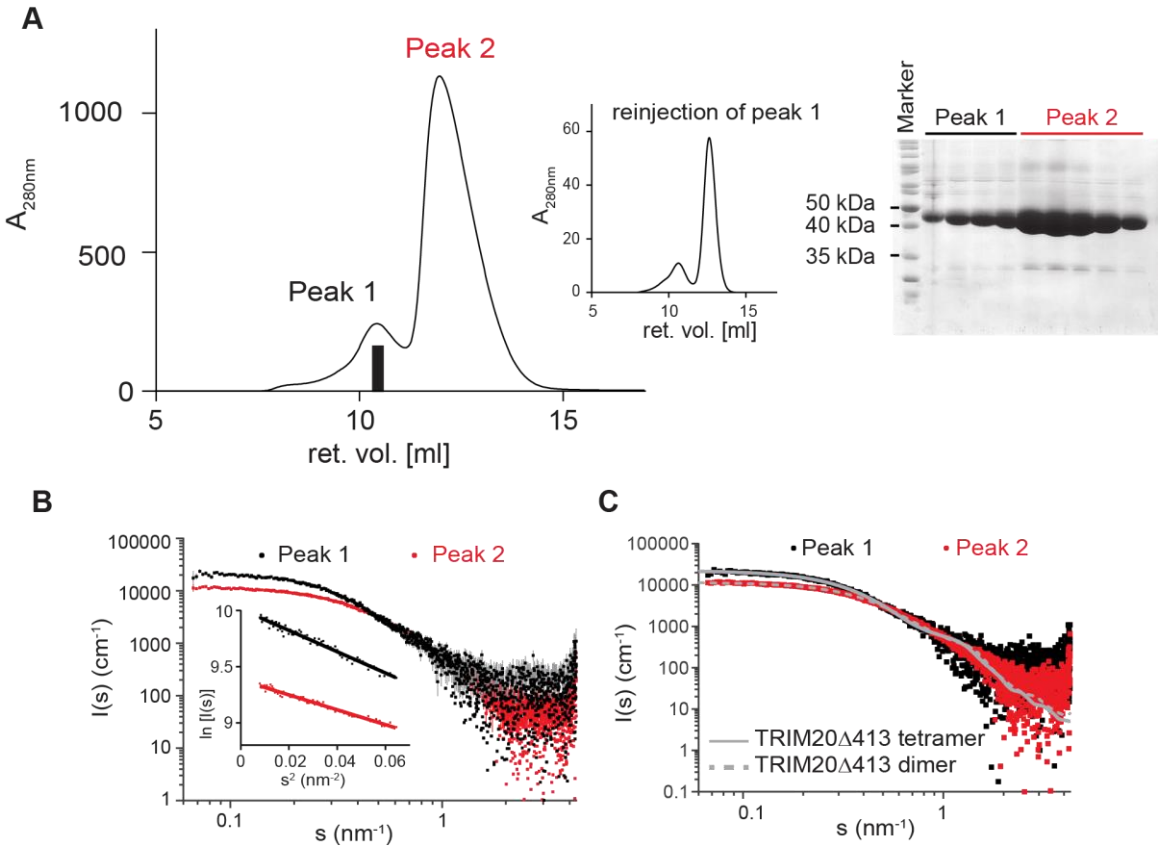

D

	TRIM5αΔ132		TRIM20Δ413		
	Peak 1	Peak 2	Tetramer (X-ray)	Dimer (SAXS)[3]	Dimer (X-ray)
Retention volume [ml]	10.4	12	-	-	-
R_G [nm]	5.3±0.24[1]	4.5±0.07[1]	5.4[2]	4.27	4.29[2]
D_{max} [nm]	18.5[1]	15.5[1]	20.1[2]	15.9	17.3[2]
Experimental MW [kDa]	159.5[1]	84.3[1]	-	90	-
Theoretical MW [kDa]	169.2[4]	84.6[4]	170.9[5]	85.5[5]	85.5[5]

Figure S4

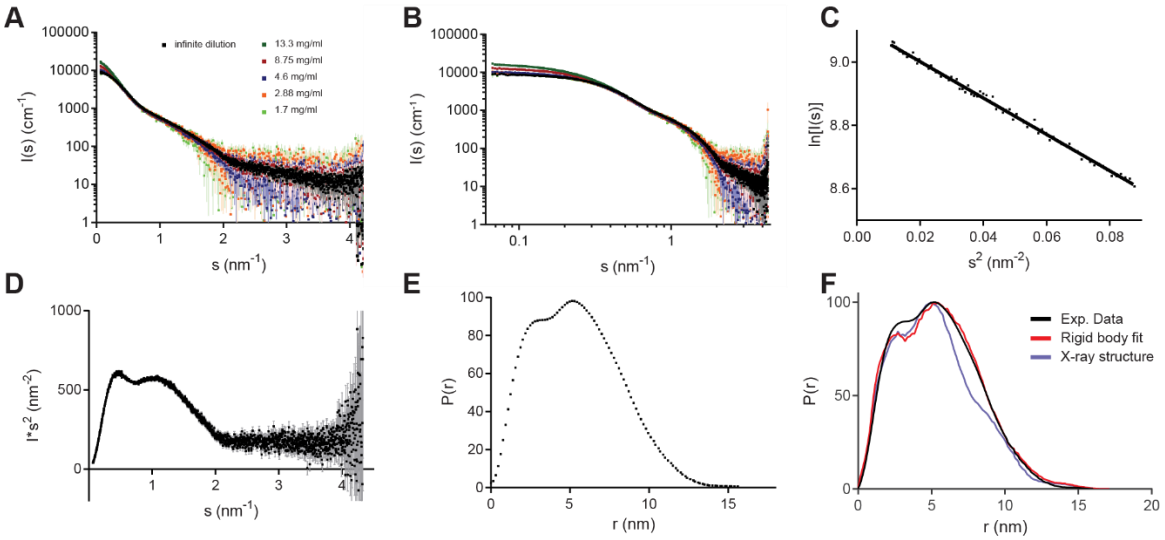

Figure S5

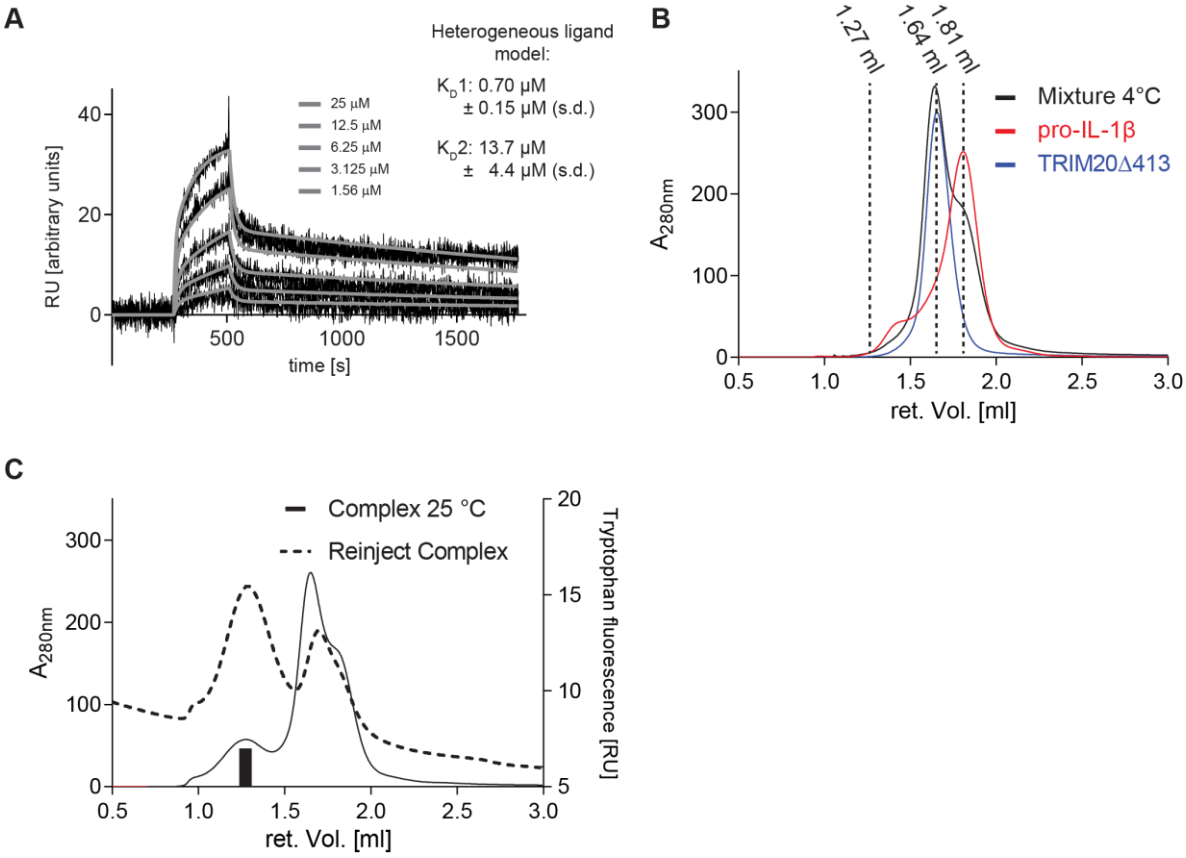

Figure S6

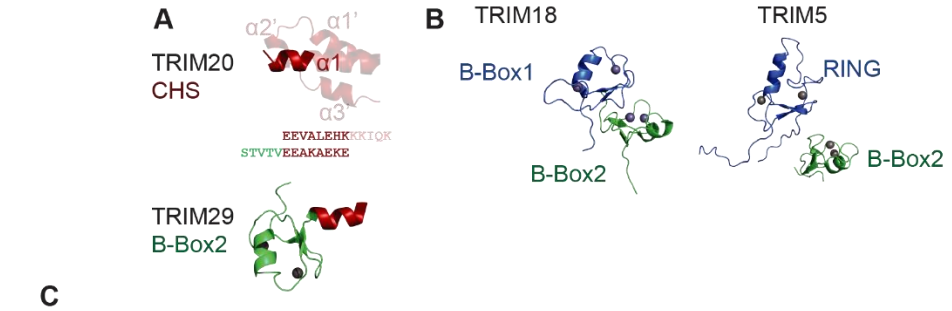

C

```
TRIM5_RING        8  MASGILVNVK EEVTCPICL- --ELLTQPLS LDCGHSFCQA CLTANHKKSM   54
TRIM5_BBox        0  ---------- ---------- ---------- ---------- ----------     0
TRIM29_BBox       0  ---------- ---------- ---------- ---------- ----------     0
TRIM18_tandem   114  ---------A EKVLCQFCDQ DPAQDAVKTC VTCEVSYCDE CLKATHP---   151
Target_seq.       1  MASGILVNVK EEVTCPICL- --ELLTQPLS LDCGHSFCQA CLTANHKKSM    47

TRIM5_RING       55  LDKGESSCPV CRISY----- ---------- ---------- ----------    69
TRIM5_BBox        8  ---------- ---------- ---------- --------SP EGQKVDHCAR    19
TRIM29_BBox      16  ---------- ---------- ---------- ---------- --FEARKCPV    23
TRIM18_tandem   152  ---------- -----NKKPF TGHRLIEPIP ----DSHI-- ---RGLMCLE   177
Target_seq.      48  LDKGESSCPV CRISYQPENI RPNRHVANIV EKLREVKLSP EGQKVDHCAR    97

TRIM5_RING       69  ---------- ---------- ---------- ---------- --zz--      71
TRIM5_BBox       20  HG-EKLLLFC QEDGKVICWL CERSQEHRGH HTF------- --zz--      53
TRIM29_BBox      24  HG-KTMELFC QTDQTCICYL CMFQ-EHKNH STVTVEEAKA EKzz--      65
TRIM18_tandem   178  HEDEKVNMYC VTDDQLICAL CKLVGRHRDH QVAALSE--- --zzzz     218
Target_seq.      98  HG-EKLLLFC QEDGKVICWL CERSQEHRGH HTFLTEEVAL EHzzzz     142
```

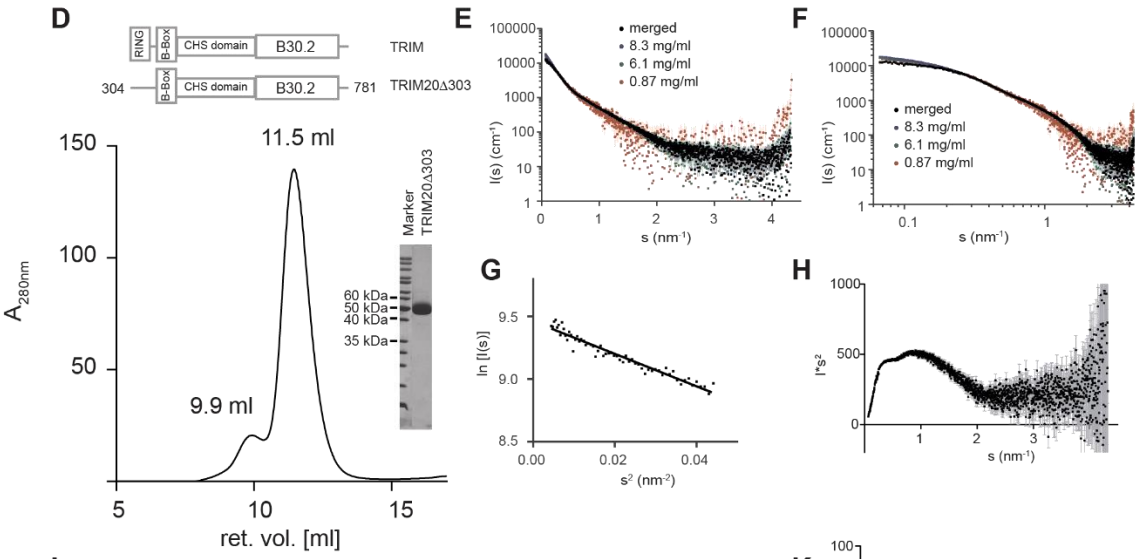

I

	TRIM20Δ303	Model full length TRIM
R_G [nm]	6.15±0.02	6.24[3]
D_{max} [nm]	20.67	21.1[3]
I(0)	12300	-
Experimental MW [kDa]	114.5[1]	-
Theoretical MW [kDa]	109.3[2]	113.5[2]

Supplementary Tables

Table S1. X-ray data collection and refinement statistics

	TRIM20Δ413
Data collection	
Space group	$P2_1$
Cell dimensions	
a, *b*, *c* (Å)	69.82 388.21 70.88
α, β, γ (°)	90 116.52 90
Resolution (Å)	48.53 - 2.4 (2.486 - 2.4)*
R_{merge}	0.1724 (1.857)*
$I / \sigma I$	9.77 (0.88)*
Completeness (%)	98.96 (93.07)*
Redundancy	7.4 (6.6)*
$CC_{1/2}$	99.6 (51.3)*
Refinement	
Resolution (Å)	48.53 – 2.4
No. reflections	129414
R_{work} / R_{free} (%)	21.15 / 26.07
No. atoms	
Protein	17943
Ligand/ion	68
Water	33
B-factors	
Protein	54.8
Ligand/ion	67.7
Water	33.6
R.m.s. deviations	
Bond lengths (Å)	0.012
Bond angles (°)	1.37

The dataset was recorded from a single crystal.
*Values in parentheses are for highest-resolution shell.

Table S2: SAXS data collection and processing

	TRIM20Δ413
Data collection	
Instrument	Petra 12; Pilatus 2M
Beam geometry	0.2x0.12 mm2
Wavelength (Å)	1.24
s range (nm^{-1})	0.0668-4.336
Exposure time (s)	0.05
Concentration range [mg/ml]	1.7-13.3
Temperature	283
Structural parameters	
I(0) (cm^{-1}) [from P(r)]	9184 (± 8.47)
Rg (nm) [from P(r)]	4.27 (± 0.056)
I(0) (cm^{-1}) (from guinier)	9100.84 (±20.24)
Rg (nm) (from guinier)	4.15 (± 0.023)
Dmax [nm]	15.9
Porod volume estimate ($Å^3$)	131.72
Dry volume calculated from structure ($Å^3$)	100.5
Molecular mass determination	
Partial specific volume (cm^3g^{-1})	1.37
Molecular mass Mr [kDa]	90.0
Molecular mass Mr [kDa; analytical ultracentrifugation]	78.4
Monomeric Mr from MS analysis [kDa]	42.737
Software employed	
Primary data reduction	*PRIMUS*
Data processing	*PRIMUS / GNOM*
Extrapolation to infinite dilution	*ALMERGE*
Ab initio analysis	*DAMMIN*
Validation and averaging	*DAMAVER*
Rigid-body modelling	*SASREF*
Multiple conformation modelling	*EOM*
Computation of model intensities	*CRYSOL*
3D graphics representation R.m.s. deviations	*PyMOL*

Table S3. Kinetic data of SPR experiment

k_{on}1 [1/Ms]	k_{off} 1 [1/s]	K_D1 [µM]	R_{max}1 [RU]
$4.17*10^2$ $\pm1.4*10^2$	$2.83*10^{-4}$ $\pm0.59*10^{-4}$	0.70 ± 0.15	20.3 ± 3.88

k_{on}2 [1/Ms]	k_{off} 2 [1/s]	K_D2 [µM]	R_{max}2 [RU]	χ^2 [RU]
$3.96*10^3$ $\pm1.32*10^3$	$5.10*10^{-2}$ $\pm1.38*10^{-2}$	13.7 ± 4.4	25 ± 3.27	2.55 ±0.54

Table S4. Construct design

Construct	Coding region	Tag	Forward primer	Reverse primer	Template vector
TRIM20Δ413	414-781	-	atatatgctcttctagtgaggtcgccctggaac	tatatagctcttcttgcgtcaggcccctgacc	pFX3CH
TRIM20Δ412	413-781	N-terminal c-Myc (EQGKLISEEDL)	atatatgctcttctagtgagcagaaactcatctctgaagaggatctggaggaggttgccc	tatatagctcttcttgcgtcaggcccctgacc	pFX3CH
TRIM20-CHS	413-577	N-terminal c-Myc (EQGKLISEEDL)	atatatgctcttctagtgagcagaaactcatctctgaagaggatctggaggaggttgccc	tatatagctcttcatgcggtttctgagaagtac	pFX3CH
TRIM20-B30.2	577-781	C-terminal c-Myc (EQGKLISEEDL)	atatatgctcttctagtctgcgttcagaaatgg	tatatagctcttcatgccagatcctcttcagagatgagtttctgctcgtcaggcccctgacc	pFX3CH
TRIM20Δ303	304-781	-	atatatgctcttctagtggaaggccaccagac	tatatagctcttcttgcgtcaggcccctgacc	pFX3CH
TRIM5αΔ132	133-493	-	atatatgctcttctagtgattacaaagacgatgacgataaagaggttgcccgg	tatatagctcttcatgcagagcttggtgagc	pFX3CH
Pro-IL-1β	Full length	C-terminal FLAG (DYKDDDDK)	atatatgctcttctagtgcggaagtgccggaac	tatatagctcttcatgccttatcgtcgtcatccttgaatcgctgctcacaaactgc	pET28-FXH3C

5 Final Discussion and Outlook

The emphasis of this thesis was to elucidate three main subjects: i) The structural characterization of pyrin fragments with a focus on the C-terminal B30.2 domain, ii) effects of FMF associated mutations located in the putative binding epitope of the B30.2 domain, iii) and the biochemical analysis of ligand binding to pyrin.

At the beginning of this thesis, no *in-vitro* information was available for pyrin. Establishing protocols for the expression and purification of pyrin fragments allowed us to structurally and functionally characterize the protein.

The structure of a C-terminal fragment of pyrin revealed the antiparallel dimerization mediated by the central helical scaffold domain and the arrangement of the single domains. This information was used to construct a stereotype full length TRIM protein that provides yet unknown insights into the architecture of this important class of proteins. Additionally, the presented tetramer provides further information on the contribution of the single domains to the TRIM self-assembly. The work on the isolated B30.2 domain revealed the structural changes induced by FMF associated mutations in the putative binding epitope that show both local effects on the shape of the epitope and but also on the conformational flexibility of entire loops. This sheds light into specific characteristics of the binding epitope of the pyrin B30.2 domain.

As the function of pyrin has exclusively been studied *in-vivo*, there is a lack of biochemical data on interaction of pyrin to putative ligands. We established protocols for the *in-vitro* characterization of the interaction to pro-IL-1β and suggest a tight binding between these proteins, when pyrin is present as a tetramer.

In summary, the thesis sets the basis for further *in-vitro* characterization of the protein pyrin. There are 4 major questions to be answered. 1) Is pyrin inhibiting the maturation of pro-IL-1β *in-vitro*? 2) Is the binding of pyrin to pro-IL-1β solely mediated by the tetramer? 3) Do FMF associated mutations alter the thermodynamics of tetramerization or the binding affinity to pro-IL-1β? 4) What is the binding interface between pyrin and pro-IL-1β?

These questions should further reveal the exact mechanism on how pyrin functions both in an anti- as well as pro-inflammatory manner, thereby elucidating the effects induced by FMF mutations.

6 References

1. Newton, K. & Dixit, V.M. Signaling in innate immunity and inflammation. *Cold Spring Harbor perspectives in biology* **4**(2012).
2. Murphy, K.T.P.W.M.J.C. *Janeway's immunobiology*, (Garland Science, New York, 2012).
3. Botos, I., Segal, D.M. & Davies, D.R. The structural biology of Toll-like receptors. *Structure* **19**, 447-59 (2011).
4. Jin, M.S. et al. Crystal structure of the TLR1-TLR2 heterodimer induced by binding of a tri-acylated lipopeptide. *Cell* **130**, 1071-82 (2007).
5. Park, B.S. et al. The structural basis of lipopolysaccharide recognition by the TLR4-MD-2 complex. *Nature* **458**, 1191-5 (2009).
6. Tanji, H., Ohto, U., Shibata, T., Miyake, K. & Shimizu, T. Structural reorganization of the Toll-like receptor 8 dimer induced by agonistic ligands. *Science* **339**, 1426-9 (2013).
7. Arthur, J.S. & Ley, S.C. Mitogen-activated protein kinases in innate immunity. *Nature reviews. Immunology* **13**, 679-92 (2013).
8. Besse, A. et al. TAK1-dependent signaling requires functional interaction with TAB2/TAB3. *The Journal of biological chemistry* **282**, 3918-28 (2007).
9. Kanayama, A. et al. TAB2 and TAB3 activate the NF-kappaB pathway through binding to polyubiquitin chains. *Molecular cell* **15**, 535-48 (2004).
10. Hardison, S.E. & Brown, G.D. C-type lectin receptors orchestrate antifungal immunity. *Nature immunology* **13**, 817-22 (2012).
11. Zeng, W. et al. Reconstitution of the RIG-I pathway reveals a signaling role of unanchored polyubiquitin chains in innate immunity. *Cell* **141**, 315-30 (2010).
12. Feng, M. et al. Structural and biochemical studies of RIG-I antiviral signaling. *Protein & cell* **4**, 142-54 (2013).
13. Monie, T.P. NLR activation takes a direct route. *Trends in biochemical sciences* **38**, 131-9 (2013).
14. Ishii, K.J., Koyama, S., Nakagawa, A., Coban, C. & Akira, S. Host innate immune receptors and beyond: making sense of microbial infections. *Cell host & microbe* **3**, 352-63 (2008).
15. Kersse, K., Verspurten, J., Vanden Berghe, T. & Vandenabeele, P. The death-fold superfamily of homotypic interaction motifs. *Trends in biochemical sciences* **36**, 541-52 (2011).
16. Halff, E.F. et al. Formation and structure of a NAIP5-NLRC4 inflammasome induced by direct interactions with conserved N- and C-terminal regions of flagellin. *The Journal of biological chemistry* **287**, 38460-72 (2012).
17. Faustin, B. et al. Reconstituted NALP1 inflammasome reveals two-step mechanism of caspase-1 activation. *Molecular cell* **25**, 713-24 (2007).
18. Hu, Z. et al. Crystal structure of NLRC4 reveals its autoinhibition mechanism. *Science* **341**, 172-5 (2013).
19. Zhao, Y. et al. The NLRC4 inflammasome receptors for bacterial flagellin and type III secretion apparatus. *Nature* **477**, 596-600 (2011).
20. Agostini, L. et al. NALP3 forms an IL-1beta-processing inflammasome with increased activity in Muckle-Wells autoinflammatory disorder. *Immunity* **20**, 319-25 (2004).

21. Roschitzki-Voser, H. et al. Human caspases in vitro: expression, purification and kinetic characterization. *Protein expression and purification* **84**, 236-46 (2012).
22. Howard, A.D. et al. IL-1-converting enzyme requires aspartic acid residues for processing of the IL-1 beta precursor at two distinct sites and does not cleave 31-kDa IL-1 alpha. *Journal of immunology* **147**, 2964-9 (1991).
23. Swaan, P.W., Knoell, D.L., Helsper, F. & Wewers, M.D. Sequential processing of human ProIL-1beta by caspase-1 and subsequent folding determined by a combined in vitro and in silico approach. *Pharmaceutical research* **18**, 1083-90 (2001).
24. Eder, C. Mechanisms of interleukin-1beta release. *Immunobiology* **214**, 543-53 (2009).
25. Dinarello, C.A. Biologic basis for interleukin-1 in disease. *Blood* **87**, 2095-147 (1996).
26. Dinarello, C.A. Interleukin-1 in the pathogenesis and treatment of inflammatory diseases. *Blood* **117**, 3720-32 (2011).
27. Shinkai, K., McCalmont, T.H. & Leslie, K.S. Cryopyrin-associated periodic syndromes and autoinflammation. *Clinical and experimental dermatology* **33**, 1-9 (2008).
28. Galeazzi, M. et al. Autoinflammatory syndromes. *Clinical and experimental rheumatology* **24**, S79-85 (2006).
29. Daniels, M., Shohat, T., Brenner-Ullman, A. & Shohat, M. Familial Mediterranean fever: high gene frequency among the non-Ashkenazic and Ashkenazic Jewish populations in Israel. *American journal of medical genetics* **55**, 311-4 (1995).
30. Grateau, G. et al. Clinical versus genetic diagnosis of familial Mediterranean fever. *QJM : monthly journal of the Association of Physicians* **93**, 223-9 (2000).
31. Shohat, M. & Halpern, G.J. Familial Mediterranean fever--a review. *Genetics in medicine : official journal of the American College of Medical Genetics* **13**, 487-98 (2011).
32. Soriano, A. & Manna, R. Familial Mediterranean fever: new phenotypes. *Autoimmunity reviews* **12**, 31-7 (2012).
33. Karadag, O. et al. The factors considered as trigger for the attacks in patients with familial Mediterranean fever. *Rheumatology international* (2012).
34. Livneh, A. et al. Criteria for the diagnosis of familial Mediterranean fever. *Arthritis and rheumatism* **40**, 1879-85 (1997).
35. Goldfinger, S.E. Colchicine for familial Mediterranean fever. *The New England journal of medicine* **287**, 1302 (1972).
36. Roldan, R., Ruiz, A.M., Miranda, M.D. & Collantes, E. Anakinra: new therapeutic approach in children with Familial Mediterranean Fever resistant to colchicine. *Joint, bone, spine : revue du rhumatisme* **75**, 504-5 (2008).
37. A candidate gene for familial Mediterranean fever. *Nature genetics* **17**, 25-31 (1997).
38. Ancient missense mutations in a new member of the RoRet gene family are likely to cause familial Mediterranean fever. The International FMF Consortium. *Cell* **90**, 797-807 (1997).

39. Kastner, P. et al. Structure, localization and transcriptional properties of two classes of retinoic acid receptor alpha fusion proteins in acute promyelocytic leukemia (APL): structural similarities with a new family of oncoproteins. *The EMBO journal* **11**, 629-42 (1992).
40. Reddy, B.A., Etkin, L.D. & Freemont, P.S. A novel zinc finger coiled-coil domain in a family of nuclear proteins. *Trends in biochemical sciences* **17**, 344-5 (1992).
41. Ashwell, J.D. The many paths to p38 mitogen-activated protein kinase activation in the immune system. *Nature reviews. Immunology* **6**, 532-40 (2006).
42. Ozato, K., Shin, D.M., Chang, T.H. & Morse, H.C., 3rd. TRIM family proteins and their emerging roles in innate immunity. *Nature reviews. Immunology* **8**, 849-60 (2008).
43. Kawai, T. & Akira, S. Regulation of innate immune signalling pathways by the tripartite motif (TRIM) family proteins. *EMBO molecular medicine* **3**, 513-27 (2011).
44. Short, K.M. & Cox, T.C. Subclassification of the RBCC/TRIM superfamily reveals a novel motif necessary for microtubule binding. *The Journal of biological chemistry* **281**, 8970-80 (2006).
45. Deshaies, R.J. & Joazeiro, C.A. RING domain E3 ubiquitin ligases. *Annual review of biochemistry* **78**, 399-434 (2009).
46. Budhidarmo, R., Nakatani, Y. & Day, C.L. RINGs hold the key to ubiquitin transfer. *Trends in biochemical sciences* **37**, 58-65 (2012).
47. Borden, K.L. et al. The solution structure of the RING finger domain from the acute promyelocytic leukaemia proto-oncoprotein PML. *The EMBO journal* **14**, 1532-41 (1995).
48. Barlow, P.N., Luisi, B., Milner, A., Elliott, M. & Everett, R. Structure of the C3HC4 domain by 1H-nuclear magnetic resonance spectroscopy. A new structural class of zinc-finger. *Journal of molecular biology* **237**, 201-11 (1994).
49. Lorick, K.L. et al. RING fingers mediate ubiquitin-conjugating enzyme (E2)-dependent ubiquitination. *Proceedings of the National Academy of Sciences of the United States of America* **96**, 11364-9 (1999).
50. Li, W. et al. Genome-wide and functional annotation of human E3 ubiquitin ligases identifies MULAN, a mitochondrial E3 that regulates the organelle's dynamics and signaling. *PloS one* **3**, e1487 (2008).
51. Trockenbacher, A. et al. MID1, mutated in Opitz syndrome, encodes an ubiquitin ligase that targets phosphatase 2A for degradation. *Nature genetics* **29**, 287-94 (2001).
52. Liu, J., Prickett, T.D., Elliott, E., Meroni, G. & Brautigan, D.L. Phosphorylation and microtubule association of the Opitz syndrome protein mid-1 is regulated by protein phosphatase 2A via binding to the regulatory subunit alpha 4. *Proceedings of the National Academy of Sciences of the United States of America* **98**, 6650-5 (2001).
53. Urano, T. et al. Efp targets 14-3-3 sigma for proteolysis and promotes breast tumour growth. *Nature* **417**, 871-5 (2002).
54. Pickart, C.M. Targeting of substrates to the 26S proteasome. *FASEB journal : official publication of the Federation of American Societies for Experimental Biology* **11**, 1055-66 (1997).

55. Xia, Z.P. et al. Direct activation of protein kinases by unanchored polyubiquitin chains. *Nature* **461**, 114-9 (2009).
56. McEwan, W.A. et al. Intracellular antibody-bound pathogens stimulate immune signaling via the Fc receptor TRIM21. *Nature immunology* **14**, 327-36 (2013).
57. Pertel, T. et al. TRIM5 is an innate immune sensor for the retrovirus capsid lattice. *Nature* **472**, 361-5 (2011).
58. Zurek, B. et al. TRIM27 negatively regulates NOD2 by ubiquitination and proteasomal degradation. *PloS one* **7**, e41255 (2012).
59. Mrosek, M. et al. Structural analysis of B-Box 2 from MuRF1: identification of a novel self-association pattern in a RING-like fold. *Biochemistry* **47**, 10722-30 (2008).
60. Massiah, M.A., Simmons, B.N., Short, K.M. & Cox, T.C. Solution structure of the RBCC/TRIM B-box1 domain of human MID1: B-box with a RING. *Journal of molecular biology* **358**, 532-45 (2006).
61. Massiah, M.A. et al. Solution structure of the MID1 B-box2 CHC(D/C)C(2)H(2) zinc-binding domain: insights into an evolutionarily conserved RING fold. *Journal of molecular biology* **369**, 1-10 (2007).
62. Diaz-Griffero, F. et al. A B-box 2 surface patch important for TRIM5alpha self-association, capsid binding avidity, and retrovirus restriction. *Journal of virology* **83**, 10737-51 (2009).
63. Tao, H. et al. Structure of the MID1 tandem B-boxes reveals an interaction reminiscent of intermolecular ring heterodimers. *Biochemistry* **47**, 2450-7 (2008).
64. Bell, J.L. et al. TRIM16 Acts as an E3 Ubiquitin Ligase and Can Heterodimerize with Other TRIM Family Members. *PloS one* **7**, e37470 (2012).
65. Crick, F.H. Is alpha-keratin a coiled coil? *Nature* **170**, 882-3 (1952).
66. Adamson, J.G., Zhou, N.E. & Hodges, R.S. Structure, function and application of the coiled-coil protein folding motif. *Current opinion in biotechnology* **4**, 428-37 (1993).
67. Lupas, A.N. & Gruber, M. The structure of alpha-helical coiled coils. *Advances in protein chemistry* **70**, 37-78 (2005).
68. Harbury, P.B., Zhang, T., Kim, P.S. & Alber, T. A switch between two-, three-, and four-stranded coiled coils in GCN4 leucine zipper mutants. *Science* **262**, 1401-7 (1993).
69. Mason, J.M. & Arndt, K.M. Coiled coil domains: stability, specificity, and biological implications. *Chembiochem : a European journal of chemical biology* **5**, 170-6 (2004).
70. Sardiello, M., Cairo, S., Fontanella, B., Ballabio, A. & Meroni, G. Genomic analysis of the TRIM family reveals two groups of genes with distinct evolutionary properties. *BMC evolutionary biology* **8**, 225 (2008).
71. Reymond, A. et al. The tripartite motif family identifies cell compartments. *The EMBO journal* **20**, 2140-51 (2001).
72. Mische, C.C. et al. Retroviral restriction factor TRIM5alpha is a trimer. *Journal of virology* **79**, 14446-50 (2005).
73. Rhodes, D.A. & Trowsdale, J. TRIM21 is a trimeric protein that binds IgG Fc via the B30.2 domain. *Molecular immunology* **44**, 2406-14 (2007).

74. Langelier, C.R. et al. Biochemical characterization of a recombinant TRIM5alpha protein that restricts human immunodeficiency virus type 1 replication. *Journal of virology* **82**, 11682-94 (2008).
75. Mallery, D.L. et al. Antibodies mediate intracellular immunity through tripartite motif-containing 21 (TRIM21). *Proceedings of the National Academy of Sciences of the United States of America* **107**, 19985-90 (2010).
76. Javanbakht, H. et al. Characterization of TRIM5alpha trimerization and its contribution to human immunodeficiency virus capsid binding. *Virology* **353**, 234-46 (2006).
77. Harbers, M., Nomura, T., Ohno, S. & Ishii, S. Intracellular localization of the Ret finger protein depends on a functional nuclear export signal and protein kinase C activation. *The Journal of biological chemistry* **276**, 48596-607 (2001).
78. Espinosa, A. et al. The autoantigen Ro52 is an E3 ligase resident in the cytoplasm but enters the nucleus upon cellular exposure to nitric oxide. *Experimental cell research* **314**, 3605-13 (2008).
79. Main, A.L., Harvey, T.S., Baron, M., Boyd, J. & Campbell, I.D. The three-dimensional structure of the tenth type III module of fibronectin: an insight into RGD-mediated interactions. *Cell* **71**, 671-8 (1992).
80. Pascual, J., Martinez-Yamout, M., Dyson, H.J. & Wright, P.E. Structure of the PHD zinc finger from human Williams-Beuren syndrome transcription factor. *Journal of molecular biology* **304**, 723-9 (2000).
81. Filippakopoulos, P. et al. Histone recognition and large-scale structural analysis of the human bromodomain family. *Cell* **149**, 214-31 (2012).
82. Schultz, D.C., Friedman, J.R. & Rauscher, F.J., 3rd. Targeting histone deacetylase complexes via KRAB-zinc finger proteins: the PHD and bromodomains of KAP-1 form a cooperative unit that recruits a novel isoform of the Mi-2alpha subunit of NuRD. *Genes & development* **15**, 428-43 (2001).
83. Slack, F.J. & Ruvkun, G. A novel repeat domain that is often associated with RING finger and B-box motifs. *Trends in biochemical sciences* **23**, 474-5 (1998).
84. Edwards, T.A., Wilkinson, B.D., Wharton, R.P. & Aggarwal, A.K. Model of the brain tumor-Pumilio translation repressor complex. *Genes & development* **17**, 2508-13 (2003).
85. Ye, H. et al. Distinct molecular mechanism for initiating TRAF6 signalling. *Nature* **418**, 443-7 (2002).
86. Vernet, C. et al. Evolutionary study of multigenic families mapping close to the human MHC class I region. *Journal of molecular evolution* **37**, 600-12 (1993).
87. Henry, J., Mather, I.H., McDermott, M.F. & Pontarotti, P. B30.2-like domain proteins: update and new insights into a rapidly expanding family of proteins. *Molecular biology and evolution* **15**, 1696-705 (1998).
88. Ponting, C., Schultz, J. & Bork, P. SPRY domains in ryanodine receptors (Ca(2+)-release channels). *Trends in biochemical sciences* **22**, 193-4 (1997).
89. Woo, J.S., Suh, H.Y., Park, S.Y. & Oh, B.H. Structural basis for protein recognition by B30.2/SPRY domains. *Molecular cell* **24**, 967-76 (2006).

90. Hilton, D.J. et al. Twenty proteins containing a C-terminal SOCS box form five structural classes. *Proceedings of the National Academy of Sciences of the United States of America* **95**, 114-9 (1998).
91. Grutter, C. et al. Structure of the PRYSPRY-domain: implications for autoinflammatory diseases. *FEBS letters* **580**, 99-106 (2006).
92. Rhodes, D.A., de Bono, B. & Trowsdale, J. Relationship between SPRY and B30.2 protein domains. Evolution of a component of immune defence? *Immunology* **116**, 411-7 (2005).
93. Kuang, Z. et al. SPRY domain-containing SOCS box protein 2: crystal structure and residues critical for protein binding. *Journal of molecular biology* **386**, 662-74 (2009).
94. James, L.C., Keeble, A.H., Khan, Z., Rhodes, D.A. & Trowsdale, J. Structural basis for PRYSPRY-mediated tripartite motif (TRIM) protein function. *Proceedings of the National Academy of Sciences of the United States of America* **104**, 6200-5 (2007).
95. Papin, S. et al. The SPRY domain of Pyrin, mutated in familial Mediterranean fever patients, interacts with inflammasome components and inhibits proIL-1beta processing. *Cell death and differentiation* **14**, 1457-66 (2007).
96. Meroni, G. & Diez-Roux, G. TRIM/RBCC, a novel class of 'single protein RING finger' E3 ubiquitin ligases. *BioEssays : news and reviews in molecular, cellular and developmental biology* **27**, 1147-57 (2005).
97. Ganser-Pornillos, B.K. et al. Hexagonal assembly of a restricting TRIM5alpha protein. *Proceedings of the National Academy of Sciences of the United States of America* **108**, 534-9 (2011).
98. Chae, J.J., Aksentijevich, I. & Kastner, D.L. Advances in the understanding of familial Mediterranean fever and possibilities for targeted therapy. *British journal of haematology* **146**, 467-78 (2009).
99. Martinon, F., Hofmann, K. & Tschopp, J. The pyrin domain: a possible member of the death domain-fold family implicated in apoptosis and inflammation. *Current biology : CB* **11**, R118-20 (2001).
100. Jeru, I. et al. Interaction of pyrin with 14.3.3 in an isoform-specific and phosphorylation-dependent manner regulates its translocation to the nucleus. *Arthritis and rheumatism* **52**, 1848-57 (2005).
101. Centola, M. et al. The gene for familial Mediterranean fever, MEFV, is expressed in early leukocyte development and is regulated in response to inflammatory mediators. *Blood* **95**, 3223-31 (2000).
102. Carthagena, L. et al. Human TRIM gene expression in response to interferons. *PloS one* **4**, e4894 (2009).
103. Grandemange, S., Aksentijevich, I., Jeru, I., Gul, A. & Touitou, I. The regulation of MEFV expression and its role in health and familial Mediterranean fever. *Genes and immunity* **12**, 497-503 (2011).
104. Richards, N. et al. Interaction between pyrin and the apoptotic speck protein (ASC) modulates ASC-induced apoptosis. *The Journal of biological chemistry* **276**, 39320-9 (2001).
105. Dowds, T.A. et al. Regulation of cryopyrin/Pypaf1 signaling by pyrin, the familial Mediterranean fever gene product. *Biochemical and biophysical research communications* **302**, 575-80 (2003).

106. Yu, J.W. et al. Cryopyrin and pyrin activate caspase-1, but not NF-kappaB, via ASC oligomerization. *Cell death and differentiation* **13**, 236-49 (2006).
107. Waite, A.L. et al. Pyrin Modulates the Intracellular Distribution of PSTPIP1. *PloS one* **4**, e6147 (2009).
108. Shoham, N.G. et al. Pyrin binds the PSTPIP1/CD2BP1 protein, defining familial Mediterranean fever and PAPA syndrome as disorders in the same pathway. *Proceedings of the National Academy of Sciences of the United States of America* **100**, 13501-6 (2003).
109. Yu, J.W. et al. Pyrin activates the ASC pyroptosome in response to engagement by autoinflammatory PSTPIP1 mutants. *Molecular cell* **28**, 214-27 (2007).
110. Gavrilin, M.A. et al. Activation of the pyrin inflammasome by intracellular Burkholderia cenocepacia. *Journal of immunology* **188**, 3469-77 (2012).
111. Laskin, J.D., Heck, D.E. & Laskin, D.L. The ribotoxic stress response as a potential mechanism for MAP kinase activation in xenobiotic toxicity. *Toxicological sciences : an official journal of the Society of Toxicology* **69**, 289-91 (2002).
112. Yu, J.W., Farias, A., Hwang, I., Fernandes-Alnemri, T. & Alnemri, E.S. Ribotoxic Stress through p38 Mitogen-activated Protein Kinase Activates in Vitro the Human Pyrin Inflammasome. *The Journal of biological chemistry* **288**, 11378-83 (2013).
113. Chae, J.J. et al. The familial Mediterranean fever protein, pyrin, is cleaved by caspase-1 and activates NF-kappaB through its N-terminal fragment. *Blood* **112**, 1794-803 (2008).
114. Chae, J.J. et al. The B30.2 domain of pyrin, the familial Mediterranean fever protein, interacts directly with caspase-1 to modulate IL-1beta production. *Proceedings of the National Academy of Sciences of the United States of America* **103**, 9982-7 (2006).
115. Milhavet, F. et al. The infevers autoinflammatory mutation online registry: update with new genes and functions. *Human mutation* **29**, 803-8 (2008).
116. el-Garf, A., Salah, S., Iskander, I., Salah, H. & Amin, S.N. MEFV mutations in Egyptian patients suffering from familial Mediterranean fever: analysis of 12 gene mutations. *Rheumatology international* **30**, 1293-8 (2010).
117. Ait-Idir, D., Khilan, A., Djerdjouri, B. & El-Shanti, H. Spectrum of mutations and carrier frequency of familial Mediterranean fever gene in the Algerian population. *Rheumatology* **50**, 2306-10 (2011).
118. Akar, N. et al. MEFV mutations in Turkish patients suffering from Familial Mediterranean Fever. *Human mutation* **15**, 118-9 (2000).
119. Albayrak, F., Selcuk, N.Y., Odabas, A.R., Cetinkaya, R. & Pirim, I. Genotype-phenotype correlation in patients with familial Mediterranean fever in East Anatolia (Turkey). *Genetic testing and molecular biomarkers* **14**, 325-8 (2010).
120. Ayesh, S.K., Nassar, S.M., Al-Sharef, W.A., Abu-Libdeh, B.Y. & Darwish, H.M. Genetic screening of familial Mediterranean fever mutations in the Palestinian population. *Saudi medical journal* **26**, 732-7 (2005).
121. Chaabouni, H.B. et al. MEFV mutations in Tunisian patients suffering from familial Mediterranean fever. *Seminars in arthritis and rheumatism* **36**, 397-401 (2007).

122. Dundar, M. et al. A molecular analysis of familial Mediterranean fever disease in a cohort of Turkish patients. *Annals of Saudi medicine* **32**, 343-8 (2012).
123. El Gezery, D.A., Abou-Zeid, A.A., Hashad, D.I. & El-Sayegh, H.K. MEFV gene mutations in Egyptian patients with familial Mediterranean fever. *Genetic testing and molecular biomarkers* **14**, 263-8 (2010).
124. Ben-Chetrit, E. Familial Mediterranean fever (FMF) and renal AA amyloidosis--phenotype-genotype correlation, treatment and prognosis. *Journal of nephrology* **16**, 431-4 (2003).
125. Akpolat, T., Ozkaya, O. & Ozen, S. Homozygous M694V as a risk factor for amyloidosis in Turkish FMF patients. *Gene* **492**, 285-9 (2012).
126. Goulielmos, G.N. et al. Mutational analysis of the PRYSPRY domain of pyrin and implications for familial mediterranean fever (FMF). *Biochemical and biophysical research communications* **345**, 1326-32 (2006).

Appendix A

Curriculum Vitae:

Christopher Weinert, M.sc. Biochemistry UZH

Date of Birth: 9 December 1981

Place of Birth: Dresden, Germany

Nationality: German

EDUCATION

1998 - 1999	1996 - 2001 Kantonschule am Burggraben St. Gallen, Switzerland; Wirtschafts-Matura
2002 - 2005:	Bachelor of Science UZH in Biochemistry, University of Zurich, Switzerland Title of Bachelor work: “Essay development for mice genotyping using RT-PCR”
2005 - 2007	Master of Science UZH in Biochemistry, University of Zurich, Switzerland Title of Master thesis: “Structure determination and binding studies of the PRYSPRY domain of human pyrin”, under the supervision of Prof. Dr. M. G. Grütter
2008 to present	PhD thesis at the University of Zurich and Ph.D. Program in Biomolecular Structure and Mechanism under the supervision of Prof. M.G. Grütter

Meeting contribution and courses

2011	Postgraduate Course – ETH, Zurich, Switzerland: Title: 9th NCCR Practical Course, Reaction Kinetics of Biological Macromolecules
2009	Postgraduate Course within the Ph.D. program Biomolecular Structure and Mechanism – Title: “Intensive course in structural biology, biophysics and biochemistry”
2009	Poster Presentation – VIII European Symposium of The Protein Society, Zurich, Switzerland; Title: „Structure analysis of the PrySpry Domain of Human Pyrin”
2007	Talk – 21st Rhine-Knee Regional Meeting, Leuenberg, Switzerland; Title: “Structure of the PrySpry Domain of Human Pyrin”

Publication

2009	Weinert C., Grütter C., Roschitzki-Voser H., Mittl P.R., Grütter M.G., The crystal structure of human pyrin b30.2 domain: implications for mutations associated with familial Mediterranean fever. JMB, 2009 Nov 27;394(2):226-36.